CHARACTERIZATION OF INDUSTRIAL AND BIOLOGICAL COMPLEX FLUIDS USING CONFOCAL MICROSCOPY

by

Danial N. Hohne

A dissertation submitted in partial fulfillment
of the requirements for the degree of
Doctor of Philosophy
(Chemical Engineering)
in The University of Michigan
2008

Doctoral Committee:

Associate Professor Michael J. Solomon, Chair
Professor Mark A. Burns
Associate Professor John G. Younger
Assistant Professor Joerg Lahann

to the memory of my dad, Bill Hohne, who
instilled the value of education

Acknowledgements

Completing a Ph.D. dissertation is not at all an individual effort. In fact the dissertation truly is the culmination of many experiences and relationships into one thesis. It takes many people, most with a lot of patience. The following people made all of this possible.

First I thank my advisor, Prof. Michael Solomon. He is a wonderful scientific mentor. Mike's level of dedication makes it easy to do your best because you know he expects nothing less of himself. What makes Mike unique is his belief that the PhD is an educational process, not just a period of time spent in the lab. I've learned a lot from working with him and for that I am grateful.

Working with the cognate member of my committee, Dr. John Younger has been a special treat. Not only is he an emergency medicine doctor who somehow finds time to conduct great research, but he has dedicated a lot of precious time to mentoring me in biological studies. The afternoons spent in his office or lab have been some of the most enjoyable times spent. He has a way of creating confidence in his students with his ability to drop everything at an opportunity to teach which has been invaluable to me. His dedication to this dissertation goes well beyond that of the typical cognate.

I also appreciate the interactions I have had with the members of my Dissertation Committee from Chemical Engineering: Profs. Mark Burns and Joerg Lahann. They are

both great scientists who have provided excellent feedback during my time at the University of Michigan.

I also appreciate the assistance of my colleagues in the Solomon group, both past and present. A common thread in all Solomon students is the desire to help one another whenever needed. Without help from everyone, this dissertation would not be possible. Mike and Tesfu helped with confocal microscopy and the shear cell. Clare and Desh taught me everything I know about image processing. Afternoons spent with Yin working on gels will not be forgotten. Siva was a pioneer in the group's venture into microfluidics. Working with Laura, Reggie and Abhi on other things has also been great. We've also had the pleasure of great undergraduates in our laboratory. Steve Dzul has provided assistance in working through the rod code. I believe our Post-Doc, Dr. Georgina Wilkins, cannot value her contribution to all our work enough. She provides a perspective to our work we cannot get anywhere else. Finally, I especially appreciate the relationship with my "batch-mate" Desh. Not only has he contributed so much to this work, but he has always been there to listen. I hope I have returned the favor to each of you.

Other people at the University have contributed to this work as well. Thank you to Hsien-Yeh Chen for making all the CVD cover slips for the emulsion project. Thank you to the great people in Dr. Younger's laboratory for growing bug and providing general advice in the lab: David Bracho, Margaret Thornton and Megan Cartwright. Harald Eberhart, the departmental glass blower, has helped build many devices for these studies. Brian Johnson assisted in the clean-room fabrication of the microfluidic devices. Finally, thank you to the people who keep the department running, Claire O'Connor, Leslie

Cypert, Rhonda Sweet, Linda Castro, Susan Hamlin, Connie Bacus, Ruby Sowards, Shelley Fellers and Mike Africa. These are the people that keep us in business.

My family has contributed to this work in ways they will likely never know. Thank you to my sister Amanda for providing inspiration. Also, thank you to my brother-in-law Sgt. Luigi Magnanti for providing appropriate perspective on what a "bad day" is. Thank you to my "local" parents, Lou and Vickie, for your constant support and love. Lastly, thank you Mom, for doing everything in your power to ensure the quality of my education. This thesis is a reflection of the time, money and energy you and Dad spent. I want you to know that the sacrifices did not go unnoticed or unappreciated.

Finally, I need to thank the two people in my life that have contributed the most to this accomplishment. Without constant loving support at home, this would have never been possible. Thank you, Nellie, for giving me this opportunity. The PhD has always been a dream and without your share in that dream, it could not have been done. Thank you also to my little girl, Jaclyn. You make it hard to go to work, but then you make it just that much sweeter to come home. I love you both.

Table of Contents

List of Figures

Abstract

Characterization of Industrial and Biological Complex Fluids Using Confocal Microscopy

by
Danial N. Hohne

Chair: Michael J. Solomon

Complex fluids are materials that respond to applied stresses in a way that is intermediate between that of a purely viscous fluid or a fully elastic solid. The characterization of material properties depends upon the ability to both apply variable stresses or strains to the complex fluid and to measure the resulting response. Often the macroscopic response of these materials depends upon the microscale structure. In this dissertation, confocal laser scanning microscopy is used to analyze microscopic changes in complex fluids. We developed methods to apply the stress or strain that matches the application or environment of the material to be characterized. For instance, confocal images of the emulsion structure of fountain solution in ink exposed to oscillatory shear flow on model substrates were acquired. We found that surfactants inhibit aqueous droplet wetting on hydrophobic substrates. Without surfactants, surface coverage of the aqueous fountain solution on the hydrophobic substrate became quite high. This result is relevant to defects in lithographic printing. To characterize the material properties of

biofilms a tunable small-scale device was needed. We developed a flexible microfluidic rheometer to apply a compressive force of ~200 pL volume. We used confocal microscopy to detect the deformation of a membrane in contact with a test material when compressive stresses were applied. This measurement allowed us to characterize material properties including elastic modulus and relaxation time of soft viscoelastic solids, biofilms in particular. We report evidence of strain hardening in biofilms; a result that could have implications for the understanding of clearance of biofilms in industrial and physiological environments. To understand the source of this phenomenon we applied confocal microscopy to characterize the structure of bacteria aggregated in a polysaccharide matrix. Interestingly, while aggregated bacteria and bacteria in biofilms are held together by ostensibly the same material we find their inter-bacterial distance to be quite different. Once this tool was developed the origin of strain-hardening in biofilms could be addressed. The strain-induced trajectories of individual bacteria found using image processing of confocal micrographs were analyzed to show that strain hardening occurs without an increase in volume fraction.

Chapter 1

Introduction

1.1 Motivation

While we generally classify non-gaseous matter as either a solid or a liquid, we often come in contact with materials that are actually somewhere in between. Solids and liquids can be classified by applying a finite stress to each material. When a step-wise stress is applied to a solid it will immediately deform a specific amount based on its elastic modulus. When the stress is released it will likewise instantly return to its original form. A similar experiment performed on a liquid will show that the liquid will continue to deform as long as the stress is applied. The amount of deformation related to the applied stress is dictated by the liquid's viscosity. When the stress is removed, the liquid remains in its strained state. Complex fluids are those materials whose behavior cannot be described by these simple responses to stress. Examples of such materials include blood, paint, whipped cream and polymer solutions. Their response to stress or strain is viscoelastic [1].

Like the experiments described above, material property characterization of complex fluids relies upon measuring the stress/strain response of the material. Unfortunately, because of their viscoelastic (and often non-linear) behavior, experimental techniques to quantify complex fluid material properties are not simple. Data from mechanical rheometers are used to characterize the bulk behavior of complex fluids in

steady-state, transient and frequency dependent flows [2]. Mechanical rheometers can record interesting bulk phenomena such as shear-thinning, yield stress and thixotropy. Consumer products, food science, pharmaceuticals and biological systems rely on precise tuning of these properties for functionality, processing and quality. Often this macroscale behavior is the result of underlying microscale interactions within the viscoelastic material. To quantify this effect, methods to measure material properties of complex fluids at small characteristic length scales have been developed.

Many methods exist to characterize the local structure and dynamics of complex fluids. Laser light scattering and high resolution microscopy are two such techniques. Laser light scattering has been used to quantify the structure of polymer solutions [3, 4], liquid crystals [5] and colloidal suspensions [6, 7]. Dynamic light scattering is used to characterize the motion of small molecules or colloids within these materials. Based on the magnitude of this motion, samples can be classified as gels or liquids [6]. With this technique relaxation times can also be characterized [8, 9]. Methods such as these report the thermal motion of small particles within quiescent samples. Similarly, scattering patterns can be acquired during the application of an external stress. Integrating a device to apply an external flow field with laser light scattering allows for microstructural changes in the complex fluid to be recorded [4, 10, 11]. These methods provide evidence of the physical interactions at the microscale that result in interesting macroscale phenomena. This type of analysis can be used to help characterize processing parameters of existing products or formulate new materials.

High resolution microscopy coupled with image processing is used to characterize similar morphologies in colloidal suspensions as those reviewed above for light scattering

techniques. Image processing is used to quantify properties of structure and dynamics from qualitative images. 3D confocal microscopy can be applied to identify the local structure of colloidal crystals [12] and gels [13]. Like light scattering, this technique is not limited to quiescent samples. Flow devices have been mounted to the microscope in order to measure shear induced crystallization and yield of colloidal suspensions [14, 15]. Images have also been acquired identifying fractures in colloidal gels induced by squeeze flow [16]. One advantage of microscopy over light scattering is that images of individual colloids within the structure are acquired. These images can be used to quantify dynamic and structural heterogeneities in the system [13]. These heterogeneities would typically be averaged in bulk characterization techniques such as mechanical rheometry. That is, bulk characterization methods fail to quantify material properties due to heterogeneities and local structural properties of the system.

Structural characterization from these techniques provides evidence of the physical nature of non-linear behavior reported with rheometry. For example, evidence of a phase change from either of these methods would likely result in an anomaly in mechanical rheometry at similar conditions. These structural characterization techniques do not always result in quantification of specific mechanical properties (such as the complex modulus) to compare numerically with mechanical rheometry.

However, one method to apply measurements from light scattering and high resolution confocal microscopy to determine viscoelastic material properties is microrheology. This method reports the complex modulus of materials based upon the mean squared displacement of probe particles in the solution. By applying the frequency dependent generalized Stokes-Einstein equation, the complex modulus of polymer

solutions can be determined [17]. The method characterizes the complex modulus of materials based on the diffusive motion of the particles (exactly the quantity each technique measures) [17-20]. In dilute polymer solutions (elastic modulus < 1 Pa) microscopic particle tracking compares well to mechanical rheometry [21]. Unfortunately, issues arise when using the method to characterize heterogeneous materials such as gellan gum [22]. For these materials specific experiments need to be designed to better understand their rheological behavior. Coupling devices designed to apply appropriate stresses/strains with microscale characterization techniques such as confocal microscopy can allow for both structural and rheological characterization of complex fluids. These methods can be specifically used to characterize materials found in industry and biology.

Light scattering and confocal microscopy methods are often applied to model materials such as colloids to understand fundamental physics associated with a broad class of materials. In fundamental studies of colloids densities and refractive indices are matched to eliminate complexities in the analysis of data [13]. While these types of experimental studies provide wonderful insight into the behavior of many complex systems, extension of these techniques to industrial or biological complex fluids can be difficult. For example, to understand the 3D structure of an ink-fountain solution emulsion, the pigment must be removed from the ink to reduce turbidity [23]. For biofilms, confocal microscopy is often applied to qualify structural heterogeneities and quantify bulk physical quantities (i.e. film thickness). Often researchers rely on other methods to then quantify mechanical properties [24, 25]. In this thesis we use confocal

microscopy to characterize the local structure and material properties of industrial and biological complex fluids such as ink-fountain solution emulsions and biofilms.

In lithographic printing roll-coating is used to transfer an aqueous fountain solution and oil based ink to a printing plate. The plate is designed with hydrophilic and hydrophobic sites to aid in the transfer of the two solutions to the appropriate location (i.e. the non-image area would be hydrophilic, thus the aqueous fountain solution would preferentially wet these sites). For successful lithographic printing the fountain solution and ink must be immiscible on the two surfaces. Interestingly, defect-free lithography also depends on the two liquids forming an emulsion [26]. Confocal microscopy has been used to characterize droplet size of fountain solution in pigment free ink [23]. Here, we build upon this study in two ways: (1) we leave the pigment in the ink to study the emulsion structure using ink as supplied and (2) we apply a shear flow to the system to measure the evolution of the droplet structure on the substrate. We use confocal microscopy to evaluate the evolution of the emulsion structure where it matters most for print processing: on the substrate. This type of evaluation would be difficult to quantify without using microstructural characterization techniques.

Complex fluids can be found in the biological sciences as well. One such complex fluid is the biofilm. Biofilms grow from microcolonies of individual planktonic cells held together by a polysaccharide matrix. These biofilms can be found in natural or physiological aqueous environments [27]. Interestingly, some biofilm forming bacteria have clinical significance in their role as nosocomial pathogens [28, 29]. Biofilms are viscoelastic in their response to stress [30-32] and heterogeneic in structure [33]. For this reason it is difficult to characterize their material properties using mechanical rheometry.

Just as shear flow was combined with confocal microscopy in the industrial ink study, we apply a similar strategy to characterize biofilms. First we develop a microfluidic rheometer to study the viscoelastic properties of biofilms at small length scales. We then use image processing of confocal micrographs to quantify the microstructure of the biofilm at length scales of the individual bacteria. Finally we evaluate the microstructural evolution of the biofilms in response to compressive strain.

As reviewed above, many macroscopic material properties are dictated by their microstuctural evolution. Therefore, to understand the viscoelastic nature of industrial and biological complex fluids, rheology must be coupled with another tool to detect structure at small length scales. The microstructural characterization tool we use is confocal microscopy. With this tool we determine material properties and interesting structural phenomena in complex fluids found in industry and biology.

1.2 Thesis outline

As stated above, the goal of this dissertation is to characterize the structure and material properties of industrial and biological complex fluids using confocal microscopy. We use high resolution imaging to characterize these materials at length scales specific to their application or environment. For example, lithographic printing involves length scales of ~ 10 μm [34] and biofilms inhabiting physiological environments may flow through capillaries of the same order (D = 10 μm [35]). In chapter 2 the structural evolution of fountain solution emulsion droplets in ink is characterized at these length scales. We quantify the structural evolution of fountain solution droplets on energetically different substrates when the emulsion is exposed to simple shear. In chapter 3 a flexible microfluidic rheometer is used to characterize soft

viscoelastic solids including biofilms. Image processing methods developed to study colloidal suspensions are extended to bacterial aggregates and biofilms to characterize their structure in chapter 4. Finally these image processing methods are used to inform our investigation of strain-hardening in biofilms in chapter 5. Because characterization of these materials often involves specific experimental procedures each chapter includes a literature review and methods section. Summary points and future work will conclude the thesis in chapter 6.

References

1. Larson, R.G., *The Structure and Rheology of Complex Fluids*. 1999, New York: Oxford University Press.
2. Ferry, J.D., *Viscoelastic Properties of Polymers.* 3rd Edition ed. 1980, New York: John Wiley and Sons.
3. Francis, R.S., G.D. Patterson, and S.H. Kim, *Liquid-like structure of polymer solutions near the overlap concentration.* Journal of Polymer Science Part B-Polymer Physics, 2006. **44**(4): p. 703-710.
4. Lee, E.C., M.J. Solomon, and S.J. Mulller, *Molecular orientation and deformation of polymer solutions under shear: A flow light scattering study.* Macromolecules, 1997. **30**(23): p. 7313-7321.
5. Avsec, M., et al., *Band structure of orientational modes in quasiperiodic mesoscale liquid-crystal-polymer dispersions.* Physical Review Letters, 2007. **98**(17).
6. Mohraz, A. and M.J. Solomon, *Gelation and internal dynamics of colloidal rod aggregates.* Journal of Colloid and Interface Science, 2006. **300**(1): p. 155-162.
7. Vermant, J. and M.J. Solomon, *Flow-induced structure in colloidal suspensions.* Journal of Physics-Condensed Matter, 2005. **17**(4): p. R187-R216.
8. Stepanek, P., et al., *A dynamic light scattering study of fast relaxations in polymer solutions.* Macromolecules, 2007. **40**(6): p. 2165-2171.
9. Nyrkova, I.A. and A.N. Semenov, *Dynamic scattering of semirigid macromolecules.* Physical Review E, 2007. **76**(1).
10. Liberatore, M.W. and A.J. McHugh, *Dynamics of shear-induced structure formation in high molecular weight aqueous solutions.* Journal of Non-Newtonian Fluid Mechanics, 2005. **132**(1-3): p. 45-52.
11. Mohraz, A. and M.J. Solomon, *Orientation and rupture of fractal colloidal gels during start-up of steady shear flow.* Journal of Rheology, 2005. **49**: p. 657-681.
12. Leunissen, M.E., et al., *Ionic colloidal crystals of oppositely charged particles.* Nature, 2005. **437**(7056): p. 235-240.
13. Dibble, C.J., M. Kogan, and M.J. Solomon, *Structure and dynamics of colloidal depletion gels: coincidence of transitions and heterogeneity.* Phys Rev E Stat Nonlin Soft Matter Phys, 2006. **74**(4 Pt 1): p. 041403.
14. Cohen, I., et al., *Slip, yield, and bands in colloidal crystals under oscillatory shear.* Physical Review Letters, 2006. **97**(21).
15. Solomon, T. and M.J. Solomon, *Stacking fault structure in shear-induced colloidal crystallization.* Journal of Chemical Physics, 2006. **124**(13).
16. Varadan, P. and M.J. Solomon, *Direct visualization of flow-induced microstructure in dense colloidal gels by confocal laser scanning microscopy.* Journal of Rheology, 2003. **47**: p. 943-968.
17. Mason, T.G., et al., *Particle tracking microrheology of complex fluids.* Physical Review Letters, 1997. **79**(17): p. 3282-3285.
18. Gisler, T. and D.A. Weitz, *Tracer microrheology in complex fluids.* Current Opinion in Colloid & Interface Science, 1998. **3**(6): p. 586-592.
19. MacKintosh, F.C. and C.F. Schmidt, *Microrheology.* Current Opinion in Colloid & Interface Science, 1999. **4**(4): p. 300-307.

20. Solomon, M.J. and Q. Lu, *Rheology and dynamics of particles in viscoelastic media.* Current Opinion in Colloid & Interface Science, 2001. **6**(5-6): p. 430-437.
21. Savin, T. and P.S. Doyle, *Static and dynamic errors in particle tracking microrheology.* Biophysical Journal, 2005. **88**(1): p. 623-638.
22. Caggioni, M., et al., *Rheology and microrheology of a microstructured fluid: The gellan gum case.* Journal of Rheology, 2007. **51**(5): p. 851-865.
23. Xambili, F., W. Shen, and I.H. Parker, *Ink-fountain solution interaction in lithography. Part I: observation of fountain solution droplets and air bubbles in ink vehicle using confocal microscopy.* Appita Journal, 2004. **57**(5): p. 399-403.
24. Allegrucci, M. and K. Sauer, *Characterization of colony morphology variants isolated from Streptococcus pneumoniae biofilms.* Journal of Bacteriology, 2007. **189**(5): p. 2030-2038.
25. Monier, J.M. and S.E. Lindow, *Frequency, size, and localization of bacterial aggregates on bean leaf surfaces.* Applied and Environmental Microbiology, 2004. **70**(1): p. 346-355.
26. MacPhee, J. *An engineer's analysis of the lithographic printing process*. in *Technical Association of the Graphic Arts*. 1979.
27. Watnick, P. and R. Kolter, *Biofilm, city of microbes.* Journal of Bacteriology, 2000. **182**(10): p. 2675-2679.
28. Balestrino, D., et al., *The characterization of functions involved in the establishment and maturation of Klebsiella pneumoniae in vitro biofilm reveals dual roles for surface exopolysaccharides.* Environmental Microbiology, 2008. **10**(3): p. 685-701.
29. O'Gara, J.P. and H. Humphreys, *Staphylococcus epidermidis biofilms: importance and implications.* Journal of Medical Microbiology, 2001. **50**(7): p. 582-587.
30. Rupp, C.J., C.A. Fux, and P. Stoodley, *Viscoelasticity of Staphylococcus aureus biofilms in response to fluid shear allows resistance to detachment and facilitates rolling migration.* Applied and Environmental Microbiology, 2005. **71**(4): p. 2175-2178.
31. Shaw, T., et al., *Commonality of elastic relaxation times in biofilms.* Physical Review Letters, 2004. **93**(9).
32. Stoodley, P., et al., *Biofilm material properties as related to shear-induced deformation and detachment phenomena.* Journal of Industrial Microbiology & Biotechnology, 2002. **29**(6): p. 361-367.
33. Stoodley, P., et al., *Relationship between mass transfer coefficient and liquid flow velocity in heterogenous biofilms using microelectrodes and confocal microscopy.* Biotechnology and Bioengineering, 1997. **56**(6): p. 681-688.
34. Mewis, J. and F. Dobbels, *Nip Flow and Tack of Printing Inks.* Industrial & Engineering Chemistry Product Research and Development, 1981. **20**(3): p. 515-519.
35. Enderle, J.D., Susan M. Blanchard and Joseph D. Bronzino, *Introduction to Biomedical Engineering*. 2000, San Diego: Academic Press. 1062.

Chapter 2

Near-surface structure of lithographic ink-fountain solution emulsions on model substrates

Chapter Summary

By means of confocal laser scanning microscopy, we present direct visual evidence of droplet interactions in emulsions of lithographic ink and fountain solution deposited on homogeneous surfaces of varying surface energies. Fountain solutions with gum arabic and isopropyl alcohol additives were emulsified in a thermoset ink and deposited between parallel plates that differed in whether or not they had been treated with the hydrophobic compound poly(*para*-xylylene) (PPX). To enhance the dynamics of the deposition process, these emulsions were subjected to high strain amplitude oscillatory shear flow. We measured the surface coverage of the fountain solution on the lower plate. The time evolution of droplet size and number on hydrophilic and hydrophobic glass surfaces was quantified as a function of the two fountain solution additives, gum arabic and isopropyl alcohol. Interestingly, although ink wetted the two substrates, both fountain solutions showed increased coverage on the hydrophobic substrate relative to the hydrophilic substrate. We explain the observations by considering the interplay of coalescence suppression due to the surfactant nature of the

additives coupled with the changing surface energy due to the addition of the surfactant. The analysis provides direct visual evidence of the complexity of droplet interactions that contribute to the performance of lithographic printing of ink fountain solution emulsions.

2.1 Introduction

Lithography is unique among printing methods in that the image area and non-image areas of the master, or plate, are in the same plane. The method thus uses variation in surface energy along the plate to produce an image. During the process a water based fountain solution is deposited through roll coating onto a heterogeneous surface, composed of hydrophilic non-image areas and hydrophobic image areas. Oil-based ink is then deposited in the same manner onto the same surface and the properties of the liquids and the solid plate dictate the quality of the print. This transfer of the two fluids to the plate and then to the substrate lies at the heart of successful printing. The basic flow regimes of roll-coating or nip flow have been studied and analyzed [1-3]. While the functionality of lithography depends upon the immiscibility of the two liquids, due to high shear rates in the nip (~ 10^5 s^{-1} at the minimum gap) [4] and the preferential wettability of the two surface types and liquids, a fountain solution-in-ink emulsion can be expected to form at the image area. This balance between the advantages of emulsion formation (i.e. removal of aqueous fountain solution from the image area [5]) and the need to separate the two fluids on the substrates is essential to the success of printing. That is, neither an ink that repels water too strongly, nor, one that forms an emulsion with the fountain solution too readily will perform well on press [5]. Practitioners of lithographic printing thus tend to focus on maintaining the appropriate balance of ink and water to ensure a successful product [5].

Direct visual evidence of the mechanisms involved in lithography has proven invaluable. Aurenty and co-workers prepared a model water-in-alkyd-resin system and then used ultrasound attenuation and visual microscopy to quantify droplet growth within the emulsion over time [6]. Recently, researchers have used confocal laser scanning microscopy (CLSM) to study bulk droplet growth in ink vehicles [7] and ink vehicle penetration into paper [8]. The studies of Aurenty and Xambili focused on bulk properties of the emulsions thereby neglecting surface effects. However, surface to volume ratios are typically significant because of small gap sizes and surface droplet structure is surely key to press performance. Therefore, the next step in directly visualizing ink/fountain solutions should be to explicitly consider substrate effects.

Here we characterize emulsion interactions with the substrate and transport effects between the near wall region and the bulk. We use parallel plate shear flow to speed droplet interactions and thereby accelerate transport effects that would otherwise be unobservable. By quantifying emulsion structures apparent in the CLSM visualizations, we show that both types of fountain solutions wet the hydrophobic substrate with a higher surface coverage than on the untreated glass. The lack of additives in the first solution allows droplets deposited on the surface of the hydrophobic substrate to coalesce both with droplets in the bulk and others on the surface. Including additives inhibits coalescence and leads to generally smaller droplet sizes on the hydrophobic substrate. Additives also act to generate more extreme differences in droplet number density between the hydrophilic and hydrophobic substrates.

The results reported here are related to the lithographic printing literature [1-10] because they provide new experimental information about microstructure that complements recent theoretical work as well as studies of macroscopic behavior in

printing. For example, Lenz and Kumar establish that the dynamic behavior of the tri-layer structure that would result from residual ink on press can lead to an instability that would result in emulsion structure [11]. This work addresses what the long-term fate of such emulsion components might be. The work also provides microstructural evidence for the finding of Shen et al. that the dominant mechanism for prevention of ink transfer to the non-image area is an initial step when the entire surface is wetted by fountain solution [9]. The emulsion structure alone provides no protection to the non-image area as ink will coat both the hydrophobic substrate as intended and the hydrophilic non-image substrate. Our work is consistent with this dynamic view of wetting in lithographic printing, since we observe time-dependent surface structure that depends sensitively on dynamical processes such as coalescence in addition to thermodynamic considerations such as fountain solution formulation and surface energetics.

2.2 Materials and methods

2.2.1 Preparation of lithographic ink-fountain solution emulsions

The procedure for creating the ink-fountain solution emulsions was adapted from a commercial process. A lithographic ink, Arrowtek AP Process Magenta Ink (Flint Ink, Ann Arbor, MI), was used in this study. As reported by the manufacturer, the ink has a viscosity ~300 Pa.s (at shear rate ~ 1 s^{-1}) and a solids content (wt%) of ~75%. With this ink, we studied two different fountain solutions. The first consisted of distilled water with phosphoric acid (pH=4.1). The second consisted of 15% IPA and 10% gum arabic in the above solution, keeping the pH the same. Both additives are typical of commercial fountain solutions [10]. Usually isopropyl alcohol is used to lower the surface energy of water [5] and gum arabic is used as a desensitizing agent [11]. For the purpose of imaging, fluorescein dye was added to the fountain solutions at a concentration of 0.1%

(w/w). To disperse the fountain solution, the ink was stirred using a standard overhead laboratory mixer rotating at ~750 rpm for 5 min. While mixing at the same rate, a 20% (w/w) (~19.5% v/v) emulsion was created by adding the appropriate amount of dyed fountain solution dropwise and allowing the emulsion to mix, again at 750 rpm for 15 minutes. To ensure any air incorporated in the emulsion was removed, the sample was allowed to degas for a minimum of 24 hours before further testing was performed. This procedure is similar to typical fountain solution development tests such as water uptake and emulsion rheology tests (Flint Ink, Ann Arbor, MI).

2.2.2 Surface modification and characterization

In order to simulate the hydrophilic non-image area and hydrophobic image area of typical lithographic printing plates, two model surfaces were produced. The non-image area was simulated using a Corning cover glass cleaned with ethanol. The image area was simulated by the chemical vapor deposition of poly(*para*-xylylene) (PPX) on the glass cover slip [13]. The contact angle of water in air on the substrates was 40º for the glass cover slip and 84º for the PPX coated cover slip. Because typical lithographic printing plate water contact angles are ~15º and ~80º for non-image and image areas, respectively [14], the simulated surfaces are good approximations of industry practice. Note that the typical surface roughness of CVD coatings is 2-9 nm [15] and of glass is ~ 90 nm [16]. To prevent contamination, surfaces were cleaned with ethanol prior to all experiments.

2.2.3 Confocal laser scanning microscopy (CLSM)

Imaging was performed on an inverted Leica TCS SP2 confocal microscope using a 100x oil-immersion objective with a numerical aperture NA = 1.4. Dual-channel fluorescence imaging was used to observe the two phases of the emulsion with a single

pixel resolution of 69 nm. All images collected were of dimension 35µm x35µm. An Argon Ion laser provided incident light at 488nm and two photo-multiplier tubes (PMT) detected the fluorescence of the dyed fountain solution from 500-515 nm and the autofluorescence of the ink phase from 575-610 nm. In order to visualize the structure of the emulsion at the surface, a single xy scan was captured at a distance < 1 µm above the cover slip. For the NA of the objective used, the depth of field of the CLSM is ~ 1.1 µm. Fig. 2.1 shows a typical dual-channel image of fluorescently labeled buffer solution in ink on hydrophilic glass. The CLSM was also used to acquire images normal to the cover slip substrate.

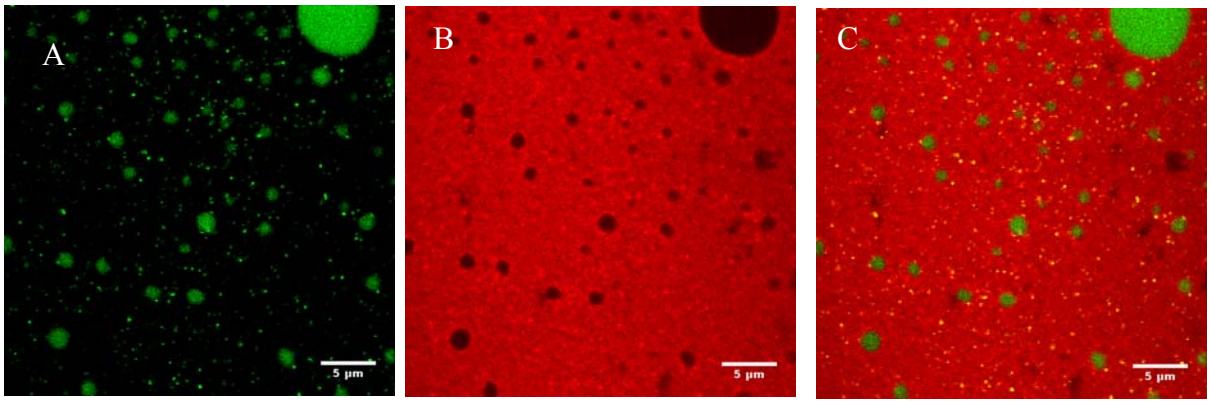

Figure 2.1: Typical CLSM images of ink-fountain solution emulsion. Scale bars are 5µm. A.) Image with detection range 500-515 nm (fountain solution phase). B.) Image from emission range 575-610 nm (ink phase) C.) An overlay of the two images.

2.2.4 Image analysis

All image analysis was performed using ImageJ software available from the National Institute of Health (http://rsb.info.nih.gov/ij/). The water phase image was principally analyzed, but results with the ink phase were consistent. An image was first convoluted with a Gaussian filter with a range of 3 pixels (0.207 µm). This distance was selected because it is approximately the Rayleigh limit of optical resolution for the

imaging system used [17]. A threshold based upon the histogram of the image was then applied to return a binary image of the brightest locations. The contour mapping function available on ImageJ was used to develop a distribution of droplet areas on the cover slip (Fig. 2.2). For this study we excluded any droplets below the Rayleigh limit of resolution (~ 0.2 μm). Results were sensitive to the filter range in that a lower range would not eliminate noise sufficiently and an increased range would give inaccurately large droplet sizes. The automated threshold, described in the literature associated with the program (http://rsb.info.nih.gov/ij/), was used to account for sample variation in intensities. The image analysis methods were applied uniformly to all data sets.

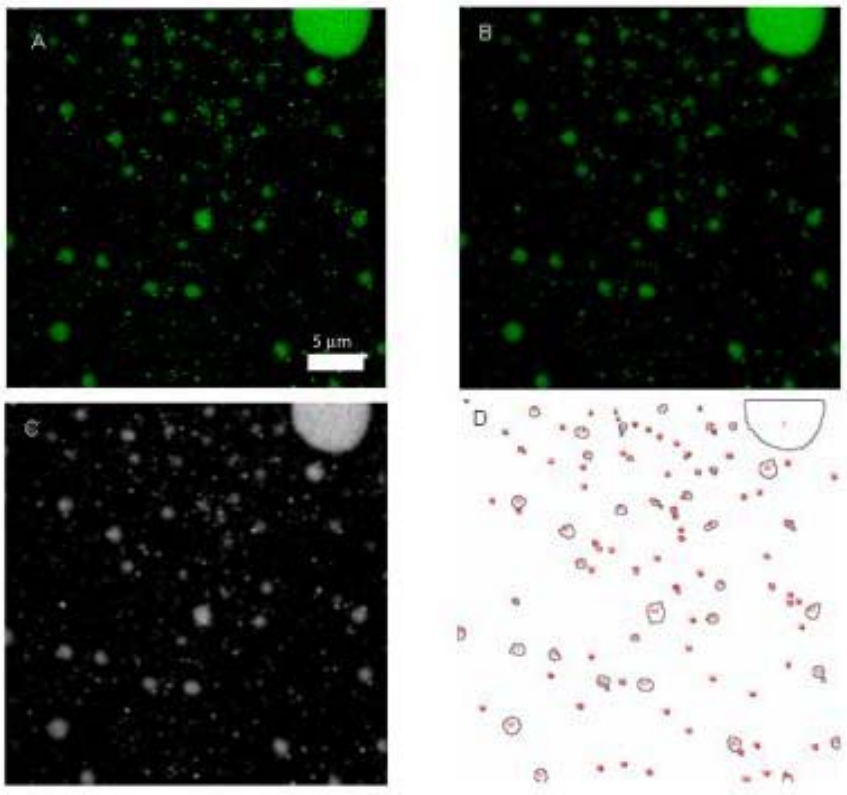

Figure 2.2: Image processing analysis performed with ImageJ software. A shows original green channel image (scale bar is 5 μm). B and C depict the Gaussian blur and threshold respectively, while D shows the results of the contour map.

2.2.5 Oscillatory Shear Flow

A parallel plate shear apparatus was mounted to the microscope to interrogate emulsion structure after an applied flow. The purpose of the shear device was to increase the number of interactions between droplets. The device is as described in Solomon and Solomon [18]. The lower plate of the apparatus was a 24 x 50 mm Corning cover slip mounted to an aluminum plate. This aluminum plate was attached to orthogonal linear stages to adjust the level and ensure the two plates were parallel to within 10 μm [17]. The upper glass plate was attached to a linear motor with motion parallel to the two plates. The gap in the flow was adjusted by moving the upper plate with a manual linear stage. For this study, the gap was 650 μm and the upper plate velocity was 10 μm/s.

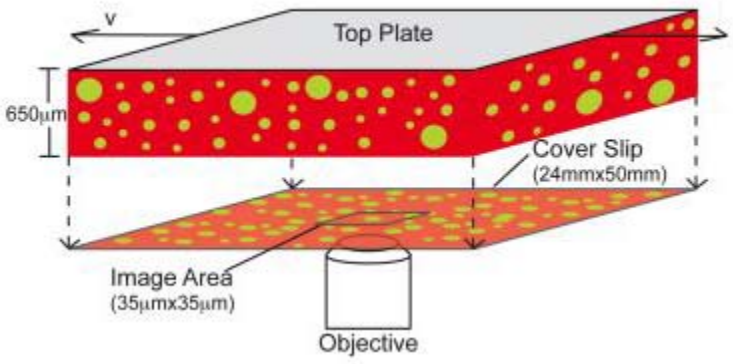

Figure 2.3: Schematic of experimental device. The shear cell consists of parallel plates. The upper plate is attached to a linear stage allowing for motion in the transverse direction. The bottom plate is a cover slip affixed to an aluminum plate with a cut-out for imaging. The cell is mounted to the inverted microscope for imaging from the bottom of the device.

Thus, shear rate = 0.015 s^{-1}. Fig. 2.3 provides a schematic of the experimental apparatus. The strain associated with the oscillatory flow was defined by the traverse distance of the upper plate during half a cycle [19]. Oscillatory strains of γ = 0.3, 0.5 and 1.0 were

applied. Because results at the different strains were not distinguishable, data sets reported are the average of all strains studied.

2.3 Results and discussion

2.3.1 Study design

In order to determine solution and substrate effects on droplet deposition, a series of experiments were completed in a 2 x 2 matrix type design. The first variable manipulated was substrate: one substrate was hydrophilic glass, the other was glass coated with hydrophobic PPX. The second variable manipulated was fountain solution composition: one was the additive-free fountain solution, the other was the fountain solution with gum arabic and IPA additives. The ink solution was held fixed for all experiments. For each fountain solution/substrate combination, the time dependence of the near-surface emulsion structure was monitored by CLSM for a duration of ~ 6 hrs. This duration was selected because steady-state emulsion microstructure was attained at that point. CLSM imaging was executed approximately every half hour during the test duration. In addition to qualitative images, quantitative image processing yielded measurements of the mean droplet size, the droplet number density and the total percent surface coverage at each time step. Errors plotted are standard error of the mean from each experiment. Below, we first discuss qualitative differences among the four combinations of substrate and solution studied (Fig. 2.4). Next, we compare results of the quantitative measures. We conclude by discussing origins of the observations in light of substrate material thermodynamic interactions as well as transport processes between the near wall and bulk solutions.

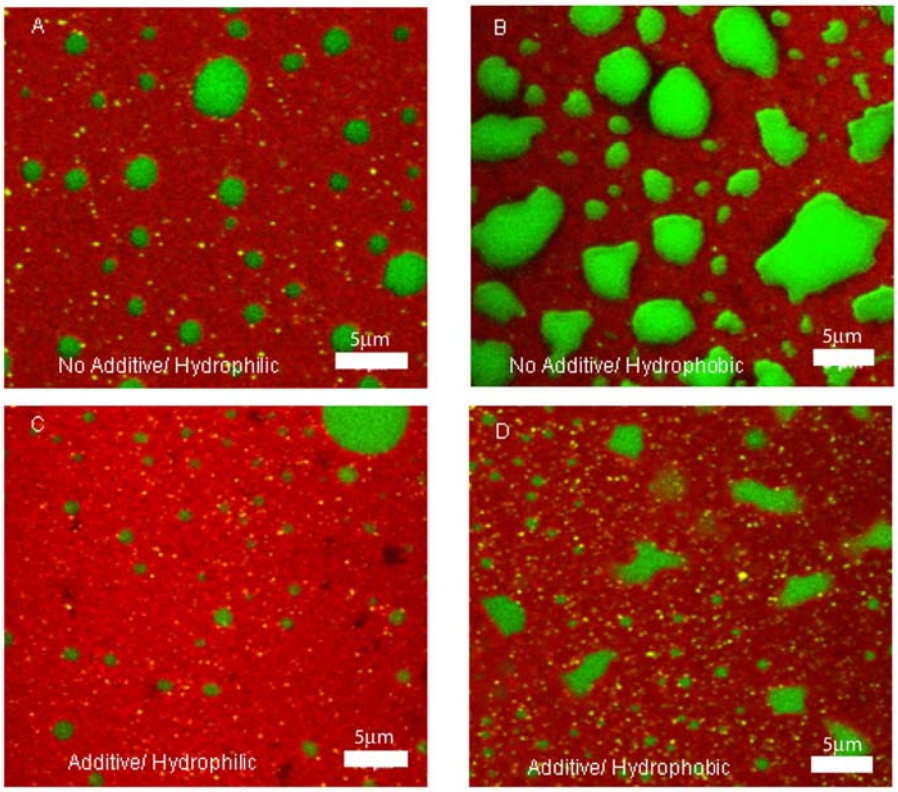

Figure 2.4: Qualitative images of different solutions of the two substrates after 6 hours of droplet evolution. Panels A and B show buffer solution on glass and PPX respectively. Panels C and D show with gum arabic and IPA on glass and PPX respectively.

2.3.2 Qualitative effects of substrate and fountain solutions composition on near wall emulsion structure.

Fig. 2.4 compares the four cases studied at the duration of six hours, after steady-state near wall emulsion structure had been achieved. For the case of the additive-free fountain solution and ink emulsion on a hydrophilic glass substrate (Fig. 2.4A), a distribution of droplet sizes is apparent. The surface coverage of fountain solution is quite low. Changing the substrate from hydrophobic to hydrophilic (Fig. 2.4B), keeps the number of droplets approximately constant; however the deposited droplet size is increased. Alternatively, keeping the hydrophilic substrate fixed, but adding gum arabic and IPA to the fountain solution (Fig. 2.4C), appears to result in fewer fountain solution

droplets at the surface. The overall surface coverage is reduced relative to the case of the additive-free fountain solution on glass. Finally, fountain solutions containing gum arabic and IPA additives on the hydrophobic substrate yield many small droplets with relative high surface coverage (Fig. 2.4D). The qualitative results are indicative of both main effects and an interaction effect of the two factors on the performance of ink fountain solution emulsions.

2.3.3 Quantitative effects of substrate and fountain solution composition on near wall emulsion structure.

Fig. 2.5a reports the time evolution of the mean droplet size for each of the four study conditions. At the longest times, the mean droplet area is greatest for the case of

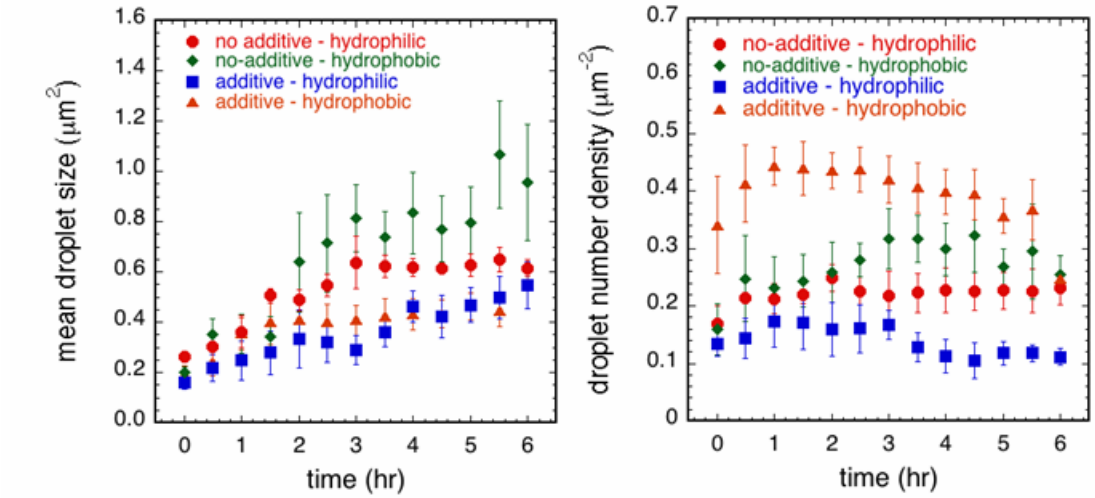

Figure 2.5: Mean droplet size (A) and droplet number density (B) on the two different substrates for the two different fountain solutions. Points represent the average of all data taken for the given conditions. The error bars represent the standard error of that mean.

no-additive fountain solution on a hydrophobic substrate, ~ 1 μm^2. For the other three study conditions, the mean droplet area is about constant, especially at the longest durations, ~ 0.6 μm^2. It is counterintuitive that increasing substrate hydrophobicity increases the mean droplet area of (hydrophilic) no-additive fountain solution. This

result will be discussed further in Sec.2.3.5 and its relationship to dynamic processes in lithographic printing will be assessed in the chapter conclusion.

Fig. 2.5b reports the time evolution of the droplet number density for each of the four study conditions. Complex behavior is apparent for the case of the emulsion with gum arabic and IPA additives on the hydrophobic substrate. Droplet number density increases to a maximum at ~ 2 hr, then decaying to a steady value of ~ 0.4 μm^{-2}. The no-additive fountain solution density is relatively independent of substrate hydrophobicity – the steady-state number (areal) density is about 0.25 μm^{-2}. Surprisingly, the addition of gum arabic and IPA to the fountain solution leads to a low number density of droplets on the hydrophilic glass substrate.

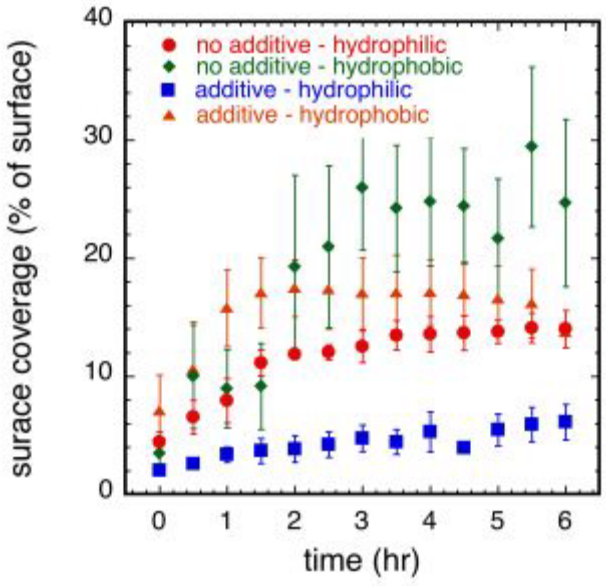

Figure 2.6: Total surface coverage of the solutions on the substrate. Again, the markers represent the average of all data taken for the given conditions and the error bars represent the standard error of the mean.

Fig. 2.6 reports the total surface coverage of the fountain solutions on the tested substrates. These results combine the effects of droplet area (Fig. 2.5a) and number density (Fig. 2.5b). For reference, the bulk fraction of fountain solution in these

emulsions is 20%. The largest surface coverage is given by the additive-free fountain solution on the hydrophobic substrate. Although the areal fraction of this case is greater than the volume fraction of fountain solution in the bulk, direct comparison of these two quantities is precluded because of their different dimensionality. The other three cases give rise to significantly lower surface coverage. Again, the fountain solution with additives has very low surface coverage on the hydrophilic substrate. In this case, surface coverage is less than 5%.

2.3.4 Results summary

The effects observed in Fig. 2.4-2.7 could be induced by the varying (thermodynamic) interactions between substrates, ink and fountain solution, or different dynamic wetting and transport effects or some combination of the two. Transport effects themselves could be linked to surface displacements or, alternatively, involve exchange between the near wall and bulk emulsion. All these processes can potentially impact lithographic printing. Several of the results shown in Figs. 2.4-2.6 are unexpected, and thus warrant further discussion in light of the underlying thermodynamic interactions and transport mechanisms. We summarize the observations here based on the results from the surface studies, and then consider each in turn in the remaining sections of the chapter:

1) For the additive-free fountain solution and ink emulsion, changing the substrate from hydrophilic to hydrophobic results in a greater mean fountain solution droplet area and a greater surface coverage. The number density of droplets is approximately unchanged. The surface coverage of the additive free solution on the hydrophobic substrate is greater than the bulk loading of the fountain solution.

2) For a hydrophilic substrate, addition of gum arabic and IPA to the fountain solution results in a lower droplet density and lower surface coverage. The mean droplet area is approximately unchanged.

3) For the fountain solution with gum arabic and IPA, changing the substrate from hydrophilic to hydrophobic results in an increase in the number density of fountain solution droplets.

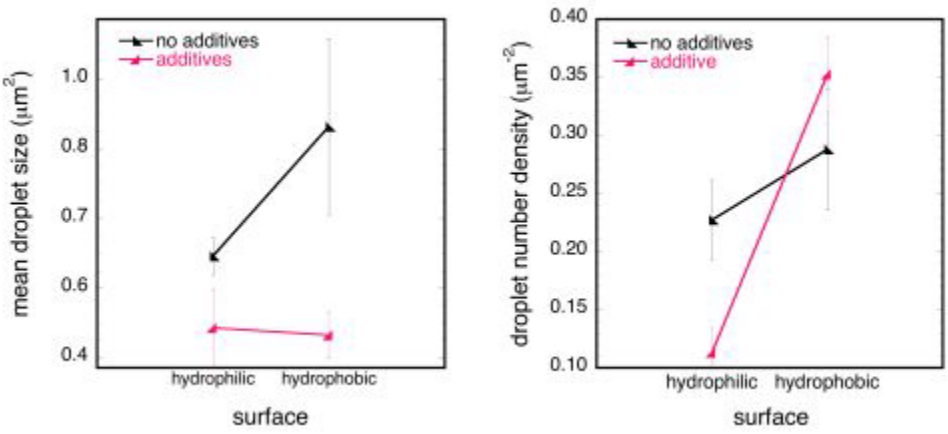

Figure 2.7: Figs. 2.7A and 2.7B depict the interaction plots showing the average mean droplet size and droplet number density of the last 2 hours of the experiments. The error bars represent the average error of the mean during that time.

Figs. 2.7 and 2.8 summarize these experimental results in a format typical of DOE (design of experiments) [20]. Values and error bars plotted are for t = 4.0 – 6.0 hrs, a duration that is approximately steady-state. The differing slopes of the curves for the performance measures of Fig. 2.7a (mean droplet size) and Fig. 2.7b (mean number density) are characteristic of interaction effects. That is, these results can only be explained by considering the joint effect of surface hydrophobicity and additive chemistry. Since surface coverage (Fig. 2.8) is the product of mean droplet size and number density, surface coverage can be viewed as a consequence of the Fig. 2.7 results. Interestingly, the simple behavior of Fig. 2.8 (hydrophobicity increases surface coverage;

additives decrease it) has a complex origin in the interaction effects of surface energy and additive chemistry on droplet size and number.

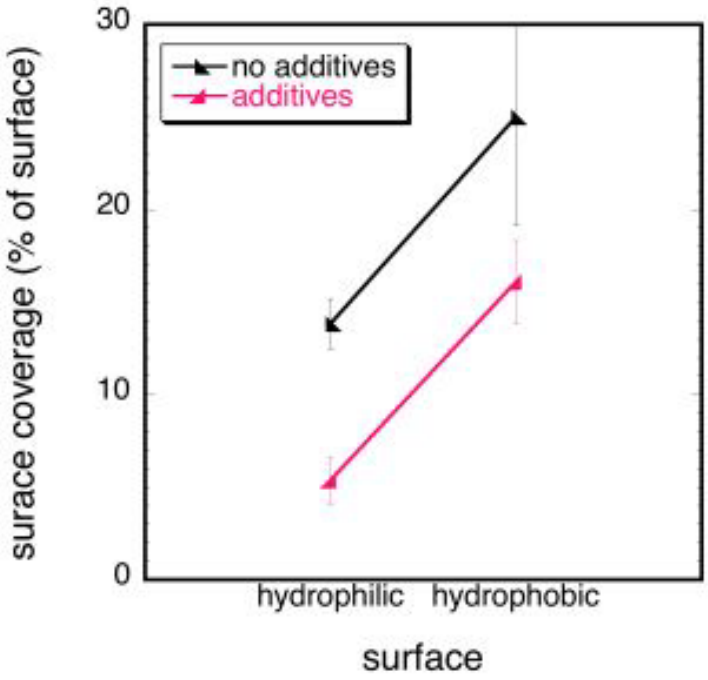

Figure 2.8: Interaction plot of average total surface coverage during the last 2 hours of the experiment. Again error bars represent the average error of the mean during that time.

Thus, Fig. 2.7 shows interaction effects between substrate and fountain solution composition on both mean droplet area and droplet number. Together, these interaction effects combine to yield main effects of substrate and of fountain solution chemistry on surface coverage (Fig. 2.8). Figs. 2.7 and 2.8 indicate that to adequately explain the results, we must account for the interaction effects in mean droplet area and number density. We next consider each interaction effect in turn. Although we acknowledge the potential role of IPA through its effect on solvent polarity, our discussion here focuses on the effects of gum arabic, because of its known surface activity and subsequent role in the interfacial dynamics that determine the emulsion structure.

2.3.5 Fig 2.7a interaction effect: Differing effects of fountain solution additives on mean droplet size as substrate is changed from hydrophilic to hydrophobic.

Fig. 2.7a reports that, regardless of substrate, surface droplets stabilized with gum arabic are smaller (~ 0.45 μm^2) than when the fountain solution is not stabilized with additives. The difference is extreme: in the case of the hydrophilic substrate, unstabilized droplets are ~ 50% greater. On the hydrophobic substrate, the droplets are about twice as large. The interaction with substrate is particularly puzzling: surface energy arguments would predict a smaller contact area of a hydrophilic droplet with a hydrophobic substrate. Instead, no-additive fountain solution droplets show the opposite effect.

To demonstrate the expectation more clearly, note that both surfaces have contact angles, θ, with the water in air that are less than 90º (~40º and ~84º for both untreated and treated glass respectively). Thus, the maximum height, h, and volume, V, of the surface droplet are described by the equations for spherical caps [21]

$$h = R\tan[\theta/2], \qquad (1)$$

$$V = \frac{\pi h[3R^2 + h^2]}{6}. \qquad (2)$$

where R is the droplet radius. Given the plausible assumption that the volume of the fountain solution droplets initially deposited are independent of substrate and that the contact angles in the fountain solution are not too different than from in air, eqns. (1) and (2) predict that the droplet radius on the hydrophobic substrate is smaller than that on the hydrophilic substrate (because of the larger contact angle). Since this initial result is not consistent with the Fig. 2.7a observations, additional evolution of the droplet size must occur (consistent with the time effects plotted in Fig. 2.5).

Intriguingly, eqns. (1) and (2) predict that the initial height, h, of droplets on the hydrophobic substrate is greater than on the hydrophilic substrate. This increased fountain solution height on the hydrophobic substrate increases the probability of contact between surface and bulk droplets.

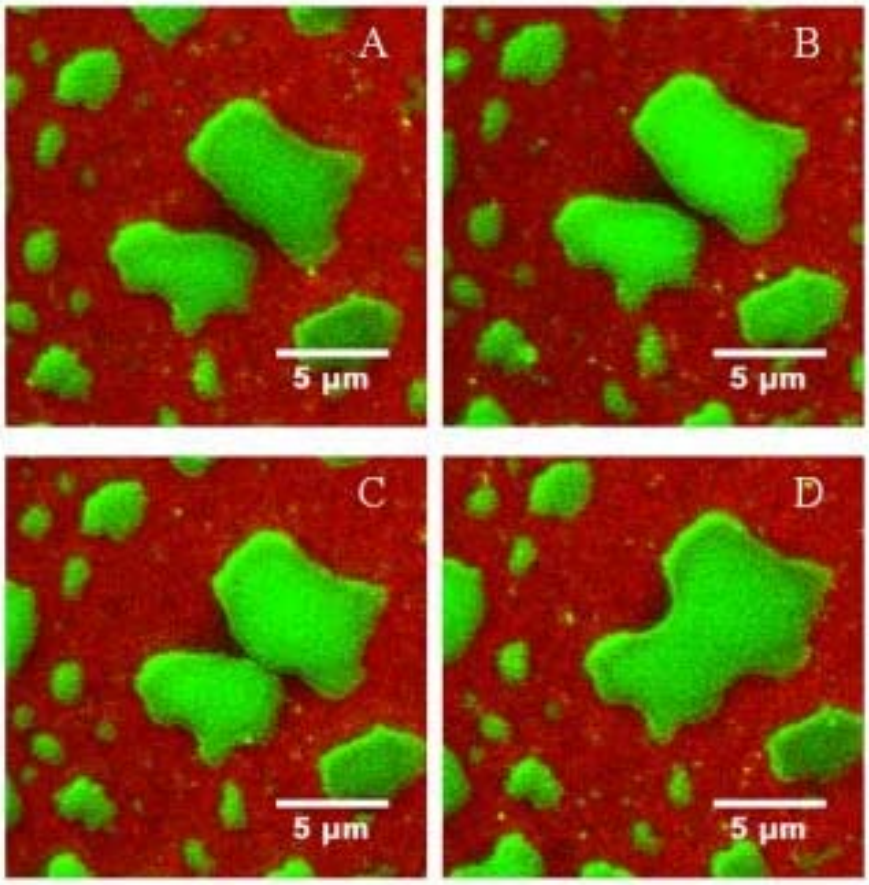

Figure 2.9: Surface coalescence of no-additive solution emulsion on PPX coating at different times during the experiment. A.) 2.5 hr. B.) 3 hr., C.) 3.5 hr. and D.) 4 hr.

The increase in fountain solution droplet area due to bulk droplet draining is coupled to the additional effect, shown in Fig. 2.9, of surface coalescence. Fig. 2.9 reports a typical surface coalescence event of the additive-free fountain solution on the hydrophobic substrate. Two initially distinct droplets laterally spread over duration ~ one hour until they contact and coalesce. The process increases the mean droplet area

just as the bulk draining phenomena. We reiterate that these processes occur most extensively on the hydrophobic substrate: the underlying physical origin for this interaction effect is the increased initial height of fountain solution droplets on hydrophobic substrates because of their large contact angle.

Why are these effects more pronounced in the case of fountain solutions that lack additives (as summarily shown in Fig 2.7a)? The answer is related to the additive gum arabic, which acts to suppress both the bulk draining and surface coalescence mechanisms that lead to greater droplet area. Gum arabic is a surface-active species comprised of hydrophobic polypeptides as well as the hydrophilic branched carbohydrates [12]. Such surfactants lead to suppression of droplet coalescence [21,22]. In this case, gum arabic

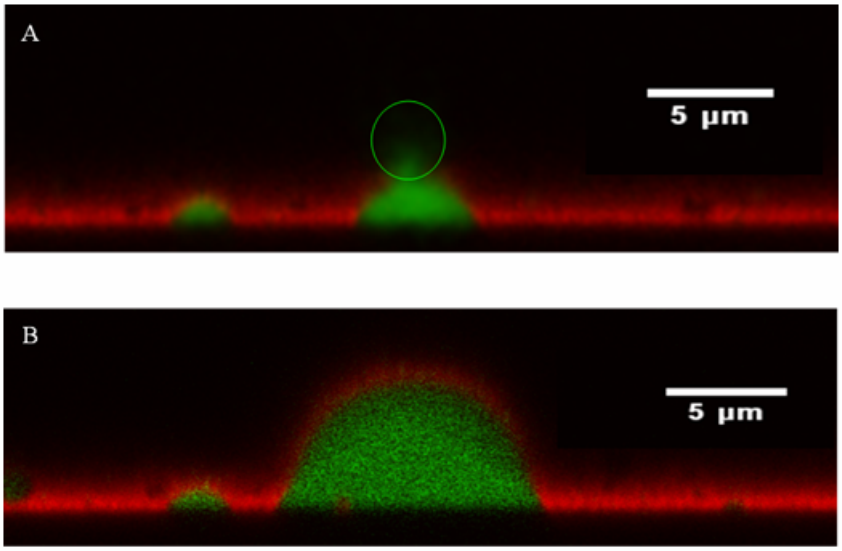

Figure 2.10: Drainage of bulk droplet into surface droplet. Figure A shows a spherical cap of solution with gum arabic and IPA with a droplet in contact from the bulk. Figure B shows the same spherical cap 2 hours later with drainage complete.

surfactant on the fountain solution surface leads to less bulk draining (because contact between bulk and surface droplets is suppressed) and less surface coalescence (because contact between surface droplets is retarded). Fig. 2.10 shows that while bulk draining

may occur in droplets with additives, the process is retarded due to the additives (duration ~2.5 hours). The reduced droplet size of additive fountain solutions relative to the additive free case is thus explained.

2.3.6 Fig 2.7b interaction effects: Differing effects of fountain solution additives on number density as substrate is changed from hydrophilic to hydrophobic.

Fig. 2.7b quantifies an interaction effect between fountain solution additives and substrate on droplet number density. Relative to the additive-free fountain solution, fountain solutions with gum arabic show decreased number density on hydrophilic substrates and increased number density on hydrophobic substrates. We explain this result by considering the hydrophobicity of the gum arabic surfactant on the surface of the droplet. This hydrophobicity enhances surface adsorption of droplets on the hydrophobic substrate. This leads to increased surface density upon addition of gum arabic to the fountain solution. Conversely, the fountain solution additive acts to repel the hydrophilic substrate; gum arabic fountain solutions thus have lower number density on this substrate relative to the no-additive fountain solution.

2.4 Conclusions

In this chapter, we have identified the complex interactions between fountain solution chemistry and substrate hydrophobicity that lead to the surface coverage of fountain solutions in lithographic ink emulsions. We find that addition of gum arabic, a surface active hydrophobic polymer, with IPA acts to reduce surface coverage on substrates of two different surface energies (hydrophilic and hydrophobic). In addition, our observations report the counterintuitive result that fountain solution surface coverage is greater on hydrophobic substrates than on hydrophilic ones.

The explanation of these simple results is complex, involving interaction effects on drop size and number density. First, droplet size on hydrophobic substrates without additives is enhanced because of increased propensity for surface – bulk droplet coalescence and draining as well as surface coalescence of droplet pairs. Gum arabic additives suppress these transport processes. Second, droplet number density on hydrophobic substrates is increased in fountain solutions with additives because surface adsorption is promoted. Surface adsorption of fountain solution droplets is promoted because of hydrophobic interactions between the surface active gum arabic additive and the hydrophobic substrate.

These findings are relevant to the fundamental understanding of lithographic printing in the following three ways: i) while the time-scales are not the same as those associated with lithographic printing, the work provides direct visual evidence of mechanisms based on surface interactions and bulk-surface transport mechanisms that contribute to the dynamic wetting of surfaces; ii) it establishes the importance of gum arabic not just as a desensitizer on the non-image area [10], but also as a key component that retards the coalescence of surface droplets; iii) it provides microstructural evidence for the idea put forward by Shen et al. that the dominant mechanism for prevention of ink transfer to the non-image area is dependent upon initial wetting of the entire surface with fountain solution. In particular, the emulsion structure itself provides no protection to the non-image area because we observed that ink coated both substrates. Moreover, the study provides indications of the fate of emulsion structure that might be generated on press by, for example, the instability of a thin layer of residual ink [11]. Finally, our confocal microscopy characterization has established that the surface coverage of fountain solutions in lithographic ink emulsions can only be understood by resolving

complex interaction effects between surface hydrophobicity and fountain solution formulation at the level of droplet size and number density.

Acknowledgements

We thank Patrick Sneary, Anna Mae Trievel and Mark Latunski from Flint Ink for their support and providing materials for this project. We also thank Ronald Larson and William Schultz for their helpful insight. We also thank Flint Ink for their funding support.

References

1. Dobbels F. and Mewis J. *Analysis of nip flow operations involving a viscoelastic roller.* Chemical Engineering Science, 1978 **33**: p. 493-500.
2. Coyle, D.J. "Knife and roll coating" *Liquid Film Coating,* Kistler, S.F. and Schweizer, P.M., ed., 1997 London: Chapman & Hall.
3. Lenz RD and Kumar S. *Competitive displacement of thin liquid films on chemically patterned substrates.* Journal of Fluid Mechanics, 2007. **571:** p. 33-57.
4. Fernandez ME. et al. *Rheological analysis of highly pigmented inks: Flocculation at high temperatures.* Journal of Rheology, 1998. **42 (2):** p. 239-253.
5. MacPhee, J. *An engineer's analysis of the Lithographic printing process* TAGA Proceedings, Technical Association of the Graphic Arts, 1979. p. 237-277.
6. Aurenty, P. Schroder A. and Gandini A. *Water-in-alkyd-resin emulsions: Droplet size and interfacial tension.* Langmuir, 1995 **11:** p. 4712-4718.
7. Xambili, F. et. al. *Ink-fountain solution interaction in lithography. Part 1: observation of fountain solution droplets and air bubbles in ink vehicle using confocal microscopy.* Appita Journal, 2004. **57 (5):** p. 399-403.
8. Ozaki Y., Bousfield D.W. and Shaler S.M., *Three-dimensional characterization of ink vehicle penetration by laser scanning confocal microscopy*. Journal of Pulp and Paper Science, 2005. **31(1):** p. 48-52.
9. Shen W., Hutton B. and Liu F. *A new understanding on the mechanism of fountain solution in the prevention of ink transfer to the non-image area in conventional offset lithography* Journal Adhesion Science and Technology, 2004 **18 (15-16):** p. 1861-1887.
10. Fetsko, JM. *Relationship of Ink/Water Interactions to Printability of Lithographic Printing Inks: Part 2 – Surface Interactions*, National Printing Ink Research Institute, Inc., 1988.
11. Lenz RD and Kumar S. *Instability of confined thin liquid film trilayers* Journal of Colloid and Interface Science, 2007. **316:** p. 660-670.
12 Williams PA. and Phillips GO. "Gum Arabic", *Handbook of Hydrocolloids*. Phillips, GO. and Williams, PA., ed., 2000 Boca Raton, CRC Press, LLC.
13. Suh KY, Langer R and Lahann J *Fabrication of elastomeric stamps with polymer-reinforced sidewalls via chemically selective vapor deposition polymerization of poly(p-xylylene).* Applied Physics Letters, 2003. **83 (20):** p. 4250-4252.
14. Kato Y, Fowkes F.M. and Vanderhoff J.W. *Surface energetics of the lithographic printing process.* Industrial and Engineering Chemistry Product Research and Development, 1982. **21(3):** p. 441-450.
15. Goschel U. and Walter H. *Surface film formation by chemical vapor deposition of di-p-xylylene: ellipsometrical, atomic force microscopy and x-ray studies*. Langmuir, 2000. **16(6):** p. 2887-2892.
16. Tahamori E.R., et al. *Effect of roughness on zirconia and titanium on fibroblast adhesion.* Artificial Organs, 2008. **32(4)**: p. 305-309.
17. Hecht, E. *Optics*, 4th ed., 2001. Addison Wesley p. 215, 480-481.

18. Solomon T and Solomon M.J. *Stacking fault structure in shear-induced colloidal crystallization* Journal of Chemical Physics, 2006. **124 (13):** Art No.134905.
19. Larson R.G. *The Structure and Rheology of Complex Fluids.* 1999, New York: Oxford University Press , pg 13 and Chapter 9.
20. Hicks C.R., *Fundamental Concepts in the Design of Experiments, 2nd Ed.,* 1973. Holt, Rinehart and Winston, Chapter 6.
21 Hu H. and Larson R.G. *Evaporation of a sessile droplet on a substrate.* Journal of Physical Chemistry B, 2002. **106 (6)**: p. 1334-1344.
22. Milner S.T. and Haowen X., *How copolymers promote mixing of immiscible homopolymers* Journal of Rheology, 1996. **40 (4):** p. 663-687.

Chapter 3
Flexible microfluidic device for mechanical property characterization of soft viscoelastic solids

Abstract

In this chapter we introduce a flexible microfluidic device to characterize the mechanical properties of soft viscoelastic solids such as gels and bacterial biofilms. The device imposes a stress on a test material by means of a microfabricated air channel which applies a fixed pressure to a thin, flexible poly(dimethyl siloxane) (PDMS) membrane in contact with the test material. The strain resulting from the applied stress is quantified by measuring the membrane deflection with a confocal laser scanning microscope. This deflection is governed by the viscoelastic properties of the PDMS membrane and the test material. The contributions of the two materials to the measured deformation are deconvoluted from finite element analysis and an independent (control) measurement of the PDMS mechanical properties in the device initially filled with water. We use the device to characterize both the steady-state elastic modulus and transient strain recoil of the soft materials gellan gum and bacterial biofilms. We find that the measured linear elastic moduli of 2% and 3% (w/w) gellan gum are 8.0 $\pm$ 0.2 and 30 $\pm$ 1 kPa respectively, in very good agreement with the results of conventional mechanical rheometry. The transient strain recovery of 2% gellan gum shows that the viscoelastic response is modeled by a single relaxation mode with λ = 19.4 $\pm$ 0.9s, a result that also

agrees well with macroscopic rheology. By studying two different monospecies biofilms comprised of *Staphylococcus epidermidis* and *Klebsiella pneumoniae*, we demonstrate that the device is capable of characterizing the mechanical properties of materials for which conventional rheometry is difficult to perform. We measure the linear Young's modulus of *S. epidermidis* and *K. pneumoniae* to be 3.2 kPa and 1.1 kPa respectively and the relaxation time of *S. epidermidis* to be 13.8 s. Finally, we discuss design parameters and detection limits of the method which show that the device has the capability to characterize soft viscoelastic solids with elastic moduli in the range of 10^2 - 10^5 Pa. This microfluidic rheometer addresses a need for a device capable of characterizing the mechanical properties of soft visoelastic solids common in fields such as biomaterials, food and consumer products using only 200 pL of test sample.

3.1 Introduction

Characterization of the mechanical properties of soft materials is important for fields such as consumer products, food science, biomaterials and pharmaceuticals. Viscoelastic properties of these materials span orders of magnitude. For example, the characteristic relaxation times of polymer solutions are ~10^{-5} seconds [1] while those of human vertebral bone are ~ 10^1s [2]. Likewise, elastic properties vary widely. For example, the Young's modulus of microcapsules used in self-healing polymer coatings are ~3GPa [3], while the storage modulus for whipping cream [4] is ~1-10kPa. Within these ranges fall many important biological materials including tissue scaffolds (E = 8-500 kPa) [5] and articular cartilage (E = 190-960 kPa) [6]. Material property characterization of this kind is important because mechanical properties control a material's functionality as in, for example, the case of self-healing polymers [7] or stem

cell differentiation [8]. Although existing rheological methods are well suited to the measurement of homogeneous materials, their applicability is more limited in cases where mechanical properties such as the viscoelastic relaxation time and linear elastic modulus exhibit microscale heterogeneity because of spatial variations in local structure. To quantify the properties of such heterogeneous materials, microscale characterization is required. Many such heterogeneous materials can be classed as soft viscoelastic solids. These materials do not readily flow, are highly elastic ($E < 0.1$ GPa) [9, 10], but are capable of some dissipation as evidenced by their transient viscoelastic response. Examples of soft viscoelastic solids include gels, biomaterials and mayonnaise.

To address the need for such local viscoelastic characterization, new techniques based upon microrheology, microfluidic rheometry and flexure-based rheometry have been developed. For example, microrheology correlates the individual motion of colloidal particles dispersed in complex fluids with the fluid's viscoelastic properties using methods such as diffusing wave spectroscopy, dynamic light scattering or multiple particle tracking microscopy [11-14]. Microrheology measures elastic moduli in the range of 0.1-1000 [15, 16] Pa and relaxation times on the order of micro to milliseconds [17, 18]. Particle-tracking microscopy can measure elastic moduli no greater than ~1 Pa due to dynamic error in particle location as the test material becomes increasingly stiff [19]. Researchers using light scattering methods have reported moduli no greater than about 1kPa [16]. The aforementioned issues of sample heterogeneity are potential limitations of microrheology - spatially resolved [20] and two-point [15] techniques have been introduced to improve the method's potential.

Methods to characterize viscoelastic properties by means of microfluidics have also been developed. Droplet retraction methods quantify relaxation times as fast as microseconds [1]. Weak elastic effects found in contraction and expansion flows have been measured [21, 22]. The addition of pressure sensing in these geometries yields simultaneous determination of shear and extensional rheology [23]. Advantages of microfluidic methods include small sample size and speed of characterization. However, to date microfluidic methods have been principally applied to weakly elastic fluids such as dilute polymer solutions. Yet, the prior discussion has identified the need for microscale characterization methods for systems for materials with much greater elasticity, such as soft viscoelastic solids.

Recently developed mini-rheometers also address the need for mechanical property characterization of small scale samples. Flexure-based rheometry has been applied to 1-10μL samples. The stresses imposed by these methods are in the range of 10-1500 Pa [24, 25]. Piezoelectric methods have likewise been applied to deform polymer solutions and measure their dynamic response to sinusoidal inputs [26]. Characterization of the viscoelastic relaxation time of weakly elastic polymer solutions would be possible with such devices. Finally, microindentation devices have been applied to characterize material properties of biofilms. These devices probe elastic moduli over the range of 1-10 kPa [27].

From this review it is apparent that a method to measure elastic moduli in the range of 10-100 kPa and relaxation times greater than milliseconds is lacking. Yet, such a method could be fruitfully applied to characterize properties of soft viscoelastic solids at a small length scale. In this manuscript we report a device suitable for mechanical

property characterization in this previously inaccessible range. The device is used to address issues of microscale structural heterogeneity and uses simple methods and materials previously developed and proven in the area of microfluidics.

To develop the flexible microfluidic rheometer we adapt the design of poly(dimethyl siloxane) (PDMS) devices previously developed for pumping and valving in microfluidic systems [28]. These devices use a two-layer assembly in which a PDMS membrane separates an air channel from a main fluidic channel. The PDMS membrane deforms in response to pressure in the air channel. Thus, pressurizing the air channel closes the fluidic channel; when depressurized the fluidic channel cross section opens. We find that when the main fluidic channel is loaded with a soft viscoelastic solid (e.g. E ~10kPa) the open/close response of the microfluidic channel changes significantly relative to the control case of a valve filled with water. The amount of deformation of the fluidic channel cross section (or, equivalently, the degree of deflection of the flexible PDMS membrane between the fluidic and air channels) is governed by the elastic modulus of the loaded material. We exploit this change in deformation to determine the Young's modulus of test samples. We use confocal imaging in the plane perpendicular to the bottom substrate to measure the deformation. To deconvolute the elastic response of the test material, we compare finite element analysis (FEA) of the stress-strain response of the simulated test device to the deformation measured on the confocal microscope. The comparison yields a unique determination of the test material's elastic modulus. When the air pressure resulting in membrane and material deformation is released, we find that the transient response of the PDMS membrane as it returns to its equilibrium position is governed by the viscoelasticity of the test material. Quantifying this transient

response with confocal microscopy yields a rapid estimate of the longest relaxation time of the test material.

Attributes of this flexible microfluidic rheometer are its simple fabrication and operation. By tuning the mechanical properties of the PDMS membrane (by changing its crosslink density), device can be prepared suitable for characterization of materials with a wide range of moduli (from 10^2-10^5 Pa) and relaxation times as small as ~1 s. The microfluidic design allows for microscale characterization using confocal microscopy, measurements of both linear and non-linear response and performance with small (~200pL) samples. The microfluidic format also allows for easy integration with multi-process lab-on-a-chip designs [29].

The organization of this chapter is the following: first, we present techniques to design, manufacture and characterize the device using confocal microscopy and FEA. We then determine the linear elastic (Young's) modulus and viscoelastic relaxation time of model gellan gum solutions. We compare the results with those acquired by means of conventional mechanical rheometry. Then, as an example application of the device to a soft viscoelastic solid, we characterize the elastic modulus and relaxation time of natively grown bacterial biofilms. These materials have proven difficult to characterize with conventional rheometers [30]. Finally we present quantitative recommendations for device design and fabrication for optimal study of the mechanical properties of soft matter with elastic moduli in the range ~0.1 - 100 kPa.

3.2 Methods and materials

3.2.1 Microfluidic device design and fabrication

To accomplish our aim we require a device fabricated from a flexible material with a chamber of well-defined geometry into which a test sample can be transported using microfluidics. We select the chamber volume to be ~25 x 125 x 75 μm^3 so that small material volumes can be studied. The top surface of the chamber is flexible so that a stress deformation profile can be applied to the loaded soft material. As introduced in the previous section, the stress imposed on the flexible membrane is generated by pressurized air applied to channels fabricated on a top layer of the device. These air

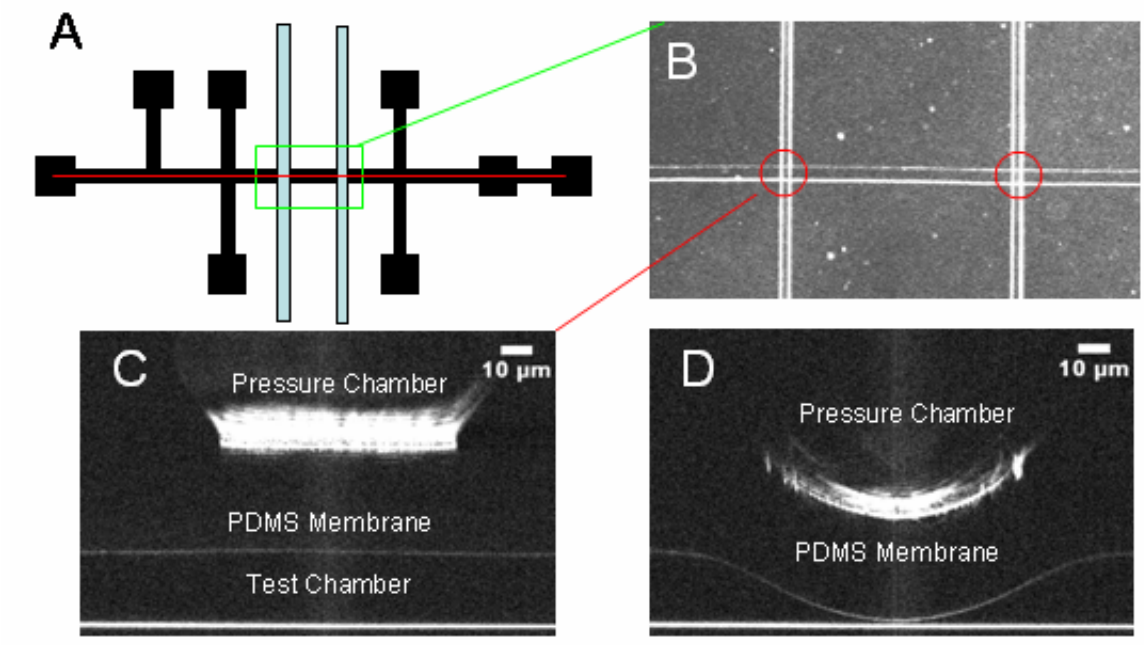

Figure 3.1: Here we show a schematic representation of the rheometer (A) with the dark test channel equipped with multiple ports and light-colored air channels. 1B shows a brightfield microscopy image of the test section (horizontal) with two actuation channels (vertical) with labeled testing sites. Here we provide images of the unpressurized chamber (C) and then pressurized (D) with full dynamic range of the actuated membrane in the plane perpendicular to the bottom substrate at the centerline of the device.

channels are fabricated by adapting the valve actuation technology of Unger et al [28]. The device is shown schematically in Fig 3.1a and a brightfield microscopy image after fabrication is shown in Fig. 3.1b. In Fig. 3.1b we show the horizontal test chamber with two vertical pressure chambers allowing for two test sites (circled) on the same device. The air pressure channel is 75 μm wide channel while the test chamber is ~25 μm high and ~125 μm wide (as seen if Fig. 3.1b).

In addition to the channel structure of Fig. 3.1a, b, the device has significant lateral structure comprised of tri-layered test chamber, flexible PDMS substrate and air channel. This layering along an axis perpendicular to the bottom substrate of the device is conveniently imaged with confocal microscopy, as shown in reflection mode in Fig 3.1c. For simplicity of measurement and ease of comparison with FEA, the device is comprised of channels with rectangular cross-section as opposed to the hemispherical channels used for valving by ref [27]. The particular geometry and dimensions were selected to achieve full actuation (closure) of the device at the center of the test chamber as shown in Fig. 3.1d.

A key component in the device design is the selection of the mechanical properties of the flexible substrate that will convey stress to the test material. Here we use corsslinked elastomeric PDMS (Dow Sylgard 184 Silicone Elastomer Kit) because we can tune the properties of the membrane by varying the cross-link density. This density is controlled by the ratio of elastomer base to curing agent included in the kit. The higher the ratio, fewer cross-links exist in the polymer, thus the lower the modulus. In typical valve applications (e.g. ref [27]) this ratio is 30:1 and the PDMS elastic modulus is then ~600-750 kPa [28, 31]. As discussed subsequently, the mechanical

properties of the PDMS membrane determine the range of moduli of soft viscoelastic solids that can be characterized by the device. Thus, we vary the PDMS mechanical properties across different devices to yield tools suitable to a particular material. To accomplish the variation, we produced devices with base to linker ratio that varied from the 30:1 value of Unger et al. to as high as 60:1. This variation leads to a PDMS membrane modulus that can be tuned from about 20kPa - 500kPa. This variability allows for a wide range of elastic moduli of test materials to be characterized.

The microfluidic device used for this study was manufactured using the rapid prototyping soft lithographic techniques developed by Duffy et al [32]. The steps to manufacture the device include (1) master fabrication (2) fabrication of the air channels and (3) the soft liquid/test channel, (4) adhesion of the two layers and finally (5) adhesion of the PDMS two-layered device to the glass bottom plate. These steps are outlined below with emphasis on methods unique relative to this study.

3.2.1.1 Master fabrication

The microfluidic channels of Figure 3.1 were produced as a master from which elastomeric PDMS devices were subsequently molded. Air and test channel masters were fabricated independently on 10cm silicon wafers (University Wafer, Boston, MA). The master was made using a photocurable polymer photoresist SU-8 2015 (MicroChem, Newton, MA). After cleaning the silicon wafer with acetone and isopropyl alcohol (IPA) (J.T. Baker, Phillipsburg, NJ) SU-8 2015 (source as above) was spin-coated onto the wafer at 2400 rpm for 30 s yielding a ~25 μm thick coating. The coated wafer was soft baked for 1 minute at 65ºC and 2 minutes at 95ºC. After soft bake the wafer was covered with a photomask of the fluidic channel design and exposed to ultraviolet light for ~30 s.

The wafer was then hard baked for 1 minute at 65ºC and 2 minutes at 95ºC and then developed in SU-8 developer solution (MicroChem, Newton, MA) for 3 minutes. The wafer was cleaned with IPA and dried with compressed air. The master wafers were then set aside for a minimum of 12 hours prior to further processing.

3.2.1.2 Air channel fabrication

Air channels were made by attaching the master wafer onto the bottom of a glass container using double-sided tape. A mixture of PDMS base and curing agent at a ratio of 10:1 (total weight ~50g) was mixed and degassed in a vacuum desiccator. This mixture was poured into the mold and degassed. The mold was cured at 70ºC for a minimum of 4 hours. Once cured the PDMS was cut into the final shape of the device and removed from the mold. One inlet was punched in each air channel. The PDMS device was cleaned with IPA and set aside to be adhered to the PDMS membrane of the test channel layer.

3.2.1.3 Fluidic test channel fabrication

We use a low curing agent density in the PDMS that forms the fluidic network because we require a flexible membrane to respond to the viscoelasticity of the test material. The low curing agent density yields tacky PDMS. In this case, a silane treatment of the master mold was required prior to pouring the PDMS to facilitate removal of the PDMS device from the mold. The wafer was heated 140ºC with a cover slip next to the wafer with 2-3 drops of (tridecafluoro-1,1,2,2-tetrahydrooctyl)-1-triclorosilane (United Chemical Technologies, Inc., Bristol, PA) on the glass. Both substrates were covered with a glass Petri dish for ~1 hour at temperature. The wafer cooled under the Petri dish until it could be handled.

PDMS elastomer base and curing agent were mixed at the appropriate ratio and degassed. To control the thickness of the membrane the PDMS was spin coated onto the silane treated mold at 2100rpm for 30 s. This operation resulted in a total thickness of PDMS of ~50 μm and, given the height of the SU-8 mold, a ~25 μm membrane. The coated wafer was then cured for 1 hour at 80ºC.

3.2.1.4 Adhesion of the two layers

To bond the air channel and test channel assemblies into a completed device we use reactive ion etching (RIE 2000, South Bay Technologies, San Clemente, CA). After semi-curing for one hour the PDMS coated wafer and previously fabricated air channels (bottom up) are oxygen plasma etched for 30 seconds. After opening the chamber the air channel PDMS blocks are mounted on the PDMS coated test channel wafer in the correct registry. Care is taken to ensure that all air is purged between the two layers by compressing the two substrates from one side to the other. The assembly is cured overnight at 40ºC.

3.2.1.5 Adhesion of the device to a glass substrate for confocal microscopy visualization

To allow for confocal microscopy with an inverted microscope the device assembly was adhered to a 45x50 mm No 1 (thickness 0.14-0.17 mm) glass coverslip (Fisher Scientific, Pittsburgh, PA). Prior to bonding the glass plate was cleaned with acetone and IPA and dried using compressed air. The two-layered device was then cut from the fluid test channel mold along the edge of the air channel block and carefully lifted from the mold. Sample ports were then punched in the two-layered assembly at the appropriate locations and the entire assembly was bonded to the glass.

The bonding technique used depended upon the mechanical properties of the PDMS. Devices produced of PDMS of 30:1 elastomer base to curing agent ratio were less tacky and were therefore bonded with RIE as described in Sec. 3.2.1.4. This step was unnecessary for devices produced from more compliant PDMS. In these devices a small drop of water was applied to the glass substrate to wet the fluidic test channels during adhesion to prevent the channels from collapsing due to interfacial forces. For this reason the fluidic channels of the devices fabricated of low modulus PDMS were kept filled with water until testing.

3.2.2 Confocal microscopy detection of flexible rheometer strain

To determine the deflection of the membrane in the microfluidic device we used confocal laser scanning microscope (CLSM, Leica TCS SP-2 with a DMIRE-2 inverted microscope). Images were acquired using a 100x N.A. 1.4 oil immersion objective. To produce images of the membrane deflection in a plane perpendicular to the bottom glass substrate, imaging was performed in the instruments xz scan mode along the center line of the device. The pixel size for these 512 x 512 scans was 98 nm yielding a typical image size of 50.2 x 50.2 μm^2. The image acquisition time was 0.848 s. To track the membrane deflection (as shown, for example in Fig. 3.1 c, d) images were acquired in reflection mode with incident light from an argon ion laser (488nm). Detection was with a photomultiplier tube over the range of 479-498nm. To measure the transient response of the device, typically a time series of 300 or 150 xz images was collected with time steps of 0.512 s or 0.848 s respectively. The deflection was measured by determining the distance between the top of the glass substrate and the bottom of the PDMS membrane. This corresponds to the thickness of the test material. The microscopy settings described

above yield a reflection signal due to the membrane of thickness ~8 pixels. Given this width we are typically able to locate the membrane position with a resolution of 3-5 pixels, corresponding to a deflection resolution of 0.5μm.

3.2.3 Operation of the flexible microfabricated rheometer

We perform both steady state and transient experiments with the device. The general mode of operation is to apply a fixed pressure to the air channels. This pressure yields a deflection of the PDMS membrane between the air channel and test material. The magnitude of the deflection depends on the mechanical properties of the test material. This deflection is recorded with a confocal microscope scanning in a plane perpendicular to the glass substrate. The pressure in the air channel is provided by a regulated nitrogen cylinder (Cryogenic Gases) attached to the inlet of the air channel and monitored with a digital pressure gauge (Ashcroft, 0-60 psi). The pressure applied depended upon the modulus of the test material. For stiff materials pressures as great as 15 psi were applied. For softer materials full scale deflection was achieved with pressures as small as 2 psi. In a steady state experiment a series of incrementally increasing air pressure is applied to the device. After the membrane deflection reached steady-state (t ~30 s - 60 s, typically), a confocal microscopy image of the membrane was acquired. The image scan was performed along the centerline of the device (as shown in Fig. 3.1a) such that the maximum deflection is recorded. For a transient experiment, the time-dependent membrane deflection was imaged after a step-change in air pressure was imposed.

Because the deflection of the flexible membrane is a function of both the test material and PDMS material properties, a control experiment to assess the response of the

device without the test material was required. To accomplish this characterization, we equilibrated the device (minimum of 30 minutes) with water in the test chamber. We then carefully imaged the device to determine its 3D geometry for later simulation using FEA. In the control experiment we typically applied at least 8 different pressures to the air channel and measured the steady-state deflection of the membrane at each pressure with the confocal microscope. This response is compared to the results of FEA to determine the (static) linear elastic modulus (E_0) of the elastomeric PDMS of the device. To address any potential issues with PDMS aging, we always performed this control experiment within 36 hours of an experiment with the test material.

3.2.4 FEA simulations

Because the microfluidic rheometer's principle of operation relies on the flexibility of the elastomeric PDMS of which the device is comprised, we modeled the deformation of this linearly elastic material so as to later apply this independent characterization to extract the mechanical properties of the test materials that we deformed in the device. We used FEA to accomplish this aim. The FEA methodology, combined with the control experiment, also improves the accuracy and precision of the rheometer by providing a simple means to account for device to device variations in geometry and PDMS material properties that inevitably result due to the variability of microfabrication.

Finite element analysis (FEA) was completed using a standard simulation tool for linear elastic analysis (Structural mechanics module of Comsol Multiphysics v 3.3a). We constructed the finite element mesh within the module by decomposing the device into three sub-domains, the dimensions each of which has been recorded by confocal

microscopy. The three sub-domains, each with different material properties, are (i) the air channel; (ii) the PDMS device surrounding the test channel and (iii) the fluidic test channel comprised of the test material. Typical mesh values over these sub-domains included 26,000 elements and ~ 90,000 degrees of freedom. The PDMS was modeled as a linear elastic material with unknown Young's modulus. The Poisson's ratio of PDMS is taken as $\nu = 0.45$, consistent with literature [31]. The volume modeled by FEA was approximately 4 x 4 x 0.05 mm^3.

The Young's modulus of the elastomeric PDMS of each device was extracted from results of the control experiment discussed previously. The pressure series applied in the control experiment was simulated for a range of different PDMS Young's moduli. The maximum deformation of the flexible membrane was extracted from the simulation at each pressure of the series. This deformation was compared to the deflection measured by confocal microscopy. The PDMS Young's modulus was taken as the value that best modeled the measured deflection at each of the applied pressures.

Typical results of this procedure are shown in Fig. 3.2. Fig. 3.2a plots the deflection of the membrane at different applied pressures (P = 3.4 kPa - 58.7 kPa) for a typical device geometry and E_{PDMS} = 350 kPa. The shape of the membrane agrees well with the simulated membrane deflection as measured by confocal microscopy and shown in Fig 3.2b. Fig 3.2c plots the experimentally determined maximum deflection normalized by the width of the air channel as a function of the pressure applied to the air channel. Figure 3.2c shows that for devices with PDMS of three very different compliances (or, equivalently, elastic moduli), the measured maximum deflection is a simple linear function of the applied stress. The curves plotted are the simulated

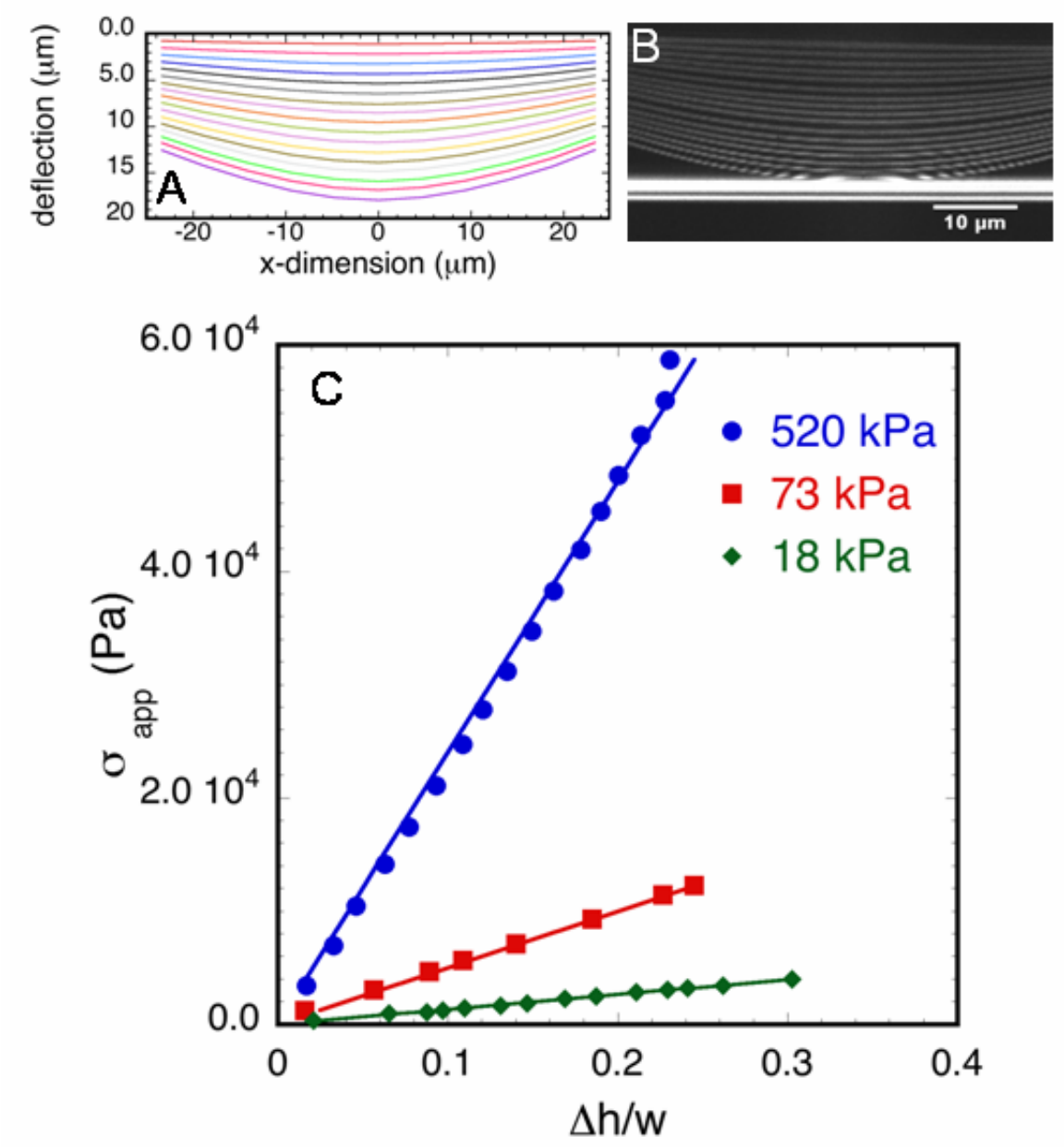

Figure 3.2: We compare the stress and strain of the device loaded with water to a Comsol Multiphysics simulation to determine the properties of the PDMS membrane. From FEA Fig. 3.2A shows the expected progression of the PDMS membrane. Fig 3.2B shows a similar progression on a device in the plane perpendicular to the bottom substrate at the centerline of the device. We compare the experimental deflection normalized by the width of the air channel at each pressure to the FEA simulation to extract the value of the elastic modulus of PDMS (C).

membrane deflection for the optimal Young's modulus of the PDMS membrane. The Young's moduli extracted from the simulations are consistent with the expected values given the amounts of cross linker used to produce the PDMS elastomer (e.g. one device characterized as E_0 = 520 kPa corresponds to a 30:1 ratio of elastomer base to cross-linking agent while a device characterized as an 18 kPa was comprised of elastomeric PDMS produced from a 60:1 ratio mixture).

Once the PDMS elastic modulus had been determined from the independent control experiment, FEA was also used to determine the unknown elastic modulus of a material loaded into the fluidic test channel. The measured deflection of the flexible membrane in this case was perturbed from the control experiment due to the elasticity of the test material. Of course the ability to resolve this difference in membrane response is a function of the relative values of the elastic modulus of the loaded material and that of the PDMS. That is, if the test material is much more compliant (lower modulus) than the PDMS, then the membrane deflection will not be significantly perturbed for the control case. Alternatively, if the PDMS is much more compliant than the test material, then the membrane will not significantly deform at all the typical air channel pressures. Intermediate between these two regimes, where $E_{\text{test sample}} \sim (0.01\text{-}1)\ E_{\text{PDMS}}$ is the optimal range of operation of the flexible microfluidic rheometer.

This situation is apparent from FEA simulation results as plotted in Fig. 3.3. Simulations were performed for a device of typical dimensions and typical PDMS elastic moduli (E = 25 and 50 kPa) and at a pressure (P = 3.8 kPa and 11.4 kPa respectively) for which the control experiment would yield a fully closed membrane ($\varepsilon = \Delta h/h_0 = 1$). Materials of Young's modulus varying from E = 10^2 Pa to 10^5 Pa were simulated in the

test section of the device. The simulated membrane deflection, plotted as a dimensionless strain, as a function of E_{test} is reported in Fig. 3.3. As shown schematically on the plot, (for a device with E_{PDMS} = 25 kPa) for a low modulus test material (E < 150 Pa) the strain is not resolvably different than unity. On the other hand, for a high modulus test material (E > ~ 20,000 Pa), the membrane deflection is not resolvably different than zero. However, for 150 < E_{test} < 20,000 Pa (or, equivalently 0.006 < E_{test}/E_{PDMS} < 0.8), a large, resolvable effect of the test material is observed. (Fig. 3.3 also shows that by increasing the device modulus this range is shifted to the right.)

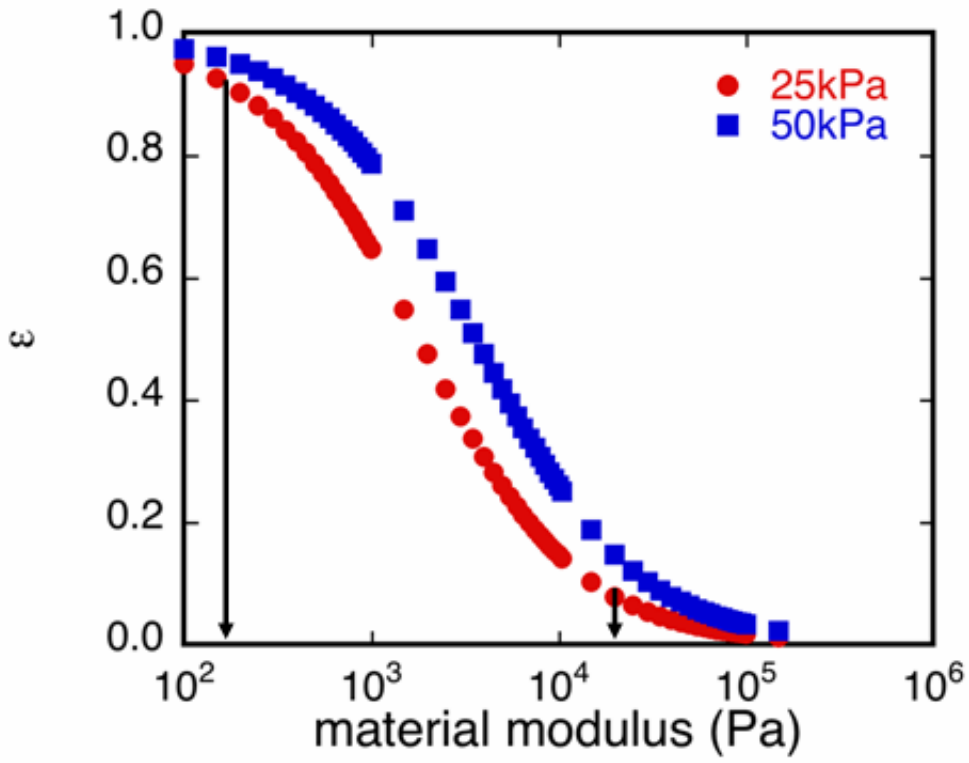

Figure 3.3: We plot the results of an FEA simulation at the pressure required for full-scale actuation (closure) of a device of typical geometery for two different PDMS elastic moduli loaded with material's that vary in elastic modulus by several orders of magnitude. The asymptotic limits of the material property resolvability are clearly shown at either end of the 25 kPa curve.

3.2.5 Rheometry

We compare results from the flexible microfluidic rheometer to tests performed with a stress-controlled rheometer (AR G2, TA Instruments, New Castle, DE). To determine the (Young's) linear elastic modulus in a manner consistent with the microfluidic experiments, the steady-state stress-strain response of 2 and 3% (w/w) gellan gum was measured in a compression experiment with a 40 mm flat plate. Steady-state behavior was confirmed by monitoring the response over 5 minutes. To measure the longest relaxation time of the gellan gum, a (shear) creep experiment was performed with a 60 mm 2º cone geometry. A shear stress (50 Pa, in the linear regime) was applied for 150 seconds and then the elastic recoil was observed after the stress was released. The device was equipped with a Peltier heater to facilitate the loading of the gellan gum solutions.

3.2.6 Gellan gum solutions

To evaluate the performance of the device, we compare results of model gellan gum solutions in the flexible microfluidic rheometer to those from a conventional rheometer. Gellan gum (food grade Kelcogel (Lot # 4E0783A, CP Kelco, Chicago, IL) was prepared in 2% and 3% (w/w) solutions according to the manufacturer. Briefly, dry gum powder was added to distilled, deionized water at the desired weight fraction. This solution was mixed on a vortexer and then heated to 70ºC for one hour so as to yield a transparent liquid solution that was easily loaded into either the microfluidic or conventional rheometer.

3.2.7 Biofilms

To demonstrate microscale characterization of a structurally heterogeneous soft viscoelastic solid two different strains of bacteria, *Staphylococcus epidermidis* RP62A (obtained from ATCC, catalog number 35984) and *Klebsiella pneumoniae* LM21(a gift from Christine Forestier, Universite d'Auvergne-Clermont, Clermont, France) [33, 34]. In both strains the microfluidic device was seeded with the bacteria first grown on Luria-Bertani (LB) agar plates for ~24 hours at 37ºC. Individual colonies were harvested and then grown in LB broth on a 1 cm radius orbit shaker/incubator (model 435, Thermo-Forma, Marlette, OH) at temperature and a speed of 200 rpm until mid-log phase growth. This suspension of bacteria in broth was then added to the microfluidic device and incubated for one hour. After incubation LB broth was used as a growth medium in the device and flowed using a syringe pump (Harvard Apparatus, Holliston, MA) at 0.1mL/hour for a minimum of 18 hours in the incubator at 37ºC. We choose biofilms to study in the microfluidic rheometer for the following reasons: the viscoelastic properties of biofilms are difficult to determine using conventional rheology [30, 35] (i.e. their microscale structure requires rheological measurements at length scales of the flexible microfluidic rheometer [36]); these length scales are also similar to those found in capillaries of the vascular system [37]; many biofilms show viscoelastic response in a range suitable for our device [38]; finally the microfluidic environment allows for *in situ* growth of the biofilms at shear rates consistent with those found in the cardiovascular system and *in situ* fluorescent labeling for imaging.

3.3 Results

The organization of results is the following: In the first section we characterize the elastic modulus and longest viscoelastic relaxation time of gellan gum, a model soft viscoelastic solid that can be produced in quantities sufficient for conventional mechanical rheometry. We compare the results of the steady-state and transient response of gellan gum in the flexible microfluidic rheometer to conventional rheometry. We then characterize the material properties of bacterial biofilms using the microfluidic rheometer. For reasons discussed above the flexible microfluidic rheometer is well suited to study the previously elusive material properties of biofilms. For each material we consider in separate sections steady-state and transient measurements with the flexible microfluidic rheometer.

3.3.1 Gellan Gum Studies

3.3.1.1 Steady-state measurements of the static elastic modulus, E_0

Figure 3.4 reports the steady-state response of 2.0% (w/w) solutions of gellan gum to a series of applied pressures in the flexible microfluidic rheometer. As described in the methods, incrementally increasing pressures were applied to the air channel. The applied pressure stresses the flexible PDMS membrane above the sample, thereby yielding a deflection of the membrane that is a function of the static elastic modulus of the PDMS and of the gellan gum. At each pressure, the steady-state membrane deflection (data acquired for $t > 1$ min after application of the pressure) was recorded by confocal microscopy. Figure 3.4a plots the steady-state strain, ε, measured for each pressure. (For consistency with the typical way of reporting mechanical property characterization, here and in subsequent figures we plot the strain measure $\varepsilon = \Delta h/h_0$, where Δh and h_0 are the

measured deflection and undeformed height of the fluidic channel respectively, as the abscissa and stress as the ordinate; however, note that in the experiments it is stress that is controlled and the strain that is measured.) We find that the data of Fig. 3.4 are sufficient to determine the static elastic modulus of the gellan gum samples.

For comparison, we also show the deflection of the PDMS membrane measured in the control experiments for the same device used to characterize the 2.0% gellan solution. This comparison clearly shows the significant differences in the deflection of

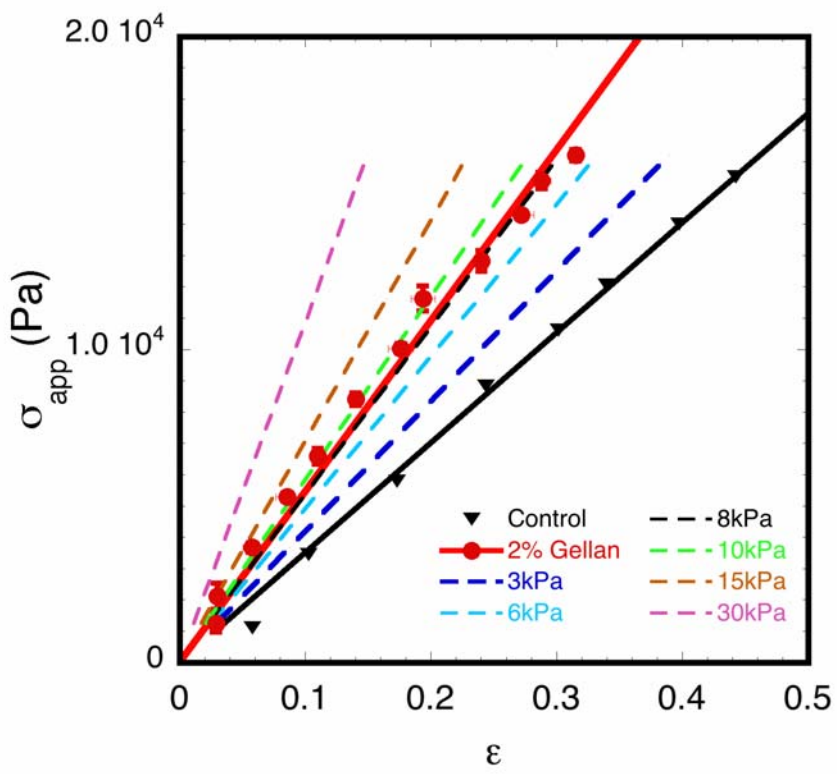

Figure 3.4: Using FEA to determine the elastic modulus of gellan gum. To find a unique solution, we match the slope of the linear fit of the experimental data to the slope of the FEA solution. Here we show that an 8kPa material will behave similar to 2% gellan gum loaded into the device.

the device loaded with the elastic gellan gum vis a vis the control experiment, loaded with water. This difference is a direct consequence of the material properties of the gellan gum, as we now show. First the control deflection response is compared to the

results of finite element analysis to determine the elastic modulus of the PDMS membrane for the particular device as discussed in Sec 3.2.4 and Fig 3.2c. The result, plotted as a solid line in Fig. 3.4 indicates that a PDMS static elastic modulus of 320 kPa is in good agreement with the measured deflection response. This value is then used as an independent input into the multilayer FEA simulation of the combined gellan/PDMS response of the loaded device. The deformation response of the 2.0% gellan gum in the PDMS device is simulated for a range of candidate static moduli of gellan gum (dashed lines). The static modulus that best models the data, E_0 = 8.0 kPa is plotted along with the linear fit of the experimental data.

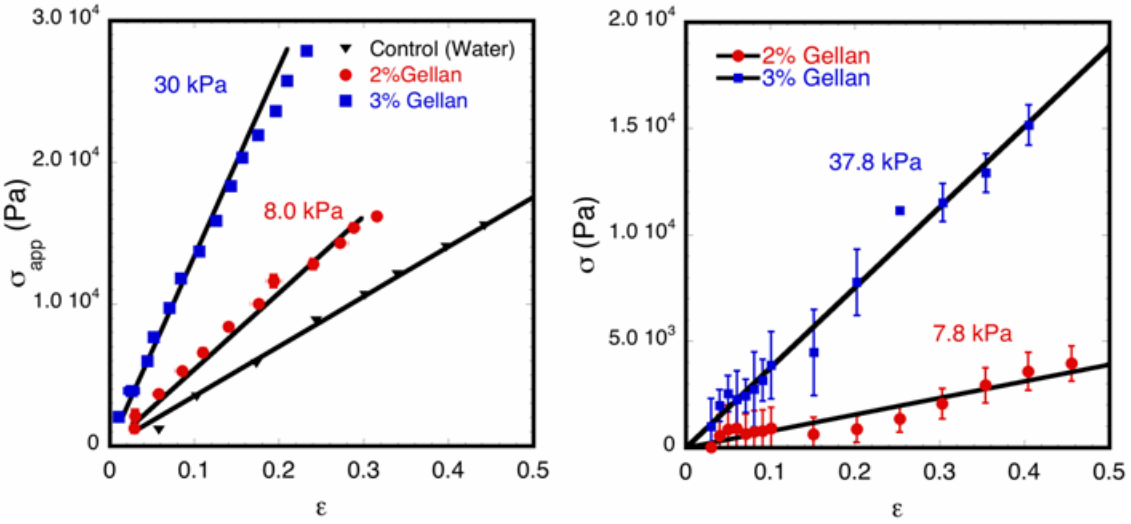

Figure 3.5: Here we show the experimental deflection of 2 and 3% (w/w) gellan gum solutions loaded into the microfluidic rheometer (A). We also report the unloaded response (Control) of the PDMS membrane of the device used to characterize the 2% gellan gum solution (same for 3% not shown for clarity) proving good separation in deflection for loaded and an unloaded device. The line fits are data from the FEA deformation with elastic modulus 8kPa and 30kPa simulated in the test channel. These values are in good agreement with the slope of the conventional rheometer studies reported in 3.5B.

Figure 3.5a reports the analysis of Fig 3.4 applied to 2.0% and 3.0% gellan solutions. The datum points are the mean of five independent experiments. The curve

plotted is the best estimate of the static modulus of the gellan materials determined from FEA (per the method in Fig. 3.4). Error bars are standard error of the mean. Note that the linearity of the stress/strain data, as well as the good agreement with the simulations method which is itself based on linear elasticity, confirms that these measurements are performed within the linear elastic limit. From the analysis of Fig 3.5, the flexible microfluidic rheometer determines the static elastic modulus of 2.0% and 3.0% gellan are 8.0 ± 0.2 and 30 ± 1 kPa, respectively.

Fig. 3.5b indicates results from conventional rheometry, in which normal stresses are plotted for 2.0 and 3.0 wt% gellan gum. This experiment is a good approximation of the compression test performed in the microfluidic device. The error bars are the standard error of the mean from four independent measurements. The static (linear) elastic modulus of the material is the slope of the stress-strain curve. From this slope, conventional rheometry determines the 2 wt% and 3 wt% gellan gum moduli to be 7.8 ± 0.5 kPa and 38 ± 0.9 kPa, respectively. The relative error between microfluidic and conventional rheometry for the 2% gellan gum is thus 2.5%. The relative error for the 3% gellan gum is 21%. These relative errors establish the capabilities of the flexible microfluidic rheometer for assessment of the static elastic modulus of soft viscoelastic solids.

3.3.1.2 Transient strain response of gellan gum

Fig. 3.6a reports the transient strain response of the PDMS membrane in contact with a 2.0 wt% gellan gum sample when the initial applied stress of 16 kPa is released. Not shown is the control response for the recoil of the elastomeric PDMS membrane without test sample - in this case the membrane returns to its equilibrium position in less

than 2 s. Thus, the membrane response is retarded by orders of magnitude by the effect of the loaded viscoelastic material. Each datum plots the average of the measured strain for five independent experiments at each time step ($\Delta\tau$ = 0.512 s) after the step decrease in pressure in the air channel. Error bars are the standard error of the mean value of the five measurements. The transient response follows an exponential decay to the original thickness of the material (ε = 0) that is well modeled as a single exponential function as shown by the solid curve in the figure. From the characteristic time of the exponential decay we estimate the longest relaxation time of the 2.0 wt% gellan gum to be 19.4 $\pm$ 0.9s.

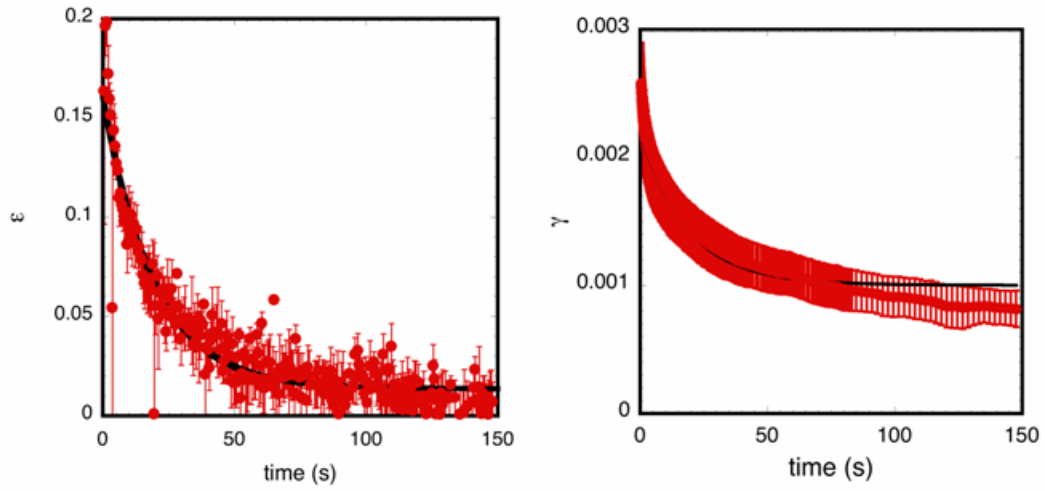

Figure 3.6: We report the transient response of the elastomeric PDMS membrane in contact with 2% gellan gum after the pressure is released (A). By fitting the results to an exponential decay, we determine the characteristic relaxation time (19.4 s). Fig 3.6b reports the recoil of a 2% gellan gum solution after a shear stress (50 Pa) was applied for 150 s on a conventional rheometer with an overlay of an exponential decay with the characteristic time reported in the transient response of the microfluidic rheometer.

To test the accuracy of this result, we applied a shear stress of 50 Pa (in the linear regime) to 2.0 wt% gellan gum for 150 s in a conventional rheometer. Figure 3.6b reports the recoil of the gellan gum sample after this stress is released. As for the flexible microfluidic rheometer an exponential decay of the strain is apparent in the data. Error

bars indicate the standard error of the mean of three independent measurements. The curve plotted is the predicted response of a single exponential decay with a characteristic relaxation time of 19.4 s, as taken from the results of the flexible rheometer in Fig. 3.6a. The agreement between the viscoelastic response predicted by the flexible rheometer and the results of conventional rheometry is very good. Thus the transient response of the flexible microfluidic rheometry provides a rapid method to characterize the longest viscoelastic relaxation time of soft viscoelastic solids.

3.3.2 Characterization of bacterial biofilms

Having established the performance of the flexible microfluidic rheomter for characterization of the elastic modulus and viscoelastic relaxation time, we apply the method to study a soft viscoelastic solid that is difficult to characterize by other methods: bacterial biofilms. These materials are well suited for flexible microfluidic rheometry for several reasons. First, heterogeneities in the structure make them difficult to study with conventional rheometry [30, 38, 39]. These heterogeneities exist on scales as large as 100μm [36, 40, 41]. Thus, microscale characterization can potentially resolve differences in the mechanical properties of biofilms on these scales. Second, the 10 - 100 μm scales of the microfluidic rheometer are equivalent to those of the cardiovascular system in which it is thought that bacterial biofilms may circulate [42, 43]. Finally, bacterial biofilms of clinical interest are thought to display elastic moduli characteristic of soft viscoelastic solids that this device was designed to resolve [38]. Thus, in this section we apply the flexible microfluidic rheometer to characterize the elastic modulus and longest relaxation time of natively grown biofilms.

3.3.2.1 Steady-state static elastic modulus determination of biofilms

Fig. 3.7 shows *Staphylococcus epidermidis* biofilm loaded into the test chamber. The bacteria are labeled with SYTO-9 dye (Invitrogen, Carlsbad, CA) for fluorescence imaging of individual organisms. The biofilm completely fills the test area as shown in the plane parallel to the bottom plate in Fig. 3.7a (image dimensions 150μm x 150μm). The biofilm also fills the entire test area in the plane perpendicular to the bottom plate as in Fig 3.7b (h_0 = 26.2 μm). As the applied pressure is increased the biofilm thins in response to the deformation of the elastomeric PDMS membrane as shown in Fig 7b-d.

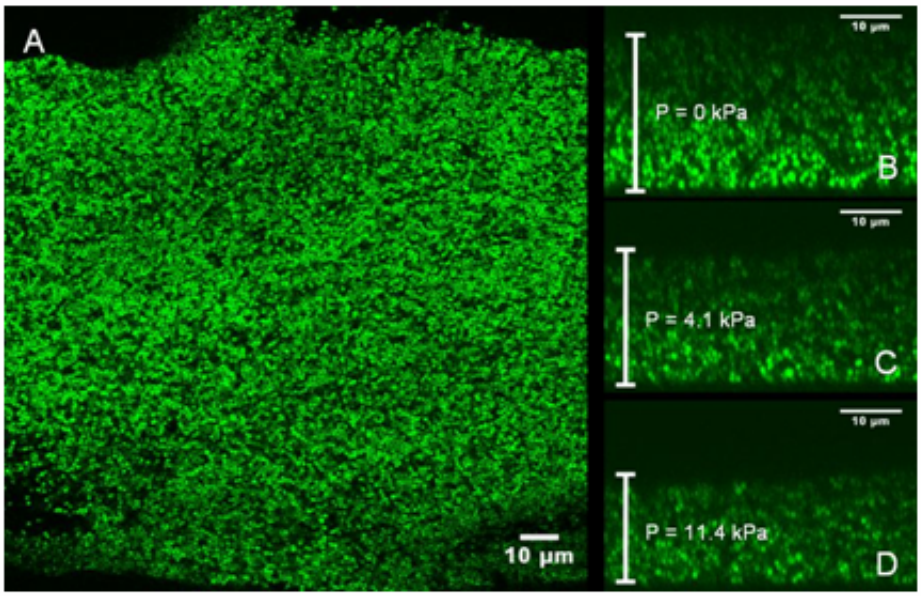

Figure 3.7: CLSM images of *S. epidermidis* biofilm loaded into rheometer. We show a dense biofilm of the bacteria labeled with Syto-9 in the plane parallel to the bottom substrate using fluorescence microscopy (A). Fig B-D show the microscale structure of the biofilm in response to the deformation of the PDMS membrane in the plane perpendicular to the bottom substrate at the centerline of the flexible microfluidic rheometer.

At the final applied pressure (P = 11.4 kPa), the height of the film at the point of maximum membrane deflection is 15.8 μm. In these and following figures each locus of

fluorescence intensity in the image is due to emission from a single bacterium of the biofilm. The fluorescence images of Fig. 3.7 show that the biofilm microstructure responds to the forcing of the flexible membrane in a way that can be used to extract mechanical properties, just as was accomplished for the gellan gum samples.

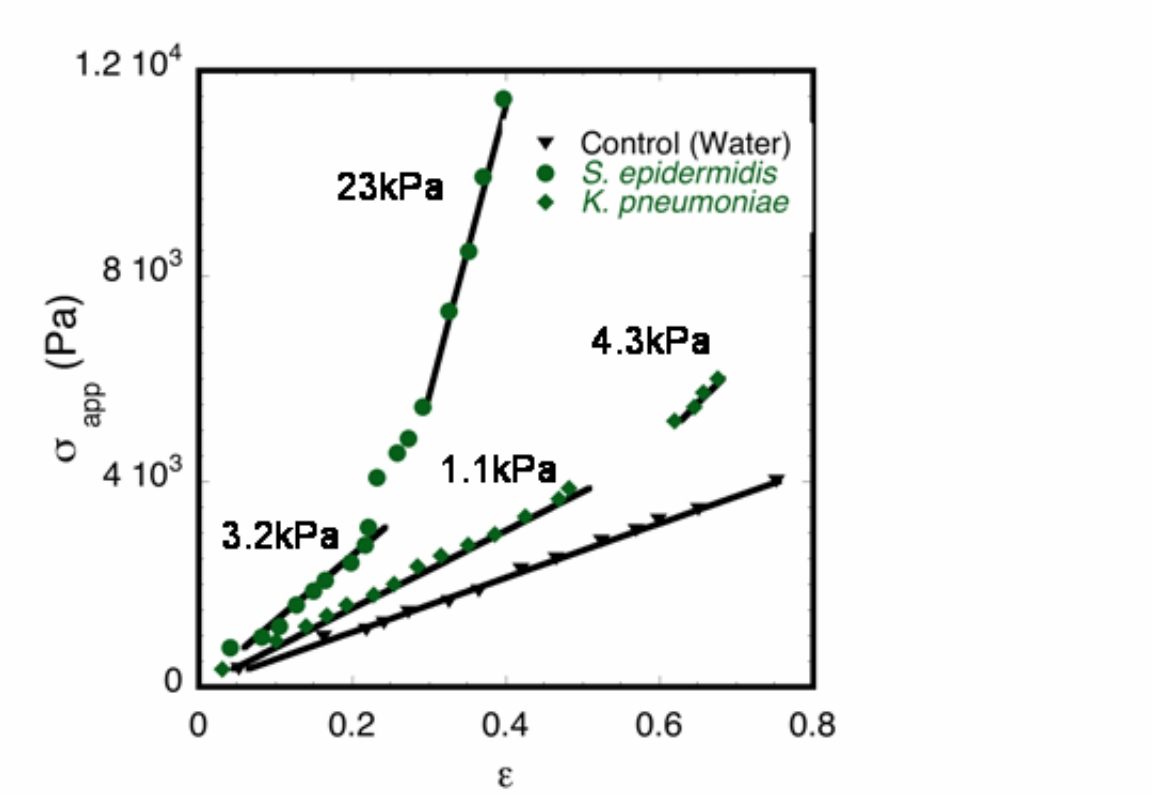

Figure 3.8: We report the deflection normalized by the initial height of biofilms grown in the device from two different species: *S. epidermidis* and *K. pneumoniae*. The FEA at the given elastic moduli provides estimates of the elasticity of the biofilms. Interestingly both films show an increase in elastic modulus, providing evidence of strain hardening. This increase in modulus is quantified using FEA.

Figure 3.8 plots the steady-state response (t ~ 30 s) for both *S. epidermidis* as well as *Klebsiella pneumoniae* biofilms subjected to the protocol reported in Fig. 3.7. As for the case of gellan gum, the control response is plotted on the figure to indicate a difference in the response between the loaded and unloaded device. In both cases the soft material stress-strain response is complex. At low applied strains a region of linear

behavior is observed. At higher strains a transition to a strain hardening behavior is found. Below we analyze these data with the methods reported for gellan gum to extract the elastic moduli of the biofilms in these two regimes.

First, we analyze the low-strain response. Using the method outlined in Sec 3.2.4, we determined the static elastic modulus of the PDMS membrane from the control response (not shown for *K. pneumoniae* device). By applying the same analysis used for gellan gum (c.f. Fig. 3.4), we found the best estimate of the low-strain (linear) static elastic modulus of *S. epidermidis* to be 3.2 kPa and for *K. pneumoniae* to be 1.1 kPa.

Next, we analyzed the interesting strain hardening response observed at high strains for both biofilms. For *S. epidermidis* the transition to strain hardening occurs at $\varepsilon \sim 0.2$. To extract an effective high strain elastic modulus we applied the FEA procedure of Sec. 3.2.4 and Fig. 3.4 to the high strain regime as shown in Fig. 3.8. This response is consistent with a high strain elastic modulus of 23 kPa, an order of magnitude greater than the low strain elastic modulus. *K. pneumoniae* displays a similar transition to strain hardening at $\varepsilon \sim 0.5$. Here the FEA estimates that the high strain elastic modulus increases 4-fold, from 1.1 kPa to 4.3 kPa.

Strain hardening in bacterial biofilms has not previously been reported as shown here. Cense et al. report increasing modulus in biofilms from measurements with the microindentation device, likely due to experimental procedures [27]. This mechanical response has potential implications for processes such as transport and clearance of biofilms from natural, manmade, or physiological aqueous environments.

3.3.2.2 Transient strain response of viscoelastic biofilm

The flexible microfluidic device was used to characterize the longest viscoelastic relaxation time of a *S. epidermidis* biofilm according to the methodology applied for gellan gum in Sec. 3.1.2. Figure 3.9 plots the transient response of the *S. epidermidis*

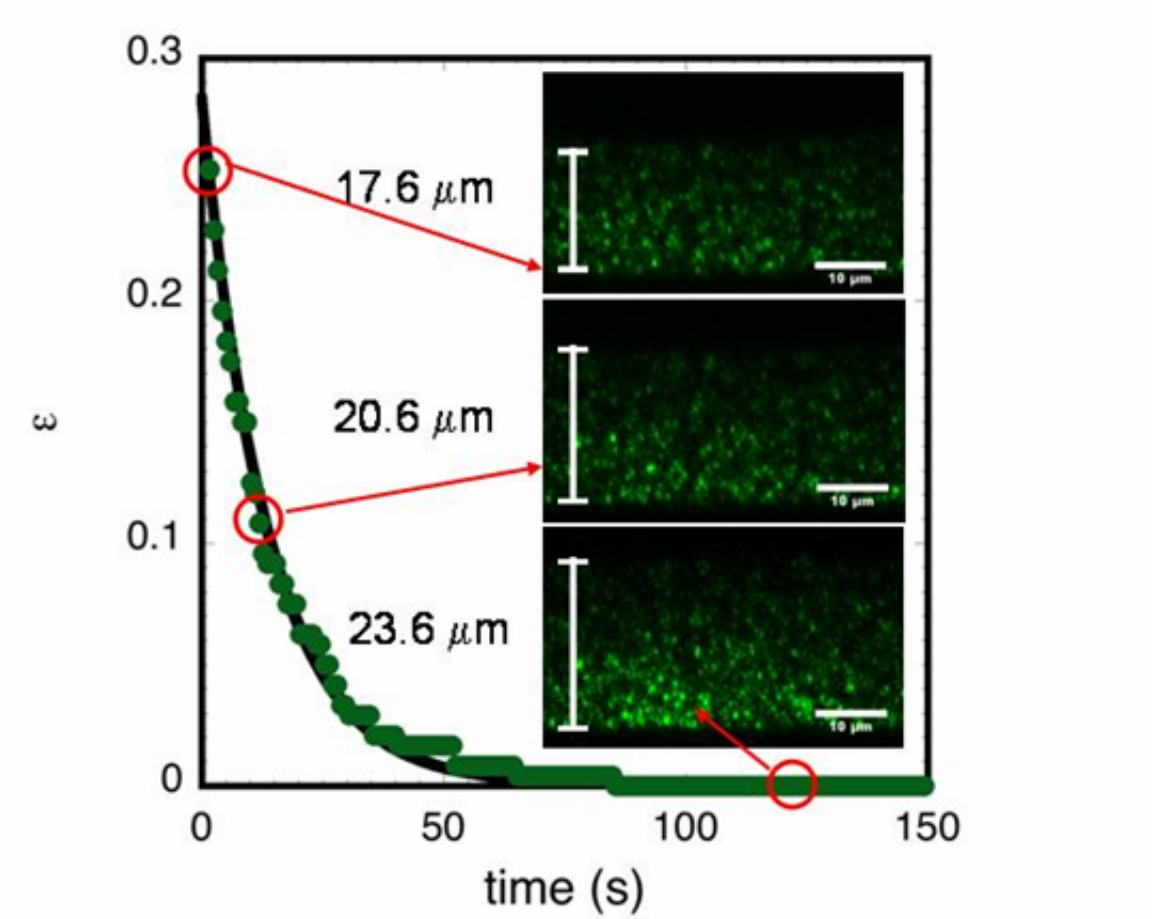

Figure 3.9: We plot the transient response of the PDMS membrane in contact with a *S. epidermidis* biofilm loaded into the channel after the pressure is released. We report exponential decay of the membrane to its original location with a characteristic time of 13.8s.

film upon release of the applied pressure. We monitor the response of the elastomeric PDMS membrane for 150 s after the step response in stress ($\Delta\tau$ = 0.848 s). The transient response is well modeled by a single exponential decay with a characteristic relaxation time of 13.8 s, much more rapid than 1100 s reported in literature [38]. The inset images

show the microstructure of the biofilm during three different time steps of the recoil. (The images were acquired in the plane perpendicular to the bottom plate of the device). In addition to showing the microstructural response, the images confirm that the biofilm adheres to both the top and bottom substrates during the transient recoil.

3.4 Discussion

The results demonstrate that the Young's modulus and transient strain response of materials can be characterized in a flexible microfluidic device by integrating FEA and confocal microscopy. The results from gellan gum experiments provide good agreement to those from conventional rheology. The elastic response of the biofilms agrees well with ranges presented in rheological reviews of other biofilm systems, while the transient response does not match the reported values [38]. We also reported strain hardening in biofilms.

The following sections address device capabilities and potential future improvements, new material property characterization of biofilms and finishes with recommendations for applying the method to other soft viscoelastic solids.

3.4.1 Device capabilities and potential future improvements

While we chose gellan gum as a model material for soft viscoelastic solid material property characterization, its structure can be quite complex. Gels that have been formed by cooling during shear flow have been found to have more uniform structures and therefore different material properties than quiescently cooled samples [44]. Thus, to ensure material uniformity for conventional rheometry we applied a shear flow at 10 s^{-1} applied to the sample as it was cooled from 70ºC to 20ºC. As an example of this effect, shear-cooling 3% gellan gum reduced the measured static elastic modulus by ~10kPa.

This same condition was accomplished on the flexible microfluidic rheometer by pre-heating the device in a water bath and cooling while loading the sample. If needed more stringent temperature controls may be added similar to those found in lab-on-a-chip applications [45]. The design of the microfluidic rheometer is thus conducive to the development of sample preparation protocols that combine thermal and shear profiles.

As discussed in Sec. 3.4.1 a 3D finite element simulation of multiple linear elastic regions is used to model the device and thereby determine the static elastic moduli of test materials. This methodology worked well for the cases considered in this manuscript; however, in order to extend the usage of the flexible microfluidic rheometer to other classes of materials, modeling the device response for the more general case of non-linear viscoelasticity would be of interest. In addition to models of elastoplastic and hyperplastic materials available for Comsol Mulphysics and other FEA software [46] that could be implemented, other simulation methods and tools could be applied [47, 48].

The flexible microfluidic device could also be operated to address frequency dependent viscoelasticity of soft viscoelastic solids by application of a sinusoidal variation in applied membrane pressure. The amplitude and phase lag of the membrane response could then be monitored by CLSM. Data analysis would then proceed as for current methods used in mechanical rheometry [10]. Of course a general limitation to acquisition of time dependent data such as described is the time resolution of the CLSM. For example, for our instrument the fastest image acquisition rate is ~ 0.5 Hz. To address this limitation, faster confocal microscopes are available [49]. The method requires measurement of the membrane deflection. This measurement can be performed by means other than confocal microscopy, such as laser reflection [50].

3.4.2 New material property characterization of biofilms

The low-strain Young's modulus of *S. epidermidis* and *K. pneumoniae* determined from the device is similar in magnitude to the shear modulus previously reported for *S. mutans* and *P. aeruginosa* [38]. The majority of the biofilms that were studied had shear moduli much lower than 1 kPa. One potential difference between the work here and this prior work is the effect of heterogeneity. Because for our system the Young's modulus is determined for a small homogeneous sample of biofilm, the potential for direct connection between molecular and genetic structure and mechanical properties is greater with these measurements than for measurements by macroscopic rheology. That is, by using the microfluidic environment we have characterized these materials at length scales that were previously inaccessible. Also by applying confocal microscopy, we collected complementary visual evidence of the microstructure of the system upon compression. This characterization leads to a report of strain hardening in biofilms. As shown in Fig 3.8 both *S. epidermidis* and *K. pneumoniae* harden upon applied strain. A similar effect was found in the microindentation device, but was thought to be caused by a change in the biofilm from one experimental series to the next [27]. This evidence of hardening can be critical to understanding the fate of biofilms in the many environments they inhabit.

The transient viscoelastic response of the biofilm is much more rapid than that reported by Shaw et al. They determined a common elastic relaxation time of 1100 s for several different biofilms [38]. However in our case the transient response of the elastomeric PDMS membrane adhered to a *S. epidermidis* film yields a characteristic relaxation time of 13.8 s. This is the time it takes for the strain-hardened film to return to

its original shape. The difference in time scales is evidence of the structural differences in the biofilms found in literature and the strain-hardened biofilm in the flexible microfluidic rheometer.

3.4.3 Recommendations for applying the flexible microfluidic rheometer to the characterization of other soft viscoelastic solids

Our device combines microfluidic assembly techniques and FEA to provide a simple method for characterizing soft viscoelastic solids with moduli in a range difficult to study with current alternative methods discussed in Sec 3.1. In this section we give recommendations for applying this method to other soft viscoelastic solids by means of Fig. 3.10. Fig. 3.10 reports the FEA determined strain response of a 25μm thick PDMS membrane and a 25 μm thick test material at the pressure required for full dynamic range (closure) of the empty device at a given PDMS modulus. The measured strain was determined over a range of moduli of the test material. The upper and lower curves are based on the known resolution limits of the flexible rheometer. The lower limit of measurability (left hand curve) is for a resolution limit of strain $\varepsilon = 0.92$ because this strain is equivalent to a 4 μm difference in full-scale deflection for the unloaded vs. the loaded device. The 4 μm limit is about an order of magnitude greater that the resolution limits of the confocal microscope. The upper limit of measurability is given by requiring that the full-scale actuation pressure in the air channel be no greater than 10% of the test material modulus. This limit addresses the resolution limit where at the strain generated by the applied pressure required for full closure in the unloaded device would yield an undeformed membrane (approaching $\varepsilon = 0$). Fig. 3.10 indicates that a test material elastic modulus varying by ~ 2 orders of magnitude can be measured in a device microfabricated

with a PDMS membrane of one specific modulus. The limits of the range shift (to the right) as the elastic modulus of PDMS increases. To determine the stiffness of PDMS needed to test a new material, an estimate of the unknown test material's modulus need

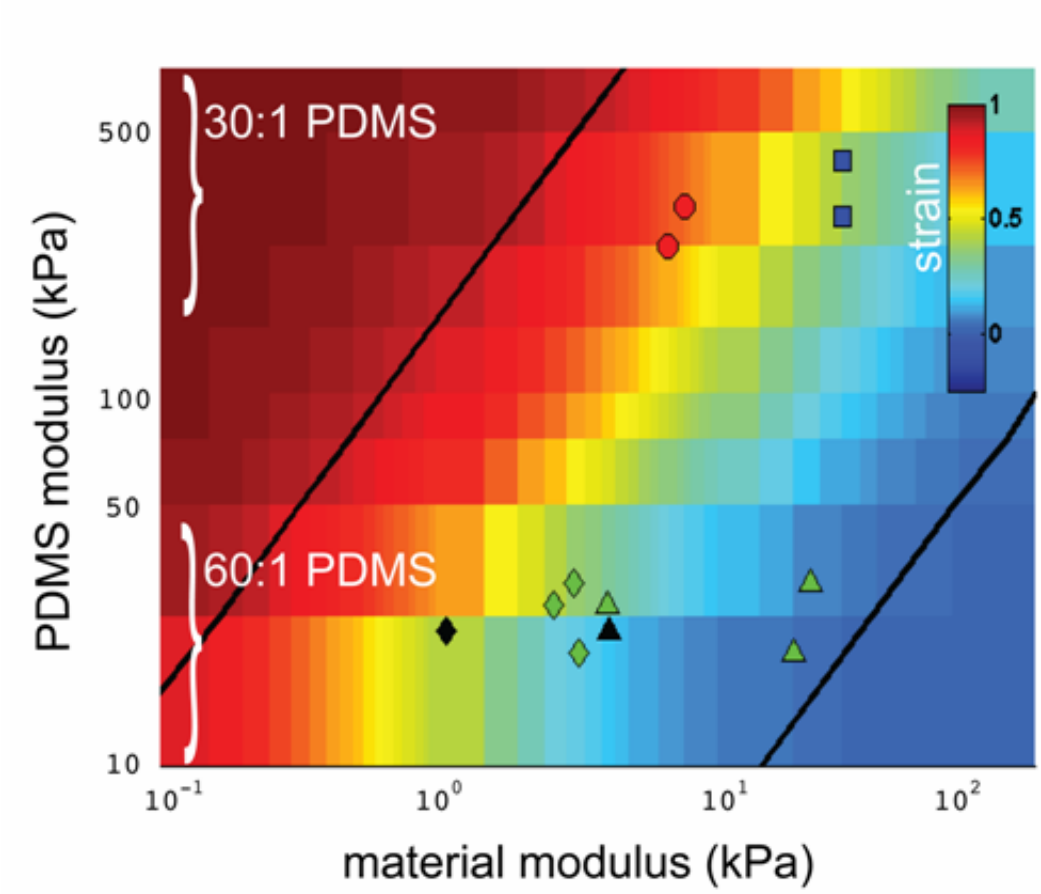

Figure 3.10: We report the strains associated with several dual layered systems using the FEA simulation. We display resolvability limits associated with the device. We also include an estimated range of elastic modulus values for different ratios of PDMS elastomer base to cross-linking agent. Finally we have included data from several experiments: 2% (●) and 3% gellan (■) *S. epidermidis* (♦) and one *K pneumoniae* (♦) biofilm. We also give the values associated with the hardening effects shown in Fig. 3.8 (▲ and ▲).

only be accurate within an order of magnitude. Fig. 3.10 also reports an estimated range of elastic moduli for 30:1 and 60:1 PDMS elastomer base to cross-linking agent ratios. This range provides a guideline to determine the appropriate ratio of elastomer base to

cross-linking agent required to fabricate a flexible microfluidic rheometer to determine the test material modulus within an estimated range.

Included in the figure are data from the experiments discussed in this paper. Results for 2% (circle) and 3% (square) gellan gum were made in two different devices each. Despite differences in device PDMS characteristics, the resulting test moduli are acceptably similar ($\pm$ 2.5% relative error). We also report the strain response for three different *S. epidermidis* films and the *K. pneumoniae* film. The low-strain elastic modulus is given by a diamond, while the high-strain modulus (due to strain hardening) is shown with a triangle. As in the case of gellan gum, the differences in elastic modulus of the PDMS membrane do not affect the measured moduli of the biofilms, even for the strain-hardened regime.

3.5 Conclusions

This chapter outlines a new method to determine the elastic modulus and transient response of soft viscoelastic solids. We have created a flexible microfluidic rheometer to test soft viscoelastic materials in ranges inaccessible by current microscale techniques. We tested the capabilities of the device using homogenous gellan gum samples. These results agreed well with similar studies using conventional rheology. The device was also used to determine the elastic moduli of soft viscoelastic bacterial biofilms. We report strain hardening in these systems, a result that may provide insight into clearance of these biofilms from the cardiovascular system. Finally we provide recommendations on design considerations for using the flexible microfluidic rheometer on new soft viscoelastic solids.

References

1. Steinhaus, B., A.Q. Shen, and R. Sureshkumar, *Dynamics of viscoelastic fluid filaments in microfluidic devices.* Physics of Fluids, 2007. **19**(7).
2. Bredbenner, T.L. and D.T. Davy, *The effect of damage on the viscoelastic behavior of human vertebral trabecular bone.* Journal of Biomechanical Engineering-Transactions of the Asme, 2006. **128**(4): p. 473-480.
3. Keller, M.W. and N.R. Sottos, *Mechanical properties of microcapsules used in a self-healing polymer.* Experimental Mechanics, 2006. **46**(6): p. 725-733.
4. Drelon, N., et al., *Influence of tempering on the mechanical properties of whipped dairy creams.* International Dairy Journal, 2006. **16**(12): p. 1454-1463.
5. Lee, J., et al., *The effect of gelatin incorporation into electrospun poly(L-lactide-co-epsilon-caprolactone) fibers on mechanical properties and cytocompatibility.* Biomaterials, 2008. **29**(12): p. 1872-1879.
6. Nissi, M.J., et al., *Estimation of mechanical properties of articular cartilage with MRI - dGEMRIC, T-2 and T-1 imaging in different species with variable stages of maturation.* Osteoarthritis and Cartilage, 2007. **15**(10): p. 1141-1148.
7. White, S.R., et al., *Autonomic healing of polymer composites.* Nature, 2001. **409**(6822): p. 794-797.
8. Hsiong, S.X., et al., *Differentiation stage alters matrix control of stem cells.* Journal of Biomedical Materials Research Part A, 2008. **85A**(1): p. 145-156.
9. Holyst, R., *Some features of soft matter systems.* Soft Matter, 2005. **1**(5): p. 329-333.
10. Ferry, J.D., *Viscoelastic Properties of Polymers*. 3rd Edition ed. 1980, New York: John Wiley and Sons.
11. Solomon, M.J. and Q. Lu, *Rheology and dynamics of particles in viscoelastic media.* Current Opinion in Colloid & Interface Science, 2001. **6**(5-6): p. 430-437.
12. MacKintosh, F.C. and C.F. Schmidt, *Microrheology.* Current Opinion in Colloid & Interface Science, 1999. **4**(4): p. 300-307.
13. Gisler, T. and D.A. Weitz, *Tracer microrheology in complex fluids.* Current Opinion in Colloid & Interface Science, 1998. **3**(6): p. 586-592.
14. Mason, T.G., et al., *Particle tracking microrheology of complex fluids.* Physical Review Letters, 1997. **79**(17): p. 3282-3285.
15. Crocker, J.C., et al., *Two-point microrheology of inhomogeneous soft materials.* Physical Review Letters, 2000. **85**(4): p. 888-891.
16. Mason, T.G., et al., *Rheology of F-actin solutions determined from thermally driven tracer motion.* Journal of Rheology, 2000. **44**(4): p. 917-928.
17. Shukla, A., R. Fuchs, and H. Rehage, *Quasi-anomalous diffusion processes in entangled solutions of wormlike surfactant micelles.* Langmuir, 2006. **22**(7): p. 3000-3006.
18. Teixeira, A.V., E. Geissler, and P. Licinio, *Dynamic scaling of polymer gels comprising nanoparticles.* Journal of Physical Chemistry B, 2007. **111**(2): p. 340-344.
19. Savin, T. and P.S. Doyle, *Static and dynamic errors in particle tracking microrheology.* Biophysical Journal, 2005. **88**(1): p. 623-638.

20. Popescu, G., A. Dogariu, and R. Rajagopalan, *Spatially resolved microrheology using localized coherence volumes.* Physical Review E, 2002. **65**(4).
21. McKinley, G.H., et al., *Extensional flows of polymer solutions in microfluidic converging/diverging geometries.* Journal of Central South University of Technology, 2007. **14**: p. 6-9.
22. Rodd, L.E., et al., *Role of the elasticity number in the entry flow of dilute polymer solutions in micro-fabricated contraction geometries.* Journal of Non-Newtonian Fluid Mechanics, 2007. **143**(2-3): p. 170-191.
23. Pipe CJ, K.N.a.M.G. *Microfluidic Rheometry on a Chip*. in *4th AERC*. 2007. Italy.
24. Clasen, C., B.P. Gearing, and G.H. McKinley, *The flexure-based microgap rheometer (FMR).* Journal of Rheology, 2006. **50**(6): p. 883-905.
25. Clasen, C. and G.H. McKinley, *Gap-dependent microrheometry of complex liquids.* Journal of Non-Newtonian Fluid Mechanics, 2004. **124**(1-3): p. 1-10.
26. Sanehez, A.M., et al., *A piezoelectric minirheometer for measuring the viscosity of polymer microsamples.* Ieee Transactions on Industrial Electronics, 2008. **55**(1): p. 427-436.
27. Cense, A.W., et al., *Mechanical properties and failure of Streptococcus mutans biofilms, studied using a microindentation device.* Journal of Microbiological Methods, 2006. **67**(3): p. 463-472.
28. Unger, M.A., et al., *Monolithic microfabricated valves and pumps by multilayer soft lithography.* Science, 2000. **288**(5463): p. 113-116.
29. Chovan, T. and A. Guttman, *Microfabricated devices in biotechnology and biochemical processing.* Trends in Biotechnology, 2002. **20**(3): p. 116-122.
30. Towler, B.W., et al., *Viscoelastic properties of a mixed culture biofilm from rheometer creep analysis.* Biofouling, 2003. **19**(5): p. 279-285.
31. Studer, V., et al., *Scaling properties of a low-actuation pressure microfluidic valve.* Journal of Applied Physics, 2004. **95**(1): p. 393-398.
32. Duffy, D.C., et al., *Rapid prototyping of microfluidic systems in poly(dimethylsiloxane).* Analytical Chemistry, 1998. **70**(23): p. 4974-4984.
33. Favre-Bonte, S., B. Joly, and C. Forestier, *Consequences of reduction of Klebsiella pneumoniae capsule expression on interactions of this bacterium with epithelial cells.* Infection and Immunity, 1999. **67**(2): p. 554-561.
34. Tojo, M., et al., *Isolation and Characterization of a Capsular Polysaccharide Adhesin from Staphylococcus-Epidermidis.* Journal of Infectious Diseases, 1988. **157**(4): p. 713-722.
35. Rupp, C.J., C.A. Fux, and P. Stoodley, *Viscoelasticity of Staphylococcus aureus biofilms in response to fluid shear allows resistance to detachment and facilitates rolling migration.* Applied and Environmental Microbiology, 2005. **71**(4): p. 2175-2178.
36. deBeer, D. and P. Stoodley, *Relation between the structure of an aerobic biofilm and transport phenomena?* Water Science and Technology, 1995. **32**(8): p. 11-18.
37. John D. Enderle, S.M.B.a.J.D.B., *Introduction to Biomedical Engineering*. 2000, San Diego: Academic Press. 1062.
38. Shaw, T., et al., *Commonality of elastic relaxation times in biofilms.* Physical Review Letters, 2004. **93**(9).

39. Stoodley, P., et al., *Biofilm material properties as related to shear-induced deformation and detachment phenomena.* Journal of Industrial Microbiology & Biotechnology, 2002. **29**(6): p. 361-367.
40. Debeer, D., P. Stoodley, and Z. Lewandowski, *Liquid Flow in Heterogeneous Biofilms.* Biotechnology and Bioengineering, 1994. **44**(5): p. 636-641.
41. Stoodley, P., et al., *Relationship between mass transfer coefficient and liquid flow velocity in heterogenous biofilms using microelectrodes and confocal microscopy.* Biotechnology and Bioengineering, 1997. **56**(6): p. 681-688.
42. Enderle, J.D., Susan M. Blanchard and Joseph D. Bronzino, *Introduction to Biomedical Engineering*. 2000, San Diego: Academic Press. 1062.
43. Hall-Stoodley, L., J.W. Costerton, and P. Stoodley, *Bacterial biofilms: From the natural environment to infectious diseases.* Nature Reviews Microbiology, 2004. **2**(2): p. 95-108.
44. Caggioni, M., et al., *Rheology and microrheology of a microstructured fluid: The gellan gum case.* Journal of Rheology, 2007. **51**(5): p. 851-865.
45. Yamamoto, T., T. Nojima, and T. Fujii, *PDMS-glass hybrid microreactor array with embedded temperature control device. Application to cell-free protein synthesis.* Lab on a Chip, 2002. **2**(4): p. 197-202.
46. [cited 2008 June 23]; Available from: http://www.femlab.de/products/sme/.
47. Krysl, P., T.W. Cranford, and J.A. Hildebrand, *Lagrangian finite element treatment of transient vibration/acoustics of biosolids immersed in fluids.* International Journal for Numerical Methods in Engineering, 2008. **74**(5): p. 754-775.
48. Muliana, A.H. and R. Haj-Ali, *A multi-scale framework for layered composites with thermo-rheologically complex behaviors.* International Journal of Solids and Structures, 2008. **45**(10): p. 2937-2963.
49. Wang, E., C.M. Babbey, and K.W. Dunn, *Performance comparison between the high-speed Yokogawa spinning disc confocal system and single-point scanning confocal systems.* Journal of Microscopy-Oxford, 2005. **218**: p. 148-159.
50. Kohl, M.J., et al., *A microfluidic experimental platform with internal pressure measurements.* Sensors and Actuators a-Physical, 2005. **118**(2): p. 212-221.

Chapter 4

Image processing techniques to determine assembly structure of rod-shaped bacteria in aggregates and biofilms

Chapter Summary

In this chapter we report a method of quantifying structural measures of bacterial aggregates from confocal laser scanning microscopy images. Many species of bacteria exist in microcolonies consisting of aggregates of individual organisms held together by a polysaccharide matrix. Such bacteria display a range of shapes. For example, spherical (such as *Staphylococcus epidermidis* and *Staphylococcus aureus*) and rod-like shapes (i.e. *Escherichia coli* and *Klebsiella pneumoniae*) are common. To date, cytometric studies have been used extensively to determine the size and structure of the aggregates. Using confocal laser scanning microscopy and an image processing algorithm originally developed for colloidal particles, we show a method to quantify the structure and dynamics of bacterial aggregates comprised of rod-shaped organisms. We use the method to determine the positions or rod-shaped bacteria within 3D aggregates of wild type and capsular mutant *K. pneumoniae*. Interestingly, despite the mutant's inability to produce capsule, the intercentroid distance of particles within aggregates is indistinguishable from those of the wild type. Finally we use image processing to compare the intercentroid distance of bacteria within the planktonic aggregates to that of

a biofilm. We show a decrease in interorganism spacing from ~ 2 μm for the aggregates to ~1.2 μm for the bacteria within the biofilm. The method introduced here addresses a need to quantify the microstructure of rod-shaped bacterial aggregates from confocal microscopic images in a range of problems important to the life sciences and human health.

4.1 Introduction

To survive the many environments they inhabit, bacteria can grow in colonies in which individual organisms are held together by a polysaccharide matrix. These colonies are thought to grow in two different manners: single planktonic cells (1) attach to substrates and form biofilms [1-3] or (2) flocculate in flowing systems such as the bloodstream [4, 5]. In host-pathogen interactions clearance of these aggregates is important to prevent distant site infections [6]. Providing a detailed description of the morphology and microstructure of these aggregates will lead to a better understanding of their fate in the bloodstream.

Interestingly many behaviors associated with bacterial aggregates are found in colloidal systems. For example, interparticle interactions regulate aggregation in both bacterial colonies and colloidal gels and crystals [5, 7, 8]. In addition, mechanical rheometry has been a common tool to study the viscoelasticity of both colloidal gels [9, 10] and biofilms [11-13]. Similarly, colloidal scientists have applied confocal microscopy (a tool well known in life-sciences [14]) to conduct fundamental studies of colloidal suspensions [15]. Here we take advantage of these commonalities to apply image processing techniques first used to quantify local structure and dynamics in colloidal systems to better understand the microstructure of bacterial aggregates.

To determine particle locations within colloidal suspensions, an image processing algorithm developed by Crocker and Grier [16] is used to quantify data from confocal images. Local fluorescent intensity maxima are used to identify particle centroids. This same algorithm can be applied to aggregates of spherical bacteria. As an illustration of the potential application of quantitative image processing to studies of bacterial aggregates, consider Fig. 4.1. Fig. 4.1a displays a representative 2D image of a fluorescently labeled *Staphylococcus epidermidis* aggregate extracted from a time series of 300 images (Δt = 0.848 s) acquired by confocal microscopy (Leica SP-2, Leica Microsystems, Exton, PA). Applying an image processing algorithm originally used to

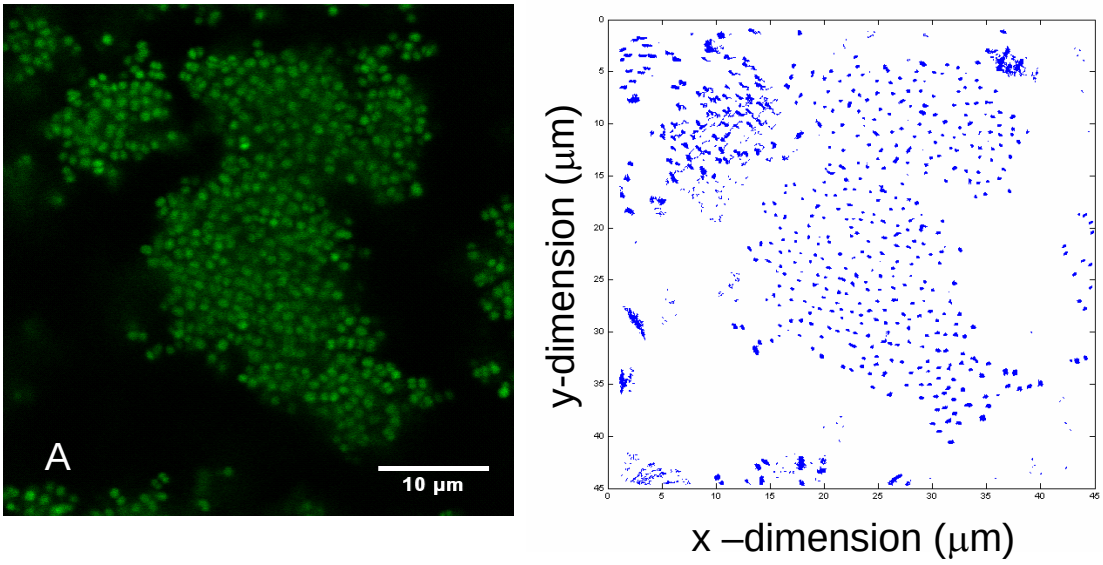

Figure 4.1: Results of quantitative image processing of individual *Staphylococcus epidermidis* (stained with Syto-9 dye) within a floc taken from confocal time series images (a) to determine the dynamics within the system (b). The arrows trace out the path of individual bacteria within the floc over 4 minutes.

quantify the dynamic behavior of colloidal gels and glasses [7, 17], we plot the trajectories of individual bacterium within the aggregate (Fig 4.1b). These data show regions with slow dynamics at the center of the aggregate and fast trajectories along its

edges. Image processing techniques for structural and dynamical properties of spherical colloidal systems are well described in the colloidal science literature [16]. Image processing methods are key tools for microrheological characterization of viscoelastic material properties [18, 19] and structural characterization of colloidal crystals [20, 21] . Here we propose that a similar process may be used to determine the 3D centroid location and orientation angles of individual non-spherical (rod-like) bacteria within aggregates and biofilms.

In this chapter, image processing techniques developed to study colloidal rod assembly [22] and diffusion [23] have been adapted to determine the centroid and orientation angle of *K. pneumoniae* in aggregates. We describe the method, including recommendations for parameters optimal for the determination of centroid location and orientation angles of each bacterium within the aggregate. As an application of the method, we then plot quantitative results from a study conducted to determine the effect of genotype, growth media and shear rate during flocculation on aggregate structure. Finally we present the quantitative difference in interparticle location between planktonically grown aggregates and biofilm of the same bacteria.

4.2 Materials and methods

4.2.1 Bacteria preparation and growth conditions

For this study two strains of *K. pneumoniae* were used: biofilm forming encapsulated LM21 wild type and its capsular mutant LM21-Δ*cps* [24, 25]. The capsular mutant has been shown to produce more protein adhesin than the encapsulated wild type [24]. Both were crypreserved at -80ºC in Lenard Bertani (LB) broth prior to next-day loop innoculation of Hanks balanced salt solution (HBSS) modified with 0.004% (w/w)

and 0.4% (w/w) glutamine. Solutions of aggregates were made in 250 mL Erlenmeyer flasks shaking at 50 and 200 rpm at 37ºC using a shaker/incubator with a 1 cm radius orbit (model 435, Thermo-Forma, Marlette, OH). Biofilm was grown in the microfluidic device described in Chapter 3. The device was inoculated with wild type aggregates grown similar to the method described above. After incubation a syringe pump (Harvard apparatus, Holliston, MA) was used to flow LB broth through the microfluidic device (minimum cross-section of 125 μm x 25 μm) at 0.1 mL/hour for ~ 20 hours at 37ºC. For imaging, the bacteria were stained with SYTO 9 dye (Invitrogen, Carlsbad, CA). For suspensions of bacterial aggregates, 1 μL of dye was added to 10 mL of the aggregate suspension ~10 minutes prior to imaging. For the biofilm, 1 μL of dye was added to the inlet. The dye flowed through the channels using a syringe with LB broth by hand. SYTO 9 is a nucleic acid stain, therefore in bacteria, the entire cytoplasm will fluoresce. This fluorescence is similar to the core of fluorescently labeled colloidal particles used in previous image processing studies.

4.2.2 Confocal microscopy

Images were acquired using a 100x N.A. = 1.4 oil immersion objective on a confocal laser scanning microscope (CLSM, Leica TCS SP-2 with a DMIRE-2 inverted microscope). Fluorescent dye excitation was by a 488 nm argon ion laser. Detection was by a photo multiplier tube over the range 500-650 nm. 3D image volumes were acquired from a series of 2D scans. The typical pixel size of the 512 x 512 images was 81 nm yielding a 2D scan size of 41.7 x 41.7 μm^2. To ensure cubic 3D voxels, scan step sizes were 81 nm as well. The total volume depth was dependent upon the size of the aggregate. The typical time to acquire a volume was ~2 minutes.

To image the aggregates 500 μL samples of fluorescently labeled bacteria in solution were pippetted into imaging sample vials. These vials were 4 mm inner diameter glass capillaries adhered with ultra-violet light cured adhesive (Dymax Light Weld, Torrington, CT) to coated No. 1 (thickness 0.14 - 0.17 mm) coverslips (Fisher Scientific, Pittsburgh, PA). To enhance adhesion of the aggregates to the bottom substrate for imaging, a thin layer (~ 20 μm) of poly(dimethyl siloxane) (PDMS, Dow Sylgard 184 Silicone Elastomer Kit) was spin coated at 2400 rpm for 30 s onto the glass coverslip prior to bonding the glass capillary. This layer of PDMS increased the adhesion of the aggregates to the bottom substrate to allow for imaging of nearly static aggregates.

4.2.3 Identification of bacteria centroid location and orientation angle using image processing

The image processing method used was originally developed to exploit the idea that the centroid of a colloidal particle can be identified by analyzing the relative brightness of voxels in the local region surrounding the particle. Our aim here is to evaluate the scope to apply this general idea to fluorescently stained bacteria in aggregates. Initial observations (cf. Fig. 4.2a) of bacteria imaged at high resolution show that the fluorescence intensity distribution within bacterial aggregates is not too different from that of colloidal particles. This congruence supports application of colloidal science image processing methods to bacterial aggregates.

Identification of these maxima from microscopic images was first accomplished for spherical colloids [16]. The algorithm used here to identify bacterium centroids is an extension of this method [22]. Briefly, the algorithm interrogates the entire 3D image

volume to identify the voxels in the image that are fluorescent maxima along the local lines that are best estimates of the central backbones of the bacteria. A cluster analysis routine is applied to group these backbone voxels into a cluster for each rod. The constraints in the cluster analysis routine are that voxels grouped together satisfy a minimum distance and mutual orientation criteria. The centroid of each bacterium is calculated by determine the 3D midpoint of the backbone through second moment averaging of the backbone clusters. Backbone lengths are calculated and then used to determine the orientation angle of each bacterium in the image volume. A detailed explanation of the method may be found in Mohraz and Solomon [22]. Here we provide details necessary to discuss results from image processing and its extension quantitatively characterize the structure of aggregated *K. pneumoniae*.

An initial filtering step is typical of image processing. In our case, to lessen the effect of noise on the intensity signal, voxels are convoluted with their nearest neighbors within a local distance, w, by applying a Gaussian filter to the 3D image volume. The value of w is based on the half-width of the bacteria in the image (here, w = 5 typically). The filtered images are then scanned to search for voxels that are the brightest within some local region. These local intensity maxima are then voxels that are candidates for inclusion in the bacterium's backbone. The exact criterion used to identify a candidate voxel is the following: a candidate voxel is a voxel that is the brightest point along at least a certain percentage of all the line segments radiating outward from it. To apply this criterion, local lines centered on the test voxel of length 2w + 1 are constructed in all orientations such that voxels along lines within a sphere (D = 2w + 1) are interrogated. A candidate point is identified as a backbone voxel if it is the brightest along at least a crical

fraction of these line segments. The critical fraction is a parameter to be optimized, and is typically set at about 80%. Backbone voxels also satisfy a minimum intensity threshold, typically set to 12% of the maximum image intensity.

Several criteria are used to group candidate points into bacterium backbones. First, backbone voxels separated by no more than one pixel are grouped. Second, small clusters separated by a minimum distance (typically 3 voxels) and both oriented in the same direction (typically within 0.05 radians) are then grouped together because they are

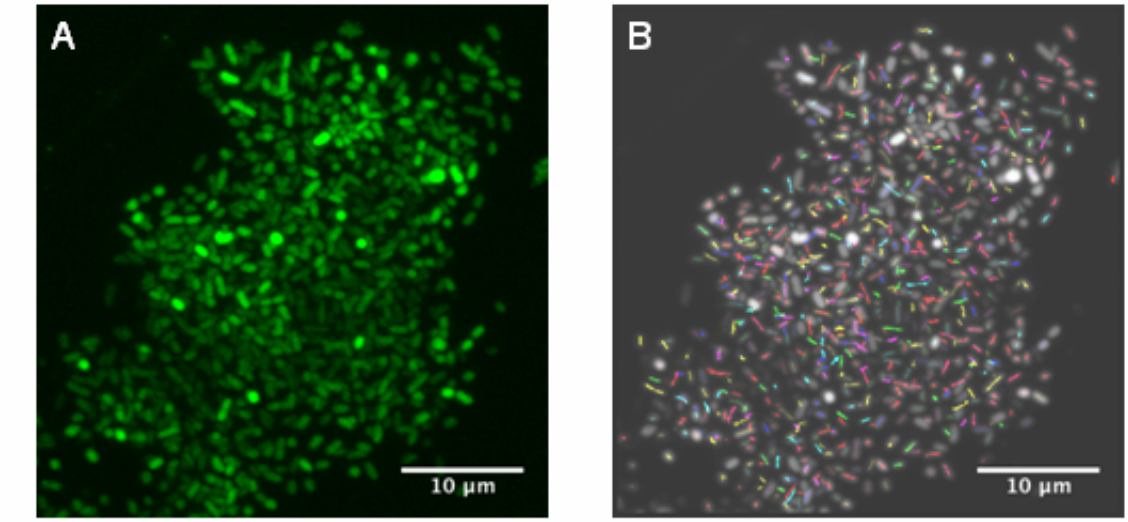

Figure 4.2: Image processing of individual capsular mutant *Klebsiella pneumoniae* within a floc. Fig 4.2A shows the z-projection of the image volume (41.7 x 41.7 x 23.3 μm^3). Fig 4.2B shows the same projection with individual bacteria backbones identified.

most often part of the same bacterium. The known physical length of the bacteria is then used to reanalyze backbones that are anomalously long (i.e. daughter bacteria incorporated as one). These split backbones are reclustered as individual bacterium. Fig 4.2a shows a 2D projection of a 3D fluorescently labeled capsular mutant *K. pneumoniae* aggregate. Fig 4.2b is a corresponding projection of the convoluted image reconstruction with individual backbones identified as per the method just described. Once the

backbones are identified bacterium centroids and orientation angles are calculated using the method we now describe.

The following calculations are performed to identify bacterium centroids and orientation angles based upon the voxels in the backbone. First the centroid is calculated as the 3D midpoint of the backbone. This calculation is performed by summing all the coordinates of the voxels in the backbone in each direction (x, y, z) individually and normalizing by the total number of voxels in the backbone. The orientation angle is determined by first calculating the average mean-squared lengths of the backbone in each dimension (l_x, l_y, l_z). From these numbers an average length can be calculated, l. The orientation angles are then simple trigonometric functions of these lengths. Fig 4.3a gives a schematic definition of the polar and azimuthal orientation angles, θ and ϕ, respectively, with the centroid located at the origin. Fig. 4.3b shows a close-up reconstructed image with bacterial backbones labeled. At this high resolution the intensity gradients orthogonal to the bacterium backbone which the code is designed to detect are apparent. To illustrate the algorithm's functionality we label one bacterium's centroid and azimuthal angle, ϕ. We then plot the 3D backbones of each bacterium within this volume from the centroid and orientation angles alone (Fig. 4.3c). By rotating this 3D representation to visualize the same plane as the reconstructed image in Fig 4.3b, four labeled bacteria agree well with the backbones determined by image processing (Fig. 4.3d). Because the bacteria are axially symmetric (that is we cannot distinguish between the two tips of the bacterial rods), their orientation angles is specified on the half space ($0 \leq \theta \leq \pi$, $0 \leq \phi \leq \pi$).

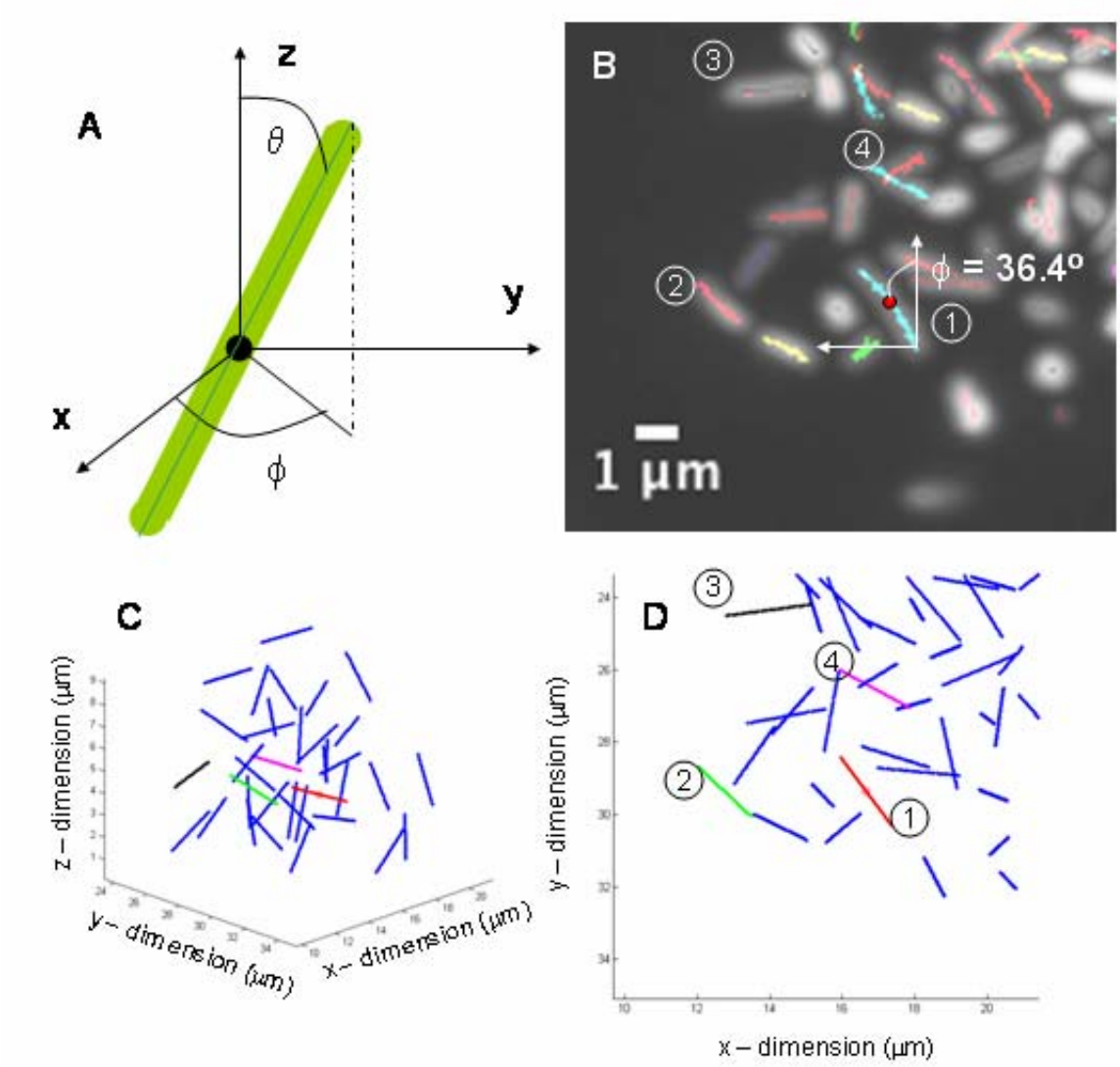

Figure 4.3: Schematic diagram of bacteria orientation angles θ and ϕ, with bacteria centroid at origin (a). Close-up of bacteria with backbones identified (b). Here we give one bacterium's centroid and azimuthal angle and label three others to show there placement in the plotted reconstruction from centroid and orientation angles (c,d).

4.3 Quantification of microscale structure of bacterial aggregates and biofilms

We first apply the image processing method to determine the microstructure of aggregates of wild type and capsular mutant *K. pneumoniae*. The three dimensional design space for experiments is a 2 x 2 x 2 matrix of genotype, glutamine concentration in HBSS and shear rate during growth of the bacterial aggregates. These variables affect

adhesion properties (genotype), growth environment in available nitrogen (glutamine concentration) and break-up forces from shear during growth. Image volumes of aggregates comprised of wild type and capsular mutant bacteria were acquired after growing in HBSS modified with 0.4% and 0.004% (w/w) glutamine concentrations at two different shaker/incubator spin speeds, 50 and 200 rpm. Under each condition confocal image volumes of several aggregates were acquired. For these growth conditions wild type flocs ranged in number from 53 - 659 bacteria. Capsular mutant number similarly ranged from 21 - 857 bacteria. Interestingly, it has been reported that these conditions lead to similar morphologies of the flocculated bacteria especially when comparing size of aggregates for the two genotypes [25]. While confocal microscopy has been used to quantify the size of aggregates and biofilms [26, 27], we apply image processing to determine microstructural differences within the aggregates. These microstructural differences are difficult to extract without high resolution microscopy.

Included in Fig 4.4 are two typical aggregates of bacteria grown in HBSS modified with 0.004% glutamine at 200 rpm. Here we show the reconstructed 2D projection of the 3D volumes with bacteria backbones identified. In these particular samples the capsular mutant aggregate (Fig 4.4a) is larger (~860 bacteria) compared to the wild type (Fig 4.4b) (~300 bacteria). A particle counter is likely a better tool for this type of data. Visual inspection of the bacteria within the aggregates appear to be randomly oriented with little difference between the capsular mutant (Fig 4.4a) and the wild type (Fig 4.4b). To verify the random orientation of the bacteria we present a 3D reconstruction of the identified backbones using their centroid and orientation angle (c, d). These reconstructions show tightly packed bacteria within the centers of the

aggregates. The wild type image volume does include some bacteria separate from the main central aggregate. These bacteria are also well identified by the method.

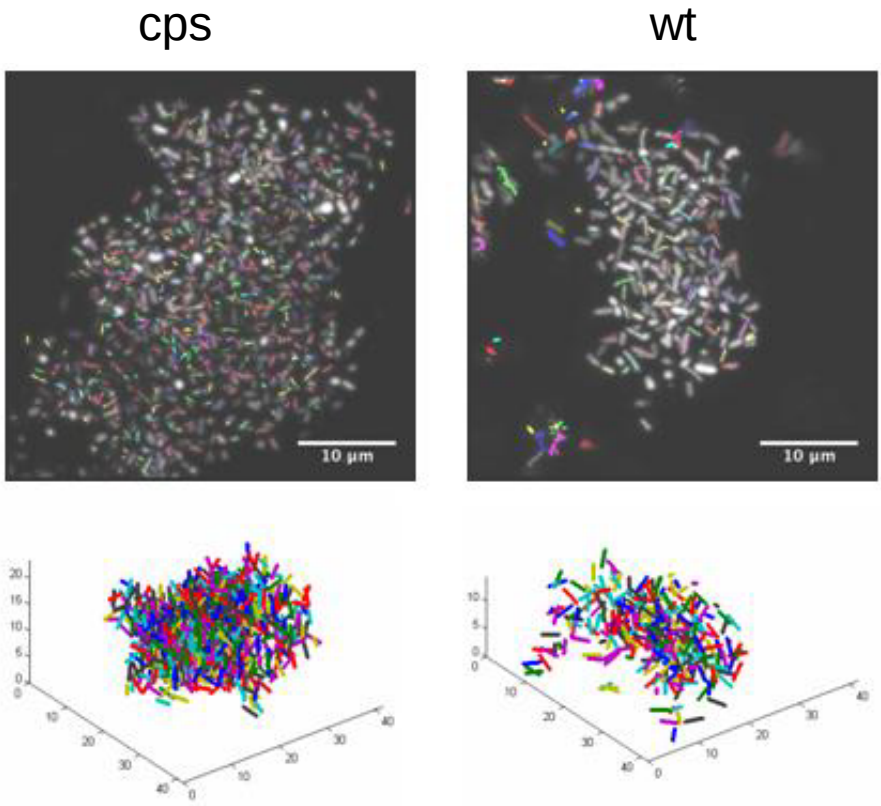

Figure 4.4: This figure shows image reconstructions of 3D volumes of bacteria identified in capsular mutant (A) and wild type (B) aggregates grown in HBSS modified with 0.004% glutamine at 200 rpm. Fig 4.4 C and D show representations of the identified backbones using the centroid and orientation angles calculated from image processing.

Fig. 4.5 shows the effect of glutamine concentration on the size of aggregates of capsular mutant *K. pneumoniae*. Fig 4.5a and b show bacteria backbones identified in aggregates of capsular mutant grown at 50 rpm in HBSS modified with 0.004% and 0.4% glutamine respectively. Again the obvious difference between these two aggregates can be detected using particle counters with statistical advantages. The capsular mutant aggregate grown in HBSS modified with 0.004% glutamine is comprised of 358 bacteria

while that grown in HBSS modified with 0.4% glutamine has 51 identified bacteria. Again both aggregates appear to consist of randomly oriented bacteria. This result is confirmed with the graphical representation of the aggregates using the centroid and orientation angles calculated from image processing.

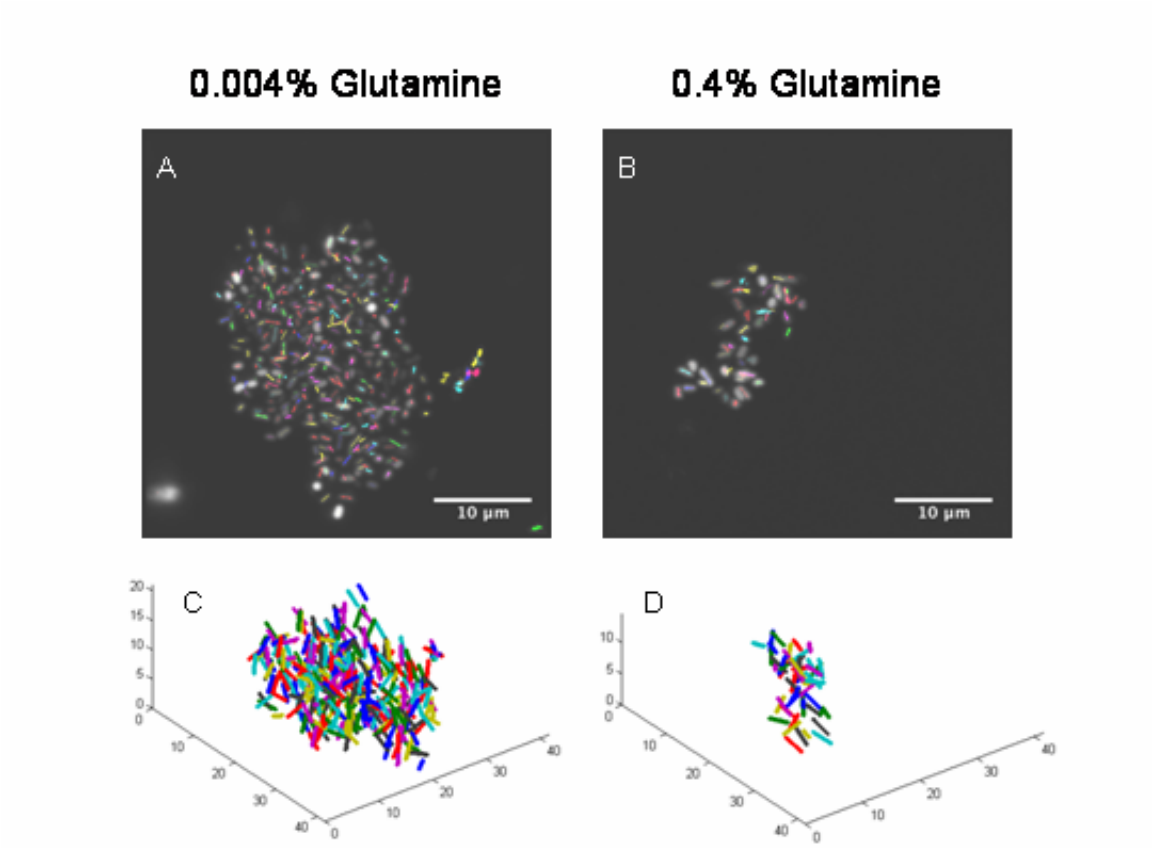

Figure 4.5: Here we show the effect of glutamine concentration on capsular mutant aggregates. We show the backbones of individual bacteria identified in the 2D reconstructed image of the 3D volume for aggregates grown in HBSS modified with 0.004% (A) and 0.4% (B) glutamine. To show the random orientation of the bacteria, the graphical representations of the backbones is shown (C, D).

Error estimation depends upon visual verification of the number of rods identified by the method. Bacteria within four aggregates consisting of 51 particles or fewer were counted visually and compared to the number of bacteria identified by image processing. An average error in the four measurements was ~ 7%. The largest error in particle

identification came from two sources of motion: aggregate rotation (limited but not eradicated by the PDMS coating on the substrate) and small detached aggregates moving through the volume during the scan.

Once backbones are identified, the centroid and orientation angles are used to characterize the microstructure of the aggregates. Note that the number density (or volume fraction) of bacteria in the aggregate is not as useful as other potential structural measures because the volume of the aggregate is a poorly defined quantity. One such suitable measure of aggregate density is the nearest neighbor inter-centroid distance. That is, we compute the separation between centroids of any two rods that are nearest neighbors. A nearest neighbor is calculated by first determining the distance between all bacteria. The nearest neighbor is identified as being the bacterium with the closest distance. Fig. 4.6a plots the probability distribution of this inter-centroid distance of the two genotypes at the two different shaker rotational speeds for aggregates grown in HBSS modified with 0.004% glutamine. The statistics of these distributions were constructed from the coordinates of 640 bacteria from three different aggregates. The distributions show little difference in the distance for either the genotype or the shaker speed. In particular, the average nearest neighbor centroid distance is ~2 μm for all four conditions. This null result for the case of the two different genotypes is of most interest: despite the lack of capsule, the distance between bacteria in the capsular mutant and the wild type aggregates of *K. pneumoniae* are indistinguishable. Capsule on *K. pneumoniae* inhibits the production of protein adhesin when compared to the capsule degenerate genotype [24]. This variability in adhesin production would predict that different

exopolysaccharide structures are created by the two different bacteria. Our results show that this difference does not affect their inter-particle spacing in aggregates.

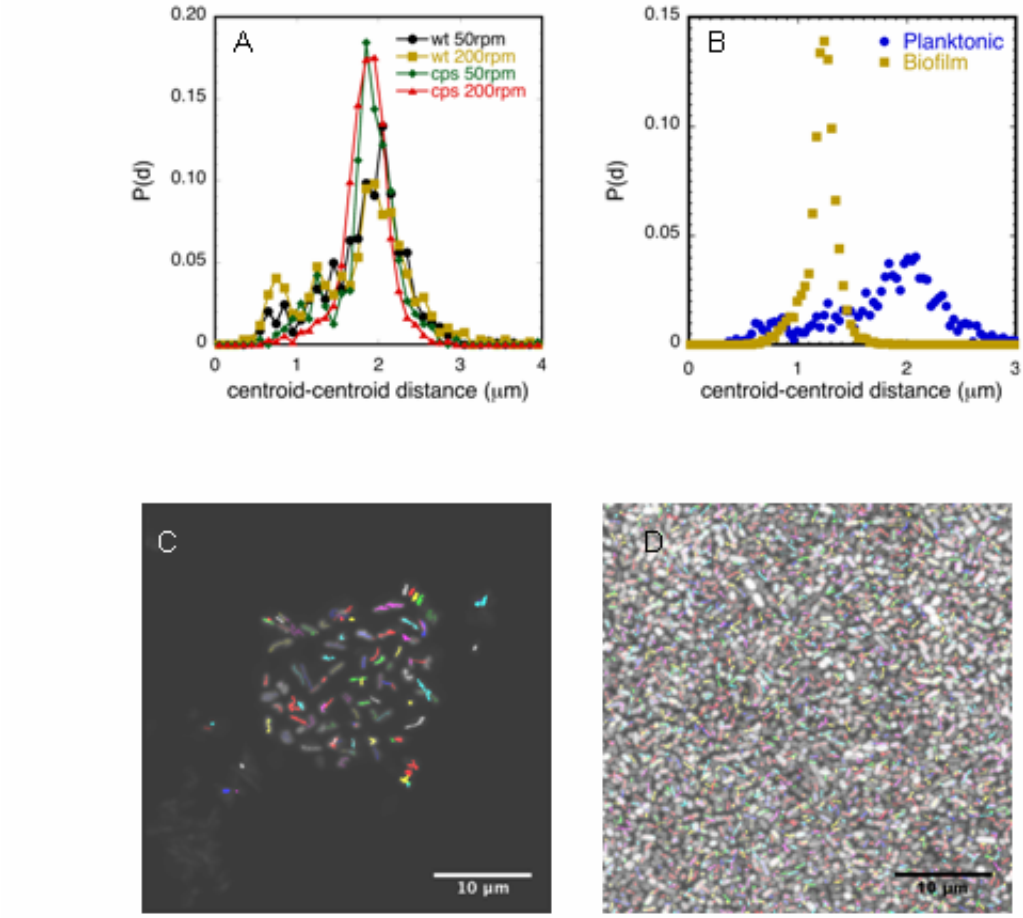

Figure 4.6: Probability distributions of wild type and capsular mutant *K. pneumoniae* grown at different shear rates are plotted. We show little difference in the distance separating the two genotypes (a). If we compare the wild type aggregation in planktonic form (c) to those grown in a biofilm (d) we show close packing of the organisms in the biofilm (b).

Fig 4.6b plots the probability distributions for the planktonic wild type aggregates at both speeds compared to the nearest neighbor distance distribution of 1000 wild type K. pneumoniae in a biofilm. The biofilm was formed by seeding a microfluidic channel

with loop-inoculated LB broth and flowing LB broth at 0.1 mL/hour for ~20 hours. The probability distribution narrows and shifts to a closer nearest neighbor inter-centroid location (~ 1.2 μm). This density difference is qualitatively apparent in the 2D projections of a typical aggregate (c) and the biofilm (d) with backbones identified and labeled in each. While this result is not surprising given biofilms are typically close packed, the resulting plot displays the application of image processing to microscale characterization of rod-shaped bacteria in aggregates and biofilms. With image processing we quantify a physical difference in structure (namely, inter-centroid distance). High resolution imaging allows for confocal applications to extend beyond qualitative comparisons and macroscopic quantitative measures (i.e. biofilm thickness). Given the typical heterogeneity found in biofilms [28], image processing techniques like those shown here can quantify structural measures such as void space and porosity in biofilms. Because of the time dependent nature of biofilm formation, these methods can be used to better understand time-dependent structural phase-space of growing biofilms. Applying image processing to these systems allows us to characterize previously inaccessible microscale structural measurements of rod-shaped bacterial aggregates and biofilms.

4.4 Conclusions

We apply image processing to determine the microstructure of aggregates and biofilms formed from rod-shaped *K. pneumoniae*. We use image processing data to show that the capsular mutant does not have a distinguishable difference in inter-centroid location that of the wild type bacteria. This same analysis is used to show that dense biofilms grown from wild type *K. pneumoniae* shift the inter-centroid distance from 2 μm

for aggregates to 1.2 μm for bacteria within the biofilm. Similar types of analyses have already been used in life sciences to track adenovirus motion [29] and cellular organelles [30]. We show that image processing of high resolution confocal images can be used to accomplish more than qualitative comparisons and macroscopic measures of bacterial systems.

References

1. Johnson, L.R., *Microcolony and biofilm formation as a survival strategy for bacteria.* Journal of Theoretical Biology, 2008. **251**(1): p. 24-34.
2. Watnick, P. and R. Kolter, *Biofilm, city of microbes.* Journal of Bacteriology, 2000. **182**(10): p. 2675-2679.
3. Costerton, J.W., P.S. Stewart, and E.P. Greenberg, *Bacterial biofilms: A common cause of persistent infections.* Science, 1999. **284**(5418): p. 1318-1322.
4. Bortz, D.M., et al., *Klebsiella pneumoniae flocculation dynamics.* Bulletin of Mathematical Biology, 2008. **70**(3): p. 745-768.
5. Bos, R., H.C. van der Mei, and H.J. Busscher, *Physico-chemistry of initial microbial adhesive interactions - its mechanisms and methods for study.* Fems Microbiology Reviews, 1999. **23**(2): p. 179-230.
6. Lockhart, P.B., et al., *Impact of amoxicillin prophylaxis on the incidence, nature, and duration of bacteremia in children after intubation and dental procedures.* Circulation, 2004. **109**(23): p. 2878-2884.
7. Dibble, C.J., M. Kogan, and M.J. Solomon, *Structure and dynamics of colloidal depletion gels: coincidence of transitions and heterogeneity.* Phys Rev E Stat Nonlin Soft Matter Phys, 2006. **74**(4 Pt 1): p. 041403.
8. Leunissen, M.E., et al., *Ionic colloidal crystals of oppositely charged particles.* Nature, 2005. **437**(7056): p. 235-240.
9. Yin, G.J. and M.J. Solomon, *Soft glassy rheology model applied to stress relaxation of a thermoreversible colloidal gel.* Journal of Rheology, 2008. **52**(3): p. 785-800.
10. Gopalakrishnan, V. and C.F. Zukoski, *Delayed flow in thermo-reversible colloidal gels.* Journal of Rheology, 2007. **51**(4): p. 623-644.
11. Rupp, C.J., C.A. Fux, and P. Stoodley, *Viscoelasticity of Staphylococcus aureus biofilms in response to fluid shear allows resistance to detachment and facilitates rolling migration.* Applied and Environmental Microbiology, 2005. **71**(4): p. 2175-2178.
12. Stoodley, P., et al., *Biofilm material properties as related to shear-induced deformation and detachment phenomena.* Journal of Industrial Microbiology & Biotechnology, 2002. **29**(6): p. 361-367.
13. Towler, B.W., et al., *Viscoelastic properties of a mixed culture biofilm from rheometer creep analysis.* Biofouling, 2003. **19**(5): p. 279-285.
14. Pawley, J.B.e., *Handbook of biological confocal microscopy*. 2nd ed. 1995, New York: Plenum Press.
15. Prasad, V., D. Semwogerere, and E.R. Weeks, *Confocal microscopy of colloids.* Journal of Physics-Condensed Matter, 2007. **19**(11).
16. Crocker, J.C. and D.G. Grier, *Methods of digital video microscopy for colloidal studies.* Journal of Colloid and Interface Science, 1996. **179**(1): p. 298-310.
17. Weeks, E.R., et al., *Three-dimensional direct imaging of structural relaxation near the colloidal glass transition.* Science, 2000. **287**(5453): p. 627-631.
18. Solomon, M.J. and Q. Lu, *Rheology and dynamics of particles in viscoelastic media.* Current Opinion in Colloid & Interface Science, 2001. **6**(5-6): p. 430-437.

19. Savin, T. and P.S. Doyle, *Statistical and sampling issues when using multiple particle tracking.* Physical Review E, 2007. **76**(2).
20. Tata, B.V.R. and B. Raj, *Confocal laser scanning microscopy: Applications in material science and technology.* Bulletin of Materials Science, 1998. **21**(4): p. 263-278.
21. Solomon, T. and M.J. Solomon, *Stacking fault structure in shear-induced colloidal crystallization.* Journal of Chemical Physics, 2006. **124**(13).
22. Mohraz, A. and M.J. Solomon, *Direct visualization of colloidal rod assembly by confocal microscopy.* Langmuir, 2005. **21**: p. 5298-5306.
23. Mukhija, D. and M.J. Solomon, *Translational and rotational dynamics of colloidal rods by direct visualization with confocal microscopy.* Journal of Colloid and Interface Science, 2007. **314**(1): p. 98-106.
24. Favre-Bonte, S., B. Joly, and C. Forestier, *Consequences of reduction of Klebsiella pneumoniae capsule expression on interactions of this bacterium with epithelial cells.* Infection and Immunity, 1999. **67**(2): p. 554-561.
25. Thornton, M., et al., *Aggregate growth of Klebsiella Pneumoniae in Serum. in preparation*, 2008.
26. Allegrucci, M. and K. Sauer, *Characterization of colony morphology variants isolated from Streptococcus pneumoniae biofilms.* Journal of Bacteriology, 2007. **189**(5): p. 2030-2038.
27. Monier, J.M. and S.E. Lindow, *Frequency, size, and localization of bacterial aggregates on bean leaf surfaces.* Applied and Environmental Microbiology, 2004. **70**(1): p. 346-355.
28. Stewart, P.S. and M.J. Franklin, *Physiological heterogeneity in biofilms.* Nature Reviews Microbiology, 2008. **6**(3): p. 199-210.
29. Helmuth, J.A., et al., *A novel supervised trajectory segmentation algorithm identifies distinct types of human adenovirus motion in host cells.* Journal of Structural Biology, 2007. **159**(3): p. 347-358.
30. Kalaidzidis, Y., *Intracellular objects tracking.* European Journal of Cell Biology, 2007. **86**(9): p. 569-578.

Chapter 5

Evidence of Strain Hardening in Bacterial Biofilms

Chapter Summary

In this chapter we apply characterization tools developed in the previous chapters to investigate the unusual, non-linear mechanical response of bacterial biofilms. As shown in Chapter 3 biofilms comprised of both *Staphylococcus epidermidis* and *Klebsiella pneumoniae* when compressed in a flexible microfluidic rheometer wxhibit an increase in static elastic (Young's) modulus upon the application of increasing strain. Here we report additional experiments and data analysis that reveal a similar behavior in planktonically grown *S. epidermidis* aggregates that are mechanically weak. We then analyze these data as well as the stress-strain measurements of biofilms in the flexible microfluidic rheometer. We find, for the strains interrogated, that the biofilms show an increase in Young's modulus with strain after an initial linear regime. Interestingly, this strain hardening is not a consequence of increased packing of the bacteria, because it occurs without a distinguishable increase in volume fraction. Finally, we use particle tracking analysis to show the streamlines of individual bacterium as the biofilm is compressed. This analysis confirms the steady volume fraction of the bacteria in the biofilm upon compression.

5.1 Introduction

Characterization of the viscoelastic properties of biofilms provides a fundamental understanding of their resistance to mechanical stresses. These mechanical stresses arise in natural, industrial and physiological aqueous environments [1, 2]. As reported in Chapter 3 an increase in compressive strain applied by a flexible microfluidic rheometer results in a static elastic modulus of biofilms. Such strain hardening may have important implications for the clearance and fracture of biofilms, because biofilms inhabit many environments with varied characteristic lengths. For example a once-sessile aggregate sloughed off from a biofilm due to a yielding transition could be transported through capillaries as small as ~10 μm while flowing through the bloodstream [3]. Such an aggregate's ability to deform on these length scales in order to traverse a capillary bed might be a consequence of the effect of strain hardening. Further investigation of this phenomenon may provide insight into the underlying microstructural changes within the biofilm.

Strain hardening is a phenomenon also found in concentrated colloidal suspensions [4] fractal gels [5, 6] and polymer glasses [7]. For diffusion-limited cluster aggregated colloidal gels the low strain elastic modulus depends on the volume fraction, ϕ. The same system shows strain hardening that can be characterized over a range of volume fractions and scales as γ^2 [6]. Because biofilms consist of aggregated bacteria held together by a polymer matrix, they may behave similar to colloidal suspensions with tuned interactions. To inform our investigation of strain hardening in biofilms we review characterization studies typical of colloids.

This chapter builds upon the work associated with the previous two chapters to focus on characterizing the cause of strain hardening in biofilms. We find that strain hardening is not only found in biofilms as reported in chapter 3, but is characteristic of weakly elastic aggregates of *S. epidermidis*. We plot the stress-strain relationship taken from the flexible microfluidic rheometer for four different biofilms, all of which show strain-hardening. To analyze this effect, we report a strain dependent static elastic (Young's) modulus and find that it increases linearly with strain (in the non-linear regime). We apply image processing techniques discussed in chapter 4 to determine the volume fraction and trajectories of single bacterium in the biofilm as it is compressed.

5.2 Materials and methods

5.2.1 Flexible microfluidic rheometer characterization of biofilms

To characterize the elastic modulus of bacterial aggregates and biofilms we used the flexible microfluidic rheometer previously described in chapter 3. Briefly, the device consisted of two orthogonal (one upper and one lower) microfluidic channels fabricated in poly(dimethyl siloxane) (PDMS, Dow Sylgaurd 184 Elatomer Kit) using a rapid prototyping technique [8]. The lower fluidic channel was formed from flexible PDMS such that its top surface was deformable when air pressure was applied to the upper channel [9]. To conduct an experiment a step-wise increase in air pressure was applied to the air channel and the steady-state deformation was measured at each pressure. When the lower fluidic channel was loaded with a soft viscoelastic solid, the deformation of the PDMS membrane at each applied pressure was governed by the material properties of the viscoelastic solid. We measured this deformation with confocal laser scanning microscopy (CLSM). The experimental deformation was compared to finite element

analysis (FEA, Comsol Multiphysics v. 3.3a) of the flexible microfluidic rheometer to characterize the elastic modulus of the soft viscoelastic solid. For this study the soft viscoelastic solids tested were bacterial aggregates and biofilms. *K. pneumoniae* and *S. epidermidis* have clinical significance as nosocomial pathogens [10, 11].

Monospecies biofilms consisting of *Staphylococcus epidermidis* RP62A and *Klebsiella pneumoniae* LM21 were grown in the flexible microfluidic device according to the procedure outlined in chapter 3. The fluidic test channel of the device was seeded with loop inoculated Luria-Bertani (LB) broth that was incubated on a shaker/incubator (model 435, Thermo-Forma, Marlette, OH) at 200 rpm and 37º until mid-log phase growth. To characterize the elastic modulus of planktonically grown *S. epidermidis* aggregates, experiments were conducted using the flexible microfluidic rheometer with the seeded suspension of bacterial aggregates. To grow biofilms in the device, LB broth flowed through the rectangular microfluidic test channel (cross-section 25 μm x 125 μm) at 0.1 mL/hr. using a syringe pump (Harvard Apparatus, Holliston, MA) for a minimum of 18 hours in an incubator at 37ºC. For imaging the bacteria were labeled with fluorescent SYTO-9 dye (Invitrogen, Carlsbad, CA).

5.2.2 Confocal laser scanning microscopy and image processing

The deformation of the flexible PDMS membrane was measured at the centerline of the fluidic test channel using confocal laser scanning microscopy (Leica TCS SP-2 with a DMIRE-2 inverted microscope, Exton, PA). 2D images were acquired by scanning in a plane perpendicular to the bottom substrate. For imaging a 100x N.A. = 1.4 oil immersion objective was used. The deformation change at each applied pressure, Δh was normalized by the initial thickness of the biofilm, h_0, to define the strain, $\varepsilon = \Delta h/h_0$.

To detect the deformation of the flexible PDMS membrane incident light from an argon ion laser (λ = 488 nm) was detected with a photomultiplier tube over the range of 479-498 nm. Fluorescent images of the individual bacteria were acquired in the same plane with detection over the range of 500-650 nm. To characterize the structure of the biofilm prior to deformation, 3D fluorescent image volumes were also acquired of the bacterial biofilm loaded in the device. The initial 3D image volume of the biofilms provided a basis for characterizing the volume fraction of bacteria in the biofilm. Subsequent 2D image processing of the biofilm under compression was used to quantify changes in microscale structure and the trajectories of individual bacteria as the flexible membrane deformed the biofilm.

Image processing was applied consistent with the description in chapter 4. Image processing of spherical *S. epidermidis* was conducted per the algorithm outlined by Crocker and Grier [12] and originally developed to study colloidal suspensions [13]. Briefly the algorithm detects the location of bacteria based on the condition that the centroid exists at the local fluorescent intensity maximum. To study the motion of individual bacteria as a function of biofilm stress and deformation, the methods of chapter 4 were extended to include particle tracking. Briefly, in particle tracking centroids found in each of a series of images are linked to generate the trajectories of the individual bacteria as a function of time. For trajectory linking the frame-by-frame locations of bacteria are used. Small deformations were applied to prevent a bacterium from moving more than its radius. This is the minimum criterion required to link a cell from one frame to the next. The initial structure of the rod-shaped *K. pneumoniae* was characterized using the same algorithm applied to study the bacterial aggregates in

chapter 4. To determine the 2D location of the *K. pneumoniae* bacteria as the biofilm was compressed, however, the spherical algorithm was used. This method was used to track the rod-shaped bacteria because empirically we found that most of the bacteria were aligned perpendicular to the image plane, therefore they were resolved in cross section.

5.3 Results

In chapter 3 we found that bacterial biofilms display characteristics of strain-hardening in a compressive flexible microfluidic rheometer. As an initial analysis of this behavior, we quantified a low-strain modulus and a high-strain modulus for different *S. epidermidis* and *K. pneumoniae* biofilms by comparing the data to results of finite element analysis. Interestingly, we found that aggregates of S. epidermidis show only weak elasticity in the rheometer at low-strains. At high strains, however, quantifiable strain hardening in these systems was observed. To understand this phenomenon further, we here apply the analysis methods of chapter 3 using FEA to quantify the effect of strain on the elasticity of the biofilms. Normalized data report an exponential increase in static elastic modulus with increasing strain. Interestingly, characterizing the microscale structure of the biofilm reveals that strain hardening occurs with little or no effect on the volume fraction of bacteria in the biofilm. The steady state volume fraction was confirmed by trajectory analysis of the biofilm.

5.3.1 Strain hardening in planktonically grown *S. epidermis* aggregates

Fig. 5.1 plots the stress-strain response of planktonically grown aggregates of *S. epidermidis*. Fig 1a plots the deformation of the 40 kPa flexible PDMS membrane in contact with a *S. epidermidis* aggregate loaded into the test channel. The response of the membrane loaded with water is also plotted. The compression reveals that the two

responses are indistinguishable at low strains. Referring to Fig. 3.10 of chapter 3, we conclude that the aggregates of *S. epidermidis* must have a modulus < 1 kPa. From Fig. 3.10, this is the minimum modulus to affect a resolvable difference in deformation for a 40 kPa PDMS membrane. This low value is in contrast with the biofilms of the same species (E_0 ~ 2-3 kPa, as reported in chapter 3). Thus we conclude that the low-strain moduli of planktonic and biofilm phenotypes of *S. epidermidis* are significantly different.

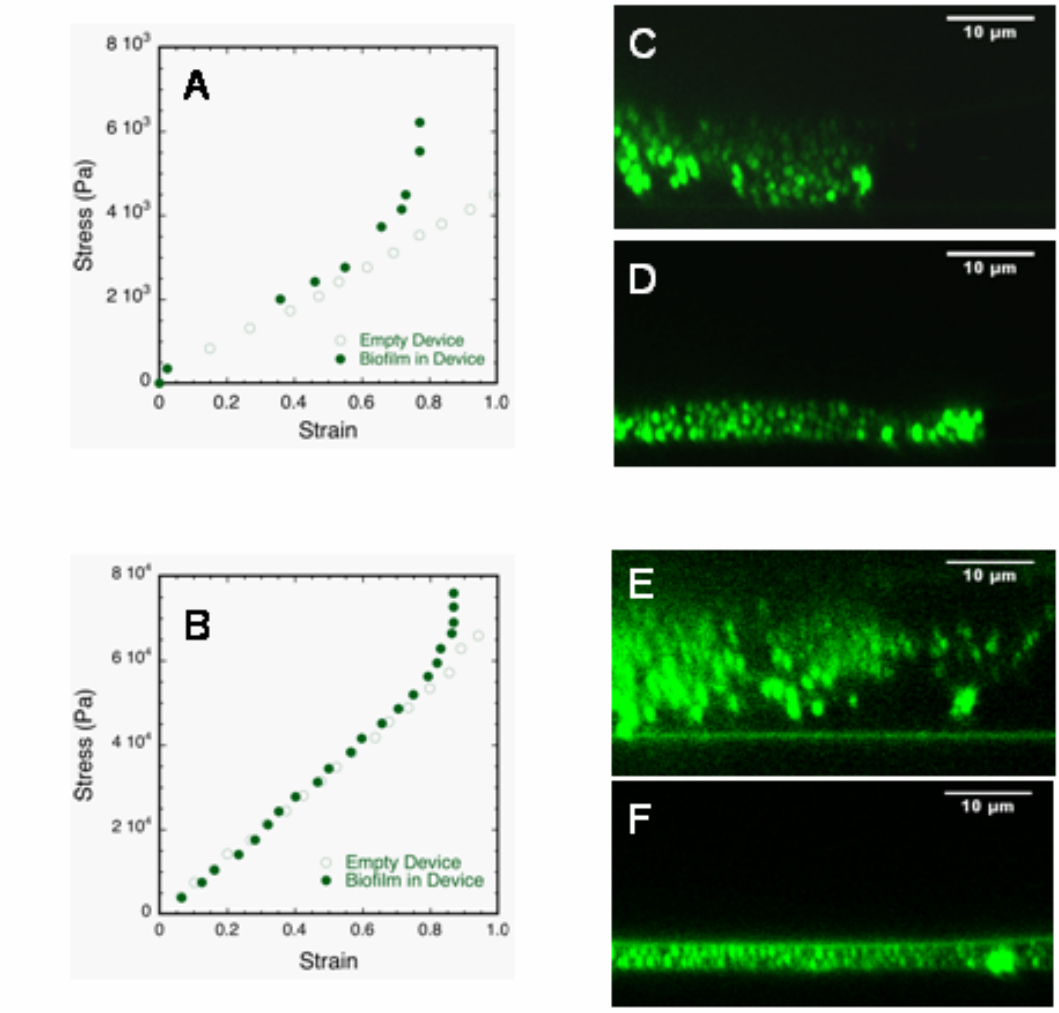

Figure 5.1: We plot the stress-strain behavior of planktonically grown weakly elastic *S. epidermidis* aggregates. Fig. 5.1 a and b show the response in a 40 kPa and 400 kPa device respectively. Fig. c, d show the undeformed and deformed morphology of the aggregate in the 40 kPa, respectively. Fig. e and f report the same for the high modulus device.

Next we consider the high strain response of planktonic *S. epidermidis*. After the planktonic aggregate has been subjected to a strain of $\varepsilon \sim 0.8$, the stress-strain response of the membrane abruptly increases. This upturn indicates a change in elastic modulus of the aggregate. Fig 5.1c and d show fluorescent images in the plane normal to the bottom substrate of the undeformed and fully deformed aggregate, respectively. Interestingly, the deformation that results in strain hardening also produces nearly close-packed structure of the thinned aggregate.

Fig 5.1b plots a similar response in a device with a stiffer (E = 400 kPa) flexible PDMS membrane. As reported in Fig 5.1a, the deformation of the PDMS membrane in contact with the aggregate is indistinguishable from the unloaded device. Again at $\varepsilon \sim 0.8$, the slope increases dramatically. This increase is so extreme that at the conclusion of the experiment an additional incremental increase in pressure no longer further deforms the aggregate. For this to occur the elastic modulus must be greater than 400 kPa, the elastic modulus of PDMS. Fig. 5.1 e and f show the undeformed and fully deformed aggregates respectively. The final configuration of the aggregate in this experiment appears to be two rows of individual bacteria in a nearly close packed configuration.

5.3.2 Strain hardening in biofilms

Fig 5.2 plots the stress-strain relationship of four biofilms tested in the flexible microfluidic device described in chapter 3. To contrast between the biofilms and the weakly elastic aggregates, data from a typical control experiment are shown. (A control experiment consists of water in the test chamber, rather than elastic biofilm.) In the cose of biofilms, the difference between the loaded and the unloaded behavior of the flexible PDMS membrane is resolvable. This resolvable difference provides a basis to determine

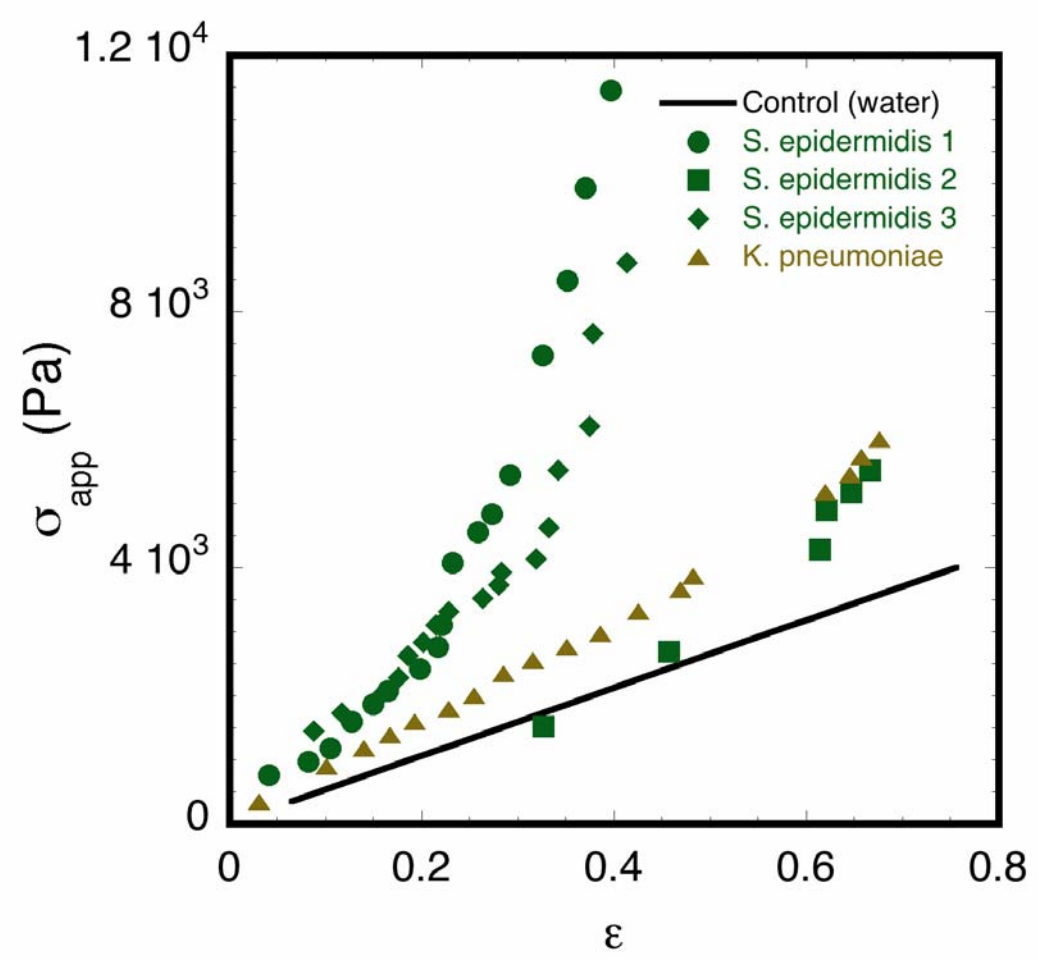

Figure 5.2: Stress-strain behavior of four biofilms in a flexible microfluidic rheometer. These data provide the basis for analyzing the complex strain based behavior of the elastic modulus of biofilms.

the elastic modulus of the biofilms. For all four biofilms an increase in applied pressure results in a non-linear increase in strain. In chapter 3 this behavior was analyzed as a 2-regime phenomenon. That is FEA was applied to characterize a low-strain and high-strain modulus of the biofilms. Yet, this analysis procedure is incomplete since the division into low and high strain regimes were arbitrary. In order to better analyze this complex behavior here we characterize the data so as to extract a strain-dependent elastic modulus of the bacterial biofilms.

To this end we again use FEA to characterize the strain-based static elastic modulus of the biofilms. Our methodology is to use the average slope of four consecutive points along each curve. This moving average was chosen so as to balance out interest to extract a strain dependent modulus and the need to address the noise inherent in a point by point analysis. The slope extracted from the moving average was compared to FEA solutions (conducted as per the methods of chapter 3) of varying modulus to characterize the elastic modulus at the local strain of the four point average.

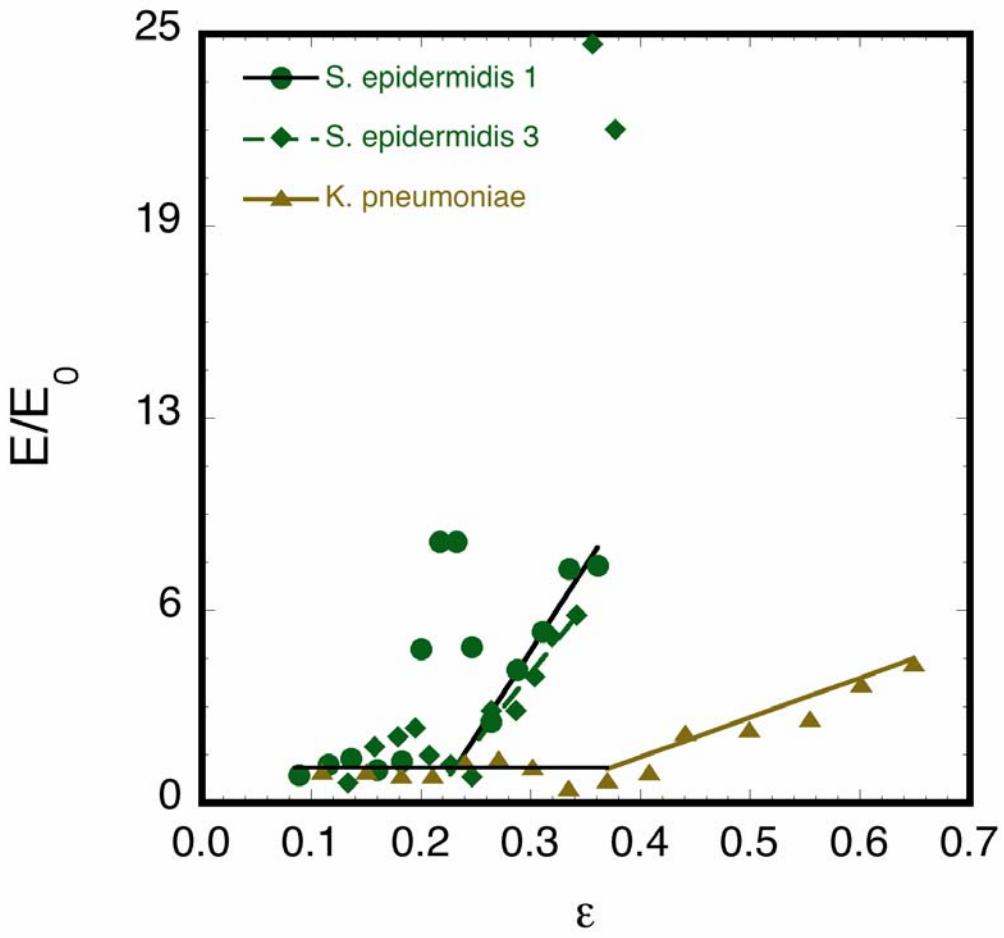

Figure 5.3 plots the localized strain-based elastic modulus normalized by the low strain modulus reported in chapter 3.

Fig. 5.3 plots the resultant strain-based elastic modulus for three of the films for which sufficient data to support the four point moving data was available. (S. epidermidis 2 was omitted due to the number of points.) The ordinate of the figure is normalized by the low-strain modulus of the biofilms (the values of which have already been reported in chapter 3). After the initial linear regime, the non-linear elastic modulus increases linearly with different slopes for the three different biofilms. As indicated by the linear fits, the slopes given for the fit of the *S. epidermidis* films are ~ 55 and 45 for *S. epidermidis* 1 and *S. epidermidis* 2, respectively. The slope of the non-linear fit for *K. pneumoniae* is ~13.

Gisler et al. report strain hardening scaling as γ^2 for colloidal fractal gels [6]. While our data due not support an power law fit of order 2, the analysis is similar. Due to the resolution limits of the flexible microfluidic rheometer we are unable to collect data at very low strain. More measurements in the low-strain (linear) regime may provide better insight into the transition to the non-linear regime. Interestingly, a similar response reported in a microindentation characterization of biofilms also shows a linear increase in elastic modulus with strain. These data are reported as anomalies of the experimental technique [14].

5.3.3 Origins of strain hardening in biofilms

In chapter 4, we applied image processing techniques to characterize the microstructure of biofilms. Here we apply the same type of analysis to determine a source of strain hardening. First we characterize the structure of the biofilm by determining the volume fraction, ϕ, of bacteria in the biofilm prior to compression. We then correlate the uncompressed total volume fraction with the initial area fraction of

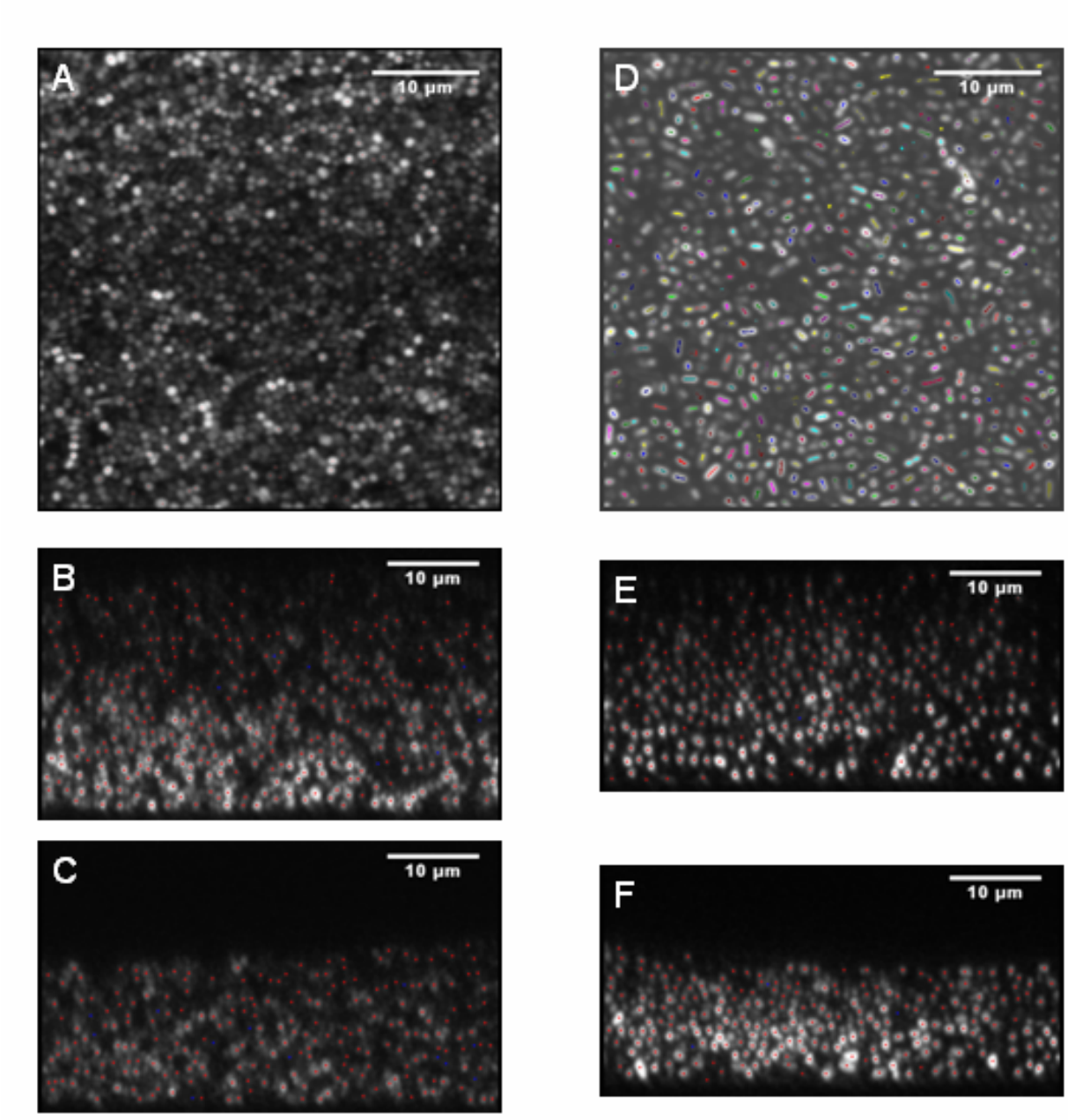

Figure 5.4 A and D show a reconstructed 2-D slice of the three dimensional volume acquired to determine the volume fraction of the uncompressed biofilm. The subsequent images show the plane perpendicular to the bottom substrate of the device B, E before pressure is applied and C, F at full compression.

biofilm in the plane perpendicular to the bottom substrate for the deformation measurements. Using this correlation we can estimate the volume fraction of bacteria at

each step in compression to determine if strain hardening is due to densification of bacteria in the biofilm.

Fig 5.4 shows reconstructed images of two different biofilms. Fig 5.4A is a 2D reconstructed scan with individual *S. epidermidis* bacterium identified. Fig 5.4B has backbones identified in a 2D scan of *K. pneumoniae*. Identification of the bacteria in the initial 3D volumes of these biofilms results in a characterization of the structure of the biofilms. Figs 5.4 B and C show bacteria identification in the 2D deformation frame before and after compression respectively for the *S. epidermidis* biofilm. Likewise the same image processing can be used to identify *K. pneumoniae* despite their anisotropy (Fig E and F). This data can then be used to calculate the effect of strain on the densification of bacteria within the biofilm.

Fig 5.5 plots the strain dependent volume fraction of bacteria in the biofilms as it is compressed (data for *S. epidermidis* 3 not shown). This data is calculated using the area fraction of bacteria during compression with correlation to the initial volume fraction determined by 3D image processing. To compare common volumes the height of the area analyzed was determined by the final height of the compressed film. Interestingly the volume fractions remain relatively flat during the compression of the biofilm, especially for the stiffest sample, *S. epidermidis* 1. The slightly softer *S. epidermidis* 2 biofilm (E_0 = 2.7 kPa vs. E_0 = 3.2 kPa for *S. epidermidis* 1) has a lower volume fraction but also remains steady. The low volume fraction *K. pneumoniae* is also relatively flat with a step-wise increase at $\varepsilon \sim 0.35$ to remain steady for the remainder of the compression. Interestingly, the strain hardening behavior of colloidal fractal gels was

also independent of volume fraction allowing for a master curve of elastic modulus and strain to be generated for gels of different colloidal volume fractions [6].

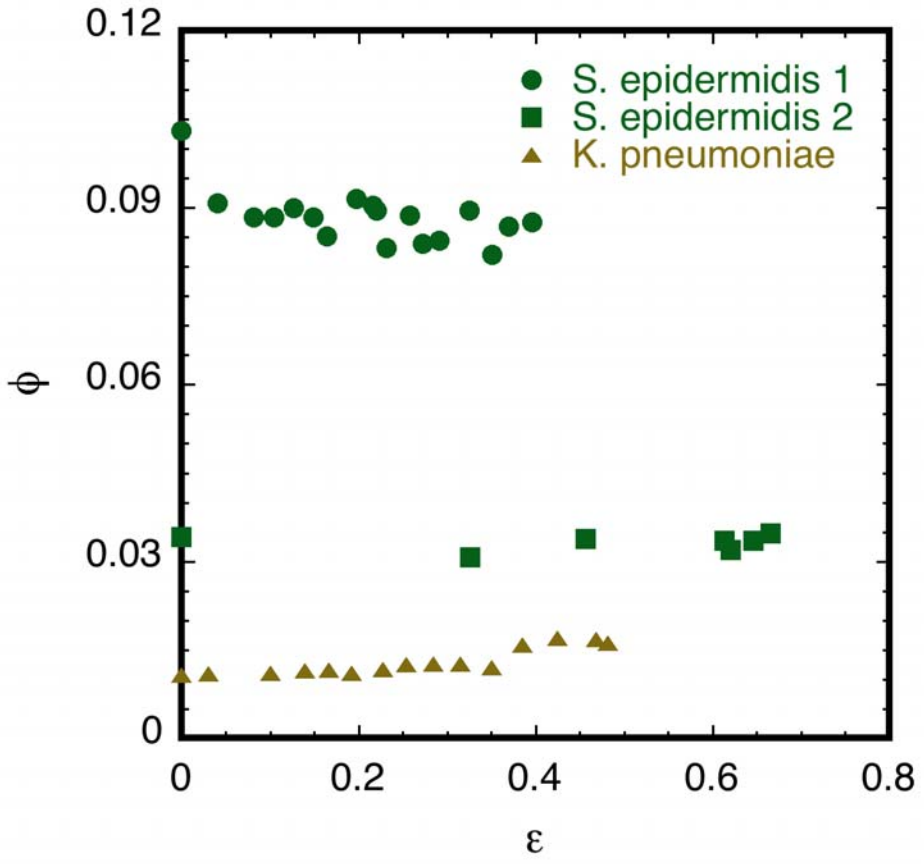

Figure 5.5 plots the volume fraction of three biofilms under compression in the flexible microfluidic rheometer.

In Fig. 5.6 we use image processing to plot the trajectories of individual bacteria in a *S. epidermidis* film as it is compressed to understand the microscale structural changes in the biofilm. Fig. 5.6a shows a projection of the strain series with bacteria centroids identified in each frame. Trajectories of this motion were also plotted in the associated vector plot (Fig. 5.6b). This analysis provides insight into the bacteria's motion within the biofilm leading to the final deformation upon compression. Here we report the lateral motion of the bacteria within the film orthogonal to the axis of compression. This analysis is consistent with the result of steady volume fraction

reported in Fig. 5.5. As bacteria enter the analysis window due to compression other bacteria leave the window in a trajectory parallel to the bottom substrate.

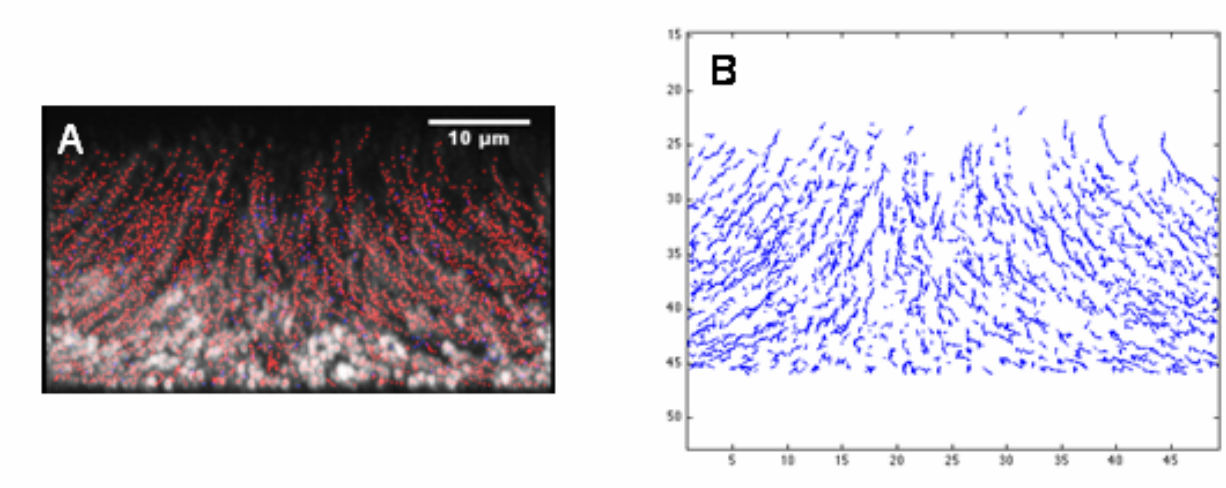

Figure 5.6: We plot the dynamic response to the applied pressure of individual bacteria in a *S. epidermidis* biofilm. Fig 5.6A gives the overlay of the strain series with particle centroids identified. This data can be converted to trajectories using image processing software (Fig 5.6B).

5.4 Conclusions

In this chapter we report strain hardening in both bacterial aggregates and biofilms. From experimental data with the flexible microfluidic rheometer, we found that the normalized elastic modulus increases linearly with strain (in the non-linear regime). While the magnitude of the elastic modulus may be dependent upon the density, the strain hardening reported here is not a function of volume fraction. This result is consistent with the analysis from linking the trajectories of individual bacteria within the biofilm during the compression experiment.

References

1. Rupp, C.J., C.A. Fux, and P. Stoodley, *Viscoelasticity of Staphylococcus aureus biofilms in response to fluid shear allows resistance to detachment and facilitates rolling migration.* Applied and Environmental Microbiology, 2005. **71**(4): p. 2175-2178.
2. Shaw, T., et al., *Commonality of elastic relaxation times in biofilms.* Physical Review Letters, 2004. **93**(9).
3. Enderle, J.D., Susan M. Blanchard and Joseph D. Bronzino, *Introduction to Biomedical Engineering*. 2000, San Diego: Academic Press. 1062.
4. Mewis, J. and G. Biebaut, *Shear thickening in steady and superposition flows effect of particle interaction forces.* Journal of Rheology, 2001. **45**(3): p. 799-813.
5. Pouzot, M., et al., *Strain hardening and fracture of heat-set fractal globular protein gels.* Journal of Colloid and Interface Science, 2006. **293**(2): p. 376-383.
6. Gisler, T., R. Ball, and D.A. Weitz, *Strain hardening of fractal colloidal gels.* Physical Review Letters, 1999. **82**(5): p. 1064-1067.
7. Hoy, R.S. and M.O. Robbins, *Strain hardening of polymer glasses: Entanglements, energetics, and plasticity.* Physical Review E, 2008. **77**(3).
8. Duffy, D.C., et al., *Rapid prototyping of microfluidic systems in poly(dimethylsiloxane).* Analytical Chemistry, 1998. **70**(23): p. 4974-4984.
9. Unger, M.A., et al., *Monolithic microfabricated valves and pumps by multilayer soft lithography.* Science, 2000. **288**(5463): p. 113-116.
10. Balestrino, D., et al., *The characterization of functions involved in the establishment and maturation of Klebsiella pneumoniae in vitro biofilm reveals dual roles for surface exopolysaccharides.* Environmental Microbiology, 2008. **10**(3): p. 685-701.
11. O'Gara, J.P. and H. Humphreys, *Staphylococcus epidermidis biofilms: importance and implications.* Journal of Medical Microbiology, 2001. **50**(7): p. 582-587.
12. Crocker, J.C. and D.G. Grier, *Methods of digital video microscopy for colloidal studies.* Journal of Colloid and Interface Science, 1996. **179**(1): p. 298-310.
13. Dibble, C.J., M. Kogan, and M.J. Solomon, *Structure and dynamics of colloidal depletion gels: coincidence of transitions and heterogeneity.* Phys Rev E Stat Nonlin Soft Matter Phys, 2006. **74**(4 Pt 1): p. 041403.
14. Cense, A.W., et al., *Mechanical properties and failure of Streptococcus mutans biofilms, studied using a microindentation device.* Journal of Microbiological Methods, 2006. **67**(3): p. 463-472.

Chapter 6

Conclusions

6.1 Conclusions

In this thesis we successfully applied confocal microscopy to characterize the local structure and material properties of complex fluids found in industry and biology. To study both ink emulsions and bacterial biofilms, high resolution confocal images were used to measure the evolution of the microstructure in response to applied stresses. For ink-fountain solution emulsion studies confocal microscopy allowed us to quantify droplet evolution in response to shear flow on two different substrates. Confocal imaging was also used to directly measure the deformation of a flexible microfluidic rheometer. The ability to image in the plane perpendicular to the bottom substrate enabled the characterization of soft viscoelastic solids. Quiescent studies were also conducted on rod-shaped bacterial aggregates to quantify structural parameters related to their aggregation in two different growth regimes. Once the methods to characterize microstructure of quiescent biofilms were developed, we used these techniques to better understand the source of interesting rheological responses in biofilms.

In chapter 2 we use confocal microscopy to characterize ink-fountain solution emulsion structure evolution on two different substrates. We found the interaction effects between fountain solution additives and substrate to be quite complex. Namely, the surface coverage of an aqueous fountain solution on a hydrophobic substrate was higher

than on a hydrophilic surface. Surfactant additive in the aqueous fountain solution suppressed bulk-surface coalescence events on hydrophobic substrates. Interestingly, the same additives allow for increased aqueous droplet density on the hydrophobic substrate. These results are of interest to lithographic printers because they provide visual evidence of microstructural events that could lead to defects on the press. This type of evidence would not be available without the use of a shear cell mounted to a confocal microscope.

While in chapter 2 we used a shear cell to apply flow to a complex fluid, in chapter 3 we developed a microfluidic rheometer to accomplish the same goal. We used confocal microscopy to measure the response of soft viscoelastic solids to compressive stress. This microfluidic rheometer was capable of characterizing viscoelastic material properties of samples as small as ~200 pL. We used confocal microscopy and the rheometer to determine the elastic modulus of monospecies biofilms of *S. epidermidis* and *K. pneumoniae*. Interestingly, compression of these biofilms led to the discovery of a strain hardening regime. This non-linear response of the biofilms can be clinically significant to clearance and fracture events.

In chapter 4 we developed techniques to characterize the microstructure of quiescent bacterial aggregates and biofilms. Using high resolution confocal microscopy with image processing we were able to identify the three dimensional location and orientation of rod-shaped bacteria within the aggregates and biofilms. This data was used to calculate the nearest neighbor distance of bacteria within each structure. Interestingly two different genotypes of *K. pneumoniae* displayed no distinguishable difference in structure. This is of interest because it is known that capsule degeneracy can lead to production of different proteins in the polysaccharide matrix around the cell [1]. We

used the same structural measure to show that rod-shaped bacteria in biofilms pack much more closely than their planktonically grown aggregates. This image processing at the level of the bacteria is important to quantify structural morphology of the each organism within the aggregates. Without image processing the tendency has been to use confocal microscopy to characterize bulk properties of biofilms and qualify structural heterogeneities.

Finally, in chapter 5, we use the methods described in the previous chapters to investigate the interesting rheological response of compressed biofilms. We were able to determine a trend in increasing elastic modulus with strain. We were also able to determine that this increase was independent of volume fraction of the bacteria within the films. This result was consistent with the trajectories of each bacterium showing the migration of the bacteria out of the field of view during compression.

In this thesis we have shown the ability to couple microscale characterization of complex fluids with rheological measurements. With confocal microscopy we quantified interesting structural changes and mechanical properties of ink-fountain solution emulsions and biofilms. Microscale measures are critical to understand bulk phenomena that can occur in these materials. A better understanding of this behavior can lead to enhanced formulation of industrial products. It can also lead to a better understanding of clinical issues associated with bacterial biofilms. The methods shown here allow research tools used for fundamental model materials to be applied directly to industrial and biological systems.

6.2 Future work

Just as the work in this thesis was an extension of techniques used to study model materials, the work here is just a first step in using confocal microscopy to characterize these types of materials. A strategy for the extension of these techniques would be to include features that are applicable to the problem being modeled.

For example, the ink-fountain solution study was conducted on homogeneous substrates. A simple extension of this experiment would be to include patterned substrates with hydrophilic and hydrophobic areas at length scales appropriate for printing. Interestingly, these patterned substrates have already been created on the microscale using chemical vapor deposition [2]. These patterned substrates would be more typical of the plates used in lithographic printing. The application of confocal microscopy to detect the emulsion structure that forms on the heterogeneous substrate would still be appropriate.

Often biological systems are not as ideal as those studied here. Mixed species biofilms can exist complicating the problem of characterizing their microstructure [3]. The process used to identify rod-shaped bacteria would likely work for mixed species biofilms as well. Parameters may need to be adjusted, however the underlying physics associated with proper identification is still the same. A technique to aid in this type of study would be to include different fluorescent signatures per species. This method could be used to identify growth patterns of mixed species biofilms. Using the image processing algorithm reported here, the structure of the biofilm may be obtained. This data would include the location of spherical and rod-shaped bacteria within the same biofilm or aggregate.

As reviewed in chapter 3, a natural extension of the microfluidic rheometer is to apply sinusoidal variation in the applied pressure on the membrane. The data analysis would then be similar to current methods used in mechanical rheometry [4]. High acquisition times on certain confocal microscopes would limit the application. However faster confocal microscopes exist to address this need [5].

Finally, confocal microscopy need not be applied only to the materials and processes discussed here. Confocal particle tracking could provide insight into such biological processes as phagocytosis. In this process shape and orientation angle determine the success of eliminating the target [6]. Confocal microscopy and image processing can be used to measure the rotational rates of the anisometric particle during phagocytosis. Also confocal microscopy can be used for *in vivo* measurements. It would be fascinating to see a bacterial aggregate flowing through the vascular system to measure the compression from decreasing diameter of capillaries. This could be accomplished by thinning tissue around a capillary to reduce turbidity. This type of measurement would provide powerful insight into the role of strain hardening as biofilms flow in physiological environments.

3D confocal imaging has been used extensively for qualitative measurements. Here we show that quantification through image processing can be extended to industrial and biological systems. This thesis presents feasible approaches to incorporate this type of analysis to different systems. Techniques to extend these methods further could provide valuable insight into rheological phenomena associated with consumer products, pharmaceuticals and biological complex fluids.

References

1. Favre-Bonte, S., B. Joly, and C. Forestier, *Consequences of reduction of Klebsiella pneumoniae capsule expression on interactions of this bacterium with epithelial cells.* Infection and Immunity, 1999. **67**(2): p. 554-561.
2. Chen, H.Y. and J. Lahann, *Vapor-assisted micropatterning in replica structures: A solventless approach towards topologically and chemically designable surfaces.* Advanced Materials, 2007. **19**(22): p. 3801-+.
3. Shaw, T., et al., *Commonality of elastic relaxation times in biofilms.* Physical Review Letters, 2004. **93**(9).
4. Ferry, J.D., *Viscoelastic Properties of Polymers.* 3rd Edition ed. 1980, New York: John Wiley and Sons.
5. Wang, E., C.M. Babbey, and K.W. Dunn, *Performance comparison between the high-speed Yokogawa spinning disc confocal system and single-point scanning confocal systems.* Journal of Microscopy-Oxford, 2005. **218**: p. 148-159.
6. Champion, J.A. and S. Mitragotri, *Role of target geometry in phagocytosis.* Proceedings of the National Academy of Sciences of the United States of America, 2006. **103**(13): p. 4930-4934.